

Turbulent Mixing of Passive Scalars at High Schmidt Number

A Thesis
Presented to
The Academic Faculty

by

Shuyi Xu

In Partial Fulfillment
of the Requirements for the Degree
Doctor of Philosophy

School of Aerospace Engineering
Georgia Institute of Technology
January 2005

Turbulent Mixing of Passive Scalars at High Schmidt Number

Approved by:

Professor P.K. Yeung, Advisor
School of Aerospace Engineering
Georgia Institute of Technology

Professor Lakshmi Sankar
School of Aerospace Engineering
Georgia Institute of Technology

Professor Suresh Menon
School of Aerospace Engineering
Georgia Institute of Technology

Professor Marilyn Smith
School of Aerospace Engineering
Georgia Institute of Technology

Professor Don Webster
School of Civil Engineering
Georgia Institute of Technology

Date Approved: January 2005

To my beloved parents

who brought me into this world against all odds

ACKNOWLEDGEMENTS

This work was supported by the National Science Foundation (grant number CTS-0121030). Our computing resources are provided by the National Partnership for Advanced Computational Infrastructure at the San Diego Supercomputer Center.

I would like to express my gratitude to those who directly or indirectly made this work possible. First of all, I would like to thank Dr. P.K. Yeung, my thesis advisor, for guiding me through the process of doctoral research. During the past few years of working with Dr. Yeung, I learned the importance of hard working and taking initiatives in research. I learned from him that it takes much more than just being smart to succeed in the frontiers of scientific research. I am also grateful to him for providing me the opportunity to explore subjects of interest, which broadened my intellectual scope. I am grateful to have the opportunities to meet well-known authors in the field of turbulence such as Drs. K.R. Sreenivasan, B.L. Sawford, S.B. Pope and Z. Warhaft. I would also like to thank Dr. Jagoda and other professors with whom I have taken courses for their valuable instruction and support.

I would like to thank Dr. Suresh Menon, Dr. Don Webster, Dr. Lakshmi Sankar and Dr. Marilyn Smith for taking the time to be on my thesis committee and their valuable suggestions on the dissertation. I am also thankful to my previous and current lab mates Dr. Prakash Vedula, Diego Donzis, Elizabeth Kurth, to name just a few, for their help and support.

My parents, my family and my close relatives deserve my deepest indebtedness and gratitude for their constant love, support, encouragement and their confidence in me. Finally, I am grateful to all my friends who have shared their lives with me at some points of my life, without whose friendships, part of my life would have been meaningless.

TABLE OF CONTENTS

DEDICATION	iii
ACKNOWLEDGEMENTS	iv
LIST OF TABLES	vii
LIST OF FIGURES	viii
SUMMARY	xiii
I INTRODUCTION	1
1.1 Background	1
1.2 Literature Review	5
1.3 Outline	10
II NUMERICAL METHOD OVERVIEW	11
2.1 Direct Numerical Simulation	11
2.2 Data Analysis and Simulation Parameters	16
III SCALING PROPERTIES AND SMALL-SCALE CHARACTERISTICS 24	
3.1 Scalar spectrum and structure functions	24
3.2 Local Isotropy: Schmidt number effects	33
3.3 Intermittency: effects for high Schmidt numbers	37
IV INTERMITTENCY EXPONENTS OF ENERGY AND SCALAR DIS- SIPATION	78
4.1 Background	78
4.2 Velocity field intermittency	81
4.3 Intermittency of scalars	85
V DIFFERENTIAL DIFFUSION AND SCALAR SPECTRAL TRANS- FER	108
5.1 Differential diffusion	108
5.2 Scalar spectral transfer	112
5.3 Scalar subgrid transfer	114

VI CONCLUSION	134
6.1 Principal results	134
6.2 Future research	136
Appendix A	138
Appendix B	139
Appendix C	140
Appendix D	141
REFERENCES	143
VITA	150

LIST OF TABLES

2.1	Simulation parameters at $R_\lambda \approx 38$	21
2.2	Simulation parameters at $R_\lambda \approx 8$	21
2.3	Simulation parameters at higher Reynolds numbers	22
3.1	Mixed gradient skewness and flatness at R_λ up to 390.	40
3.2	Mixed gradient skewness and flatness at $R_\lambda \approx 8$	41
3.3	Statistical moments of scalar gradients and the scalar dissipation at $R_\lambda \approx 38$	42
3.4	Statistical moments of scalar gradients and the scalar dissipation at R_λ up to 390.	43
3.5	Statistical moments of scalar gradients and the scalar dissipation at $R_\lambda \approx 8$	44
4.1	Intermittency exponents for energy dissipation and enstrophy	92
4.2	Intermittency exponents for scalar dissipation at higher Reynolds numbers	93
4.3	Intermittency exponents for scalar dissipation at $R_\lambda \approx 38$	93
4.4	Intermittency exponents for scalar dissipation at $R_\lambda \approx 8$	94

LIST OF FIGURES

2.1	Comparison of Kolmogorov-scaled energy spectrum at $R_\lambda \approx 38$ (Δ) and $R_\lambda \approx 8$ (\circ).	24
3.1	Compensated spectrum according to Obukhov-Corrsin variables (Eq. 3.1) for passive scalars at different Schmidt numbers (open symbols for 1/8, closed symbols for 1.0). Triangles, circles and squares denote Reynolds number at 90, 140 and 240 respectively. Cross and plus denote $Sc = 1$ and 1/8, respectively, at $R_\lambda \approx 390$. Dashed line at 0.67 is for comparison with experiments.	45
3.2	Compensated one-dimensional spectrum for scalars of $Sc = 1/8$ (triangles) and $Sc = 1$ (circles) at $R_\lambda \approx 390$. Dashed line at 0.4 is for comparison with experiments (Sreenivasan 1996). Also shown for comparison are: Squares for one-dimensional longitudinal energy spectrum in DNS, and unmarked solid line for data on scalar spectrum from Mydlarski & Warhaft (1998) at $R_\lambda \approx 582$ and Prandtl number of 0.71.	46
3.3	Obukhov-Corrsin scaling of component-averaged second-order structure function of passive scalars at different Schmidt numbers (open symbols for 1/8, closed symbols for 1.0). Triangles, circles and squares denote Reynolds number at 90, 140 and 240 respectively. Cross and plus denote $Sc = 1$ and 1/8, respectively, at $R_\lambda \approx 390$. The dotted line shows the small r asymptote (Eq. 3.4). Dashed line at 1.608 is for comparison with experiments. The inset shows second-order structure function normalized by the scalar variance (which is not dependent on r), with dashed line at the value 2.0.	47
3.4	Scaling of mixed third-order velocity-scalar structure function, compared with Yaglom's relation (Eq. 3.7). Symbols are same as in Fig. 3.3. Dashed line at 2/3 is for comparison with Yaglom's exact result.	48
3.5	Normalized third-order velocity-scalar structure function for $Sc = 1$ at $R_\lambda \approx 390$, with separation distance r taken in different coordinate directions (triangles, circles and squares for x, y, z , respectively).	49
3.6	Even-order compensated scalar structure functions. Curves A and B are at $R_\lambda \approx 240$ for $Sc = 1/8$ and $Sc = 1$, respectively. Curves C and D are at $R_\lambda \approx 390$ for $Sc = 1/8$ and $Sc = 1$, respectively. Compensation power law exponents for $Sc = 1$ at $R_\lambda \approx 390$ are $\zeta_2^\phi = 0.6$, $\zeta_4^\phi = 0.85$, $\zeta_6^\phi = 1.0$ and $\zeta_8^\phi = 1.1$	50
3.7	Odd-order compensated scalar structure functions, where curve notations are the same as FIG. 3.6. $\zeta_3^\phi = 0.75$, $\zeta_5^\phi = 0.95$, and $\zeta_7^\phi = 1.05$ for $Sc = 1$ at $R_\lambda \approx 390$	51
3.8	Even-order compensated longitudinal velocity structure functions. Curves A, B and C are at $R_\lambda \approx 140, R_\lambda \approx 240$ and $R_\lambda \approx 390$, respectively. Compensation power law exponents at $R_\lambda \approx 390$ are $\zeta_2 = 0.68$, $\zeta_4 = 1.26$, $\zeta_6 = 1.75$ and $\zeta_8 = 2.15$	52
3.9	Same as FIG. 3.8 for odd-order structure functions. $\zeta_3 = 1$, $\zeta_5 = 1.5$, and $\zeta_7 = 1.96$ at $R_\lambda \approx 390$	53

3.10	Scaling exponents for scalar structure functions and longitudinal velocity structure functions. Triangles and squares are DNS results at $R_\lambda \approx 390$, for scalar structure functions and longitudinal velocity structure functions, respectively. Circles are for scalar structure functions at $R_\lambda \approx 461$ and $Pr \approx 0.71$ from Mydlarski and Warhaft (1998) for temperature field in grid turbulence. Crosses are for longitudinal velocity structure functions at $R_\lambda \approx 536$ from Anselmet <i>etal.</i> (1984) for a turbulent jet. Dashed line with a slope of $1/3$ is shown to represent KOC prediction. Solid circles are from p.166(c) of Dasi (2004) for $Sc \approx 1000$ at $Re10000$, $x = 2m$ for turbulent boundary layers.	54
3.11	Three-dimensional spectra at (a) $R_\lambda \approx 38$ for scalars of Schmidt numbers $1/4, 1, 4, 8, 16, 32, 64$ (lines A to G respectively). (b) at $R_\lambda \approx 8$ for scalars of Schmidt numbers $64, 128, 256$ (256^3) and $256, 512, 1024$ (512^3) (lines A to F respectively). The dashed line has a slope of -1 on logarithmic scales. . .	55
3.12	Three-dimensional spectra normalized by Kolmogorov scaling. (a) same data as FIG. 3.11(a). The dashed line has a slope of $2/3$. (b) Same as FIG. 3.12(a), except at $R_\lambda \approx 8$ for $Sc = 64, 128, 256$ (256^3) and $Sc = 256, 512, 1024$ (512^3) (line A to F, respectively).	57
3.13	Three-dimensional scalar spectrum normalized by Batchelor variables at (a) $R_\lambda \approx 38$ for $Sc = 1, 4, 8, 16, 32, 64$ (lines A-F, respectively). Dotted curve for Batchelor's expression (Eq. 3.13). (b) at $R_\lambda \approx 8$ for $Sc = 64, 128, 256$ (256^3) and $256, 512, 1024$ (512^3) (lines A-F, respectively). Dashed curve for Kraichnan's (Eq. 3.14). Inset shows the same data in log-linear scales. . .	59
3.14	Same as FIG. 3.13(a), except for $R_\lambda \approx 38$ and $Sc = 64$ (triangle), $R_\lambda \approx 8$ and $Sc = 64$ (square) and $R_\lambda \approx 8$ and $Sc = 1024$ (circle).	61
3.15	Scaling of second-order scalar structure function (similar to FIG. 3.3) for scalars of (a) $Sc = 1, 4, 8, 16, 32, 64$ (lines A-F, respectively) at $R_\lambda \approx 38$. (b) for $Sc = 64, 128, 256$ (256^3) and $Sc = 256, 512, 1024$ (512^3) at $R_\lambda \approx 8$ (lines A-F, respectively).	62
3.16	Scaling of mixed third-order velocity-scalar structure function (similar to FIG. 3.4) for scalars with (a) $Sc = 1, 4, 8, 16, 32, 64$ (lines A-F, respectively) at $R_\lambda \approx 38$. (b) for $Sc = 64, 128, 256$ (256^3) and $Sc = 256, 512, 1024$ (512^3) at $R_\lambda \approx 8$ (lines A-F, respectively).	64
3.17	(a) Skewness of scalar gradients in the direction parallel to the mean scalar gradient. Close symbols are for $R_\lambda \approx 38$, and open symbols for $R_\lambda \approx 8$. Solid and open squares from Mydlarski & Warhaft (1998) at $R_\lambda \approx 217, 731$ for $Pr=0.71$, Solid circle from Tong & Warhaft (1994) at $30 < R_\lambda < 130$. (b) Kurtosis of scalar gradients. Triangles are for $\Delta_{\parallel}\phi$ and squares are for $\Delta_{\perp}\phi$. Close symbols are for $R_\lambda \approx 38$, and open symbols for $R_\lambda \approx 8$. (c) Normalized odd-order moments of scalar gradients. Triangles are for μ_3 , squares are for μ_5 and circles are for μ_7 . Close symbols are for $R_\lambda \approx 38$, and open symbols for $R_\lambda \approx 8$	66
3.18	Standardized probability density function (shown as base-10 logarithm) of $\nabla_{\parallel}\phi$ for scalars of Schmidt numbers (a) $1, 4, 8, 16, 32, 64$ (lines A to F respectively) at $R_\lambda \approx 38$. (b) $1, 8, 64$ (lines A-C, 128^3), $64, 128, 256$ (lines D-F, 256^3) and $256, 512, 1024$ (lines G-I, 512^3) at $R_\lambda \approx 8$. Dashed curve shows a Gaussian distribution for comparison.	69

3.19	The skewness structure function of $\nabla_{\parallel}\phi$ (Eq. 3.17) as a function of separation on Batchelor scales, for scalars of Schmidt numbers (a) 1/4, 1/2, 1, 4, 8, 16, 32, 64 (lines A to H respectively) at R_{λ} 38. Dashed line shows Gaussian value of 0. (b) 1, 8, 64 (lines A-C, 128^3), 64, 128, 256 (lines D-F, 256^3) and 256, 512, 1024 (lines G-I, 512^3) at $R_{\lambda} \approx 8$	71
3.20	The flatness structure function of (a) $\nabla_{\parallel}\phi$ with symbols same as FIG. 3.19(a). (b) $\nabla_{\perp}\phi$. Dashed line shows Gaussian value of 3.	73
3.21	The flatness structure function of (a) $\nabla_{\parallel}\phi$ with symbols same as FIG. 3.19(b). (b) $\nabla_{\perp}\phi$ with symbols same as FIG. 3.19(b).	75
3.22	Plot of flatness versus skewness for the scalar dissipation. Each data point represents one realization taken from our data sets at various Reynolds numbers of $R_{\lambda} \approx 8$, $R_{\lambda} \approx 38$, $R_{\lambda} \approx 140$, $R_{\lambda} \approx 240$ and $R_{\lambda} \approx 390$. The dashed line is a least-square fit, with a slope of 2.33.	77
4.1	The functions (a) $\text{Var}(\ln \epsilon_r)$, (b) $\langle \epsilon_r^2 \rangle / \langle \epsilon \rangle^2$, and (c) $\langle \epsilon(x)\epsilon(x+r) \rangle / \langle \epsilon \rangle^2$ used to infer intermittency exponents for the energy dissipation. Lines A-E represent results at Taylor-scale Reynolds numbers $R_{\lambda} \approx 8$ (on 256^3 grid), 38 (256^3), 140 (256^3), 240 (512^3), and 390 (1024^3), respectively. Inset in (c) shows use of slope of line E to evaluate the exponent μ_3 at $R_{\lambda} \approx 390$. Dashed lines are at 0.17 and 0.21, respectively.	95
4.2	Comparison of the mean-squared local energy dissipation $\langle \epsilon_r^2 \rangle / \langle \epsilon \rangle^2$, at (a) R_{λ} 140, (b) R_{λ} 390, for averages taken in one, two- and three-dimensions respectively (lines A-C).	96
4.3	Comparisons of two-point correlators of energy dissipation and its one-dimensional surrogates at (a) R_{λ} 140, (b) R_{λ} 390. Triangles for full 3-D dissipation ($Y = \epsilon$) averaged over distance r in three directions; circles for longitudinal velocity with longitudinal separation distance (e.g. $Y = (\partial u_1 / \partial x_1)^2$ with $\underline{r} = r\mathbf{e}_1$), squares for transverse velocity with transverse separation distance (e.g. $Y = (\partial u_1 / \partial x_2)^2$ with $\underline{r} = r\mathbf{e}_3$).	97
4.4	Comparisons of two-point correlators of different velocity gradients squared $(\partial u_{\alpha} / \partial x_{\beta})^2$, with distance r taken along the axis x_{γ} . Open triangle: $\alpha = \beta = \gamma$, open circle: $\alpha = \beta \neq \gamma$, open square: $\alpha = \gamma \neq \beta$, close triangle: $\alpha \neq \beta = \gamma$, close circle: $\alpha \neq \beta \neq \gamma$	98
4.5	Normalized sixth-order longitudinal velocity structure function. $R_{\lambda} \approx 140$, 240 and 390 (lines A-C respectively). The inset shows the slopes of the curves, with a dashed line corresponding to an intermittency exponent 0.25 for reference.	99
4.6	Sams as Fig. 4.1, but for the enstrophy ($\Omega = \omega_i \omega_i$).	100
4.7	Comparisons of two-point correlators of scalar dissipation and its scalar gradient surrogates for (a) $R_{\lambda} \approx 390$, $Sc = 1$ and (b) $R_{\lambda} \approx 38$, $Sc = 64$. Triangles for full scalar dissipation (χ) averaged over distance r in three directions; circles and squares for components parallel (χ_{\parallel}) and perpendicular (χ_{\perp}) to direction of mean gradient respectively.	101
4.8	Same as Fig. 4.7, but for local averages taken over three-dimensional boxes of length r on each side.	102

4.9	Same as Fig. 4.1, but for scalar dissipation at $Sc = 1$ for the same Reynolds numbers.	103
4.10	Comparison of two-point correlators for scalar dissipation at $Sc = 1/8$ and 1 (lines A and B) R_λ 390, with distance r normalized by (a) Kolmogorov scale and (b) Obukhov-Corrsin scale	104
4.11	Same as Fig. 4.1, but for scalar dissipation at R_λ 38, for Schmidt numbers $Sc = 1, 4, 8$ (lines A-C, 256^3) and $16, 32, 64$ (lines D-F, 512^3).	105
4.12	Same as Fig. 4.11(a,b,c), but at R_λ 8, for $Sc = 1, 4, 16$ (lines A-C, 128^3), 64 (line D, 256^3), and $256, 1024$ (lines E-F, 512^3).	106
4.13	Intermittency exponents as a function of Sc : closed symbols at $R_\lambda \approx 38$, open symbols at $R_\lambda \approx 8$; triangles (μ_3), squares (μ_2), circles (μ_1).	107
5.1	Evolution of the scalar correlation coefficient $\rho_{\alpha\beta}$. Line A, B, and C represent scalar pairs with (a). $Sc = \{16, 32\}$, $Sc = \{16, 64\}$ and $Sc = \{32, 64\}$ at $R_\lambda \approx 38$. (b). $Sc = \{1, 8\}$, $Sc = \{1, 64\}$ and $Sc = \{8, 64\}$ at $R_\lambda \approx 8$. (c). $Sc = \{256, 512\}$, $Sc = \{256, 1024\}$ and $Sc = \{512, 1024\}$ at $R_\lambda \approx 8$	119
5.2	Evolution of the scalar gradient ($\nabla_{\parallel}\phi$) correlation coefficient $g_{\alpha\beta}$. Line A, B, and C represent scalar pairs with (a) $Sc = \{16, 32\}$, $Sc = \{16, 64\}$ and $Sc = \{32, 64\}$ at $R_\lambda \approx 38$. (b) $Sc = \{1, 8\}$, $Sc = \{1, 64\}$ and $Sc = \{8, 64\}$ at $R_\lambda \approx 8$. (c) $Sc = \{1/8, 1\}$ at $R_\lambda \approx 140, 240$ and 390 . Dashed line represents the large time limit in Eq. 5.3.	120
5.3	Coherency spectrum as defined in Eq. 5.4, where we normalized wavenumber by η_B of the less diffusive scalar. Lines A-F represent scalar pairs with $Sc = \{4, 8\}$, $\{4, 16\}$, $\{8, 16\}$, $\{16, 32\}$, $\{16, 64\}$, and $\{32, 64\}$ at $R_\lambda \approx 38$. Lines G-R represent scalar pairs with $Sc = \{1, 8\}$, $\{1, 64\}$, $\{8, 64\}$, $\{4, 16\}$, $\{4, 32\}$, $\{16, 32\}$, $\{64, 128\}$, $\{64, 256\}$, $\{128, 256\}$, $\{256, 512\}$, $\{256, 1024\}$ and $\{512, 1024\}$, respectively, at $R_\lambda \approx 8$. The curves “collapse” according to Sc ratio of the scalar pair.	121
5.4	PDFs of the difference in phase angle at $R_\lambda \approx 8$ between scalars: (a) $Sc = \{512, 1024\}$, (b) $Sc = \{256, 1024\}$, (c) $Sc = \{1, 8\}$, (d) $Sc = \{1, 64\}$. (a), (b) lines A-F represent $k = 6, 46, 86, 126, 166, 206$, respectively. (c), (d) lines A-F represent $k = 2, 12, 22, 32, 42, 52$, respectively.	122
5.5	Difference spectrum as defined in Eq. 5.6, where we normalized wavenumber by η_B of the less diffusive scalar. Lines A-L represent scalar pairs with $Sc = \{1, 8\}$, $\{1, 64\}$, $\{8, 64\}$, $\{4, 16\}$, $\{4, 32\}$, $\{16, 32\}$, $\{64, 128\}$, $\{64, 256\}$, $\{128, 256\}$, $\{256, 512\}$, $\{256, 1024\}$ and $\{512, 1024\}$, respectively, at $R_\lambda \approx 8$	123
5.6	Decomposition of the scalar transfer spectrum into contributions $T_\phi(k p)$ from velocity modes p in the logarithmic spaced ranges A-F in (a), (b), (c) and A-H in (d), where dashed lines are the overall scalar transfer $T_\phi(k)$. All from DNS data sets at $R_\lambda \approx 8$. (a) $Sc = 1, 128^3$. (b) $Sc = 8, 128^3$. (c) $Sc = 64, 128^3$. (d) $Sc = 1024, 512^3$	124
5.7	The same as FIG. 5.6, shown only for high wavenumbers.	125

5.8	Decomposition of scalar spectral transfer at $R_\lambda \approx 38$. (a) $T_\phi(k p, q)$, $Sc = 1$, dashed line for $T_\phi(k p)$, $1 \leq p \leq 2$, solid curves correspond to q at different ranges, (b) same as (a) for $Sc = 64$, (c) $T_\phi(k q)$, $Sc = 1$, dashed line for $T_\phi(k)$, (d) same as (c) for $Sc = 64$	126
5.9	Decomposition of scalar spectral transfer $T_\phi(k q, p)$ at $R_\lambda \approx 38$. (a) $Sc = 1$, dashed line for $T_\phi(k q)$ with $2 \leq q \leq 4$. (b) same as (a) for $Sc = 64$	127
5.10	Decomposition of scalar transfer spectrum $T_\phi(k)$ (dashed line) into fully resolvable transfer $T_\phi^{<<}(k k_c)$ (line A), resolvable-subgrid transfer $T_\phi^{><}(k k_c)$ (line B) and fully subgrid transfer $T_\phi^{>>}(k k_c)$ (line C). (a) $Sc = 1$ at $R_\lambda \approx 38$ (256^3), $k_c = 8$, (b) $Sc = 64$ at $R_\lambda \approx 38$ (512^3), $k_c = 22$	128
5.11	(a) Fully resolvable transfer $T_\phi^{<<}(k k_c)$ for $Sc = 64$ at $R_\lambda \approx 38$ at $k_c = 4, 16, 32, 64$ (lines A-D, respectively). (b) Same as (a) for subgrid transfer $T_\phi^s(k k_c)$. (c) Same as (a) for subgrid eddy diffusivity $D_e(k k_c)$	129
5.12	(a) Subgrid transfer $T_\phi^s(k k_c)$ for $Sc = 1, 8, 64$ (lines A-C) at $R_\lambda \approx 8$, $k_c = 8$. (b) Same as (a) at $k_c = 16$. (c) Subgrid diffusivity $D_e(k k_c)$ with the same parameters as (a). (d) Same as (c) at $k_c = 16$	130
5.13	Subgrid turbulent Schmidt number $Sc_t(k k_c)$ for $Sc = 16, 32, 64$ (lines A-C) at $R_\lambda \approx 38$	131
5.14	(a) Subgrid transfer $T_\phi^s(k k_c)$ (line A), its positive (line B) and negative contribution (line B and C) for $Sc = 64$ at $R_\lambda \approx 38$, $k_c = 4$. (b) Same as (a) at $k_c = 16$. (c) Corresponding decomposition of subgrid diffusivity $D_e(k k_c)$ with the same parameters as (a) (d) Same as (c) at $k_c = 16$	132
5.15	Same as FIG. 5.14 (a) and (b), respectively, for decomposition of fully subgrid transfer.	133

SUMMARY

A numerical study of fundamental aspects of turbulent mixing has been performed, with emphasis on the behavior of passive scalars of low molecular diffusivity (high Schmidt number Sc). Direct Numerical Simulation (DNS) is used to simulate incompressible, stationary and isotropic turbulence carried out at high grid resolution. Data analyses are carried out by separate parallel codes using up to 1024^3 grid points for Taylor-scale Reynolds number (R_λ) up to 390 and Sc up to 1024. Schmidt number of order 1000 is simulated using a double-precision parallel code in a turbulent flow at a low Reynolds number of $R_\lambda \approx 8$ to reduce computational cost to achievable level.

The results on the scalar spectrum at high Schmidt numbers appear to have a k^{-1} scaling range and agree very well with Kraichnan's (1968) model in the diffusive range as well. In the presence of a uniform mean scalar gradient, statistics of scalar gradients are observed to deviate substantially from Kolmogorov's hypothesis of local isotropy, with a skewness factor remaining at order unity as the Reynolds number increases. However, this skewness decreases with Schmidt number suggesting that local isotropy for scalars at high Schmidt number is a better approximation. Small scale intermittency seen in the flatness factor of scalar gradients and scalar dissipation tends to an asymptotic level at high Schmidt numbers. Intermittency exponents manifested by three types of two-point statistics of energy and scalar dissipation, i.e., the two-point correlator $\langle \chi(x)\chi(x+r) \rangle$, the second-order moment of local scalar dissipation $\langle \chi_r^2 \rangle$ and the variance of the logarithmic local scalar dissipation $\sigma_{\ln \chi_r}^2$ are discussed. These intermittency exponents are indicators of scalar intermittency in inertial-convective or viscous-convective ranges. Several basic issues in differential diffusion between two scalars of different molecular diffusivities transported by the same turbulent flow, the physical process of scalar spectral transfer and subgrid-scale transfer are also briefly addressed.

CHAPTER I

INTRODUCTION

1.1 Background

Turbulent flows are more important than laminar flows in the sense that turbulence commonly exist in nature and engineering applications. Turbulent motion can be found from astrophysical flow including interstellar cloud movement, plasma motion in the sun, to the Earth's atmospheric motion and atmospheric boundary layers, and to common observations such as the smoke stack motion from a chimney, the wake of a ship, the ocean current, flow over an aerodynamic surface, flow in a gasoline pipe as well as in chemically reacting flows in industrial processes. One of the most important characteristics of turbulent flows is irregularity, or randomness, which makes the deterministic approach of studying laminar flows inapplicable. In spite of the unpredictability and intractability of the instantaneous turbulent flow field, certain empirical laws can be extracted for the statistical properties of the turbulent fluctuation. The monograph *Statistical Fluid Mechanics* by Monin and Yaglom (Vol. II 1975) provides mathematical foundation for the statistical approach in turbulence research. Among the vast literature on turbulence, the seminal work of Kolmogorov (1941) on the similarity in small scales of turbulence has been greatly influential even 60 years later today.

It is well known that turbulent flows provide much more efficient mixing than laminar flows due to the fluctuations and randomness of velocity field. One of the important and desirable applications of turbulent mixing in industry is gaseous combustion, where the gas flow is often turbulent and the coupling between mixing and chemical reaction is a major challenge in combustion research (Turns 2000). The rate of chemical reaction of gaseous reactants is often controlled by the rate of turbulent mixing at the small scales. This thesis primarily focuses on the turbulent mixing of passive scalars, which are defined as diffusive contaminants that are chemically inert and present in such low concentrations that they

do not have dynamical effects on the turbulent flow (Warhaft 2000). Common examples of passive scalars are the concentration of certain substance in a turbulent flow or the temperature field in a weakly heated turbulent air jet. Passive scalars are distinguished by a non-dimensional parameter, i.e., Schmidt number (Sc) or Prandtl number (Pr). Sc is defined as the ratio between the kinematic viscosity (ν) and the molecular diffusivity when the scalar under investigation is a chemical species concentration. Similarly, Pr is the ratio between the kinematic viscosity and thermal diffusivity when temperature fluctuations are the object of study. In this work, Sc is used for the general purpose with no distinction between Sc and Pr .

Scalars at high Schmidt number are weakly diffusive with small molecular diffusivity. A fluorescent dye in flow visualization experiment is a common example of a weakly diffusive scalar where the color dye is expected to follow the fluid flow closely. For different color dyes, the degree of accuracy of the flow imaging result depends on the Schmidt number. In applications, Sc can vary widely from much less than unity in liquid metals with large molecular conductivities, to order one for most gaseous flows, and to the order of 1000 for color dyes and in some biological applications. Antonia and Orlandi (2003) give a thorough review on Schmidt number effects on the small-scale passive scalars of $Sc \gg 1$. For $Sc > 1$, scalar fluctuations arise at smaller scales than the velocity field. Batchelor (1959) and Kraichnan (1968) provide theoretical background for scalar mixing at $Sc > 1$, which is a major motivation for the work. For $Sc \leq 1$, scaling for scalar spectrum in inertial-convective range was proposed by Obukhov (1949) and Corrsin (1951). The present research emphasizes the high Sc regime of the scalar mixing, for which many important issues are still not well understood.

In this work, Direct Numerical Simulation (DNS) is used to study the properties of passive scalars. In the approach of DNS, the full range of scales in turbulent flows is resolved by solving the exact conservation equations of mass, momentum and passive scalars. The DNS approach to studying turbulent flows, despite its restriction to flows with simple geometries and low Reynolds number, can provide very detailed physical information about the small-scale structure which, in some cases, is very difficult to measure in experiments.

For instance, energy dissipation rate defined as $\epsilon \equiv 2\nu s_{ij}s_{ij}$, where the strain rate s_{ij} can be computed in DNS strictly according to the definition, whereas in experiments, it usually must be replaced by the one dimensional surrogate $15\nu(\partial u_1/\partial x_1)^2$. DNS also allows greater freedom in the choice of parameters and helps avoid the practical difficulties in handling some substances and fluids (e.g., mercury which has $Sc \ll 1$) in experiments. For $Sc \gg 1$, the smallest scales, the Batchelor scale ($\eta_B \equiv \eta Sc^{-1/2}$), that need to be resolved are much smaller than the smallest turbulence scale, namely, the Kolmogorov scale $\eta = (\nu^3/\langle\epsilon\rangle)^{1/4}$, where $\langle\epsilon\rangle$ is averaged energy dissipation rate. High resolution is therefore required, especially at high Reynolds number where η is very small. Batchelor's theory on weakly diffusive scalars only requires a large enough separation between η and η_B without requirement of high Reynolds number. This makes DNS a feasible approach to capture the fine scales of weakly diffusive scalars by keeping the Reynolds number relatively low (Bogucki *etal.* 1997, Brethouwer *etal.* 2003, Yeung *etal.* 2002, 2004).

In this work, the scalar field at Sc up to 1024 (Yeung *etal.* 2004) is simulated and analyzed on IBM SP parallel computers at San Diego supercomputing center. In addition to basic statistics such as the scalar spectrum, structure functions, statistics of scalar gradient, which were given in Yeung *etal.* (2002), statistics of scalar and energy dissipation taken at two different points in space are also computed at various Reynolds number and Schmidt number combinations. One of the more challenging tasks in this work lies in the calculation of the moments of local scalar dissipation χ_r , where χ_r is the averaged dissipation over a cube of linear size r as defined in Kolmogorov (1962). Averaging is taken over three-dimensional cubes of different size r strictly according to the definition, whereas in many numerical and experimental works, averaging is taken over a one-dimensional line of size r . Difficulties arise in parallel programming when data points belonging to a given sub-domain of a cube with linear size r are stored on different processors. In order to see the sensitivity of the results to the averaging methods, local dissipation averaged over one-dimensional, two-dimensional and three-dimensional spaces is all computed and compared. The DNS results show that intermittency exponent (see Sec.1.2) in intermediate range increases with averaging dimensions, but the values of the moments of local dissipation at fixed r in the

middle range decreases with averaging dimensions. The statistics mentioned above help to address the issues of local isotropy and intermittency and the Schmidt number effects. The issue of local isotropy at small scales in the context of Kolmogorov's (1941) hypothesis is of special interest for passive scalars when a mean scalar gradient is present. Reviews on this subject (Sreenivasan 1991, Warhaft 2000) have emphasized that passive scalars show first-order deviation from local isotropy for $Sc \sim O(1)$ even at very high Reynolds number. It is reasonable to speculate that, when $Sc \gg 1$, the separation between η and η_B plays an important role, and that the scalar fluctuations may be more nearly isotropic at higher Sc . Intermittency, as an important property in turbulence, refers to short-lived or localized bursts of intense fluctuations often associated with the small scales. Many studies based on experimental and numerical work (e.g., Sreenivasan and Antonia 1997, Overholt and Pope 1996) have shown that the passive scalar field is more intermittent than the velocity. An important issue is the nature of this behavior for $Sc \gg 1$. Some experimental data (Sreenivasan and Prasad 1989) have suggested a lack of intermittency in the Batchelor range between η and η_B .

In including more than one scalar in the simulations, it is possible to study differential diffusion at high Sc when two scalars with different Sc evolve differently (Bilger and Dibble 1982, Yeung 1996, 1998). In turbulent flames, Lewis number ($\equiv Sc/Pr$) is not unity. Differential diffusion is important because unequal mixing leads to non-uniformities in local stoichiometric conditions, which can cause inefficient combustion and increased formation of undesirable by-products (such as pollutants in the atmosphere). But in many models of turbulent combustion, multiple chemical species in reactions are assumed to have equal molecular diffusivity so that the Shvab-Zeldovich conserved-scalar approach can be used where a certain linear combination of the species concentration is conserved. The importance of accounting for differential diffusion effect in combustion models has been well recognized (Pope 1990).

The mechanisms of nonlinear interaction between different scales are essential in turbulence research. For passive scalars, triadic interactions between velocity and scalar modes are the key in the scalar transfer which affects the evolution of the scalar spectrum. Scalar

transfer is the net rate at which scalar fluctuations are transferred at one scale to another. Earlier work (Yeung 1996) has shown a local forward scalar transfer where the triadic interactions occur at about the same scales and scalar fluctuations are transferred from large to small scales. At high Sc , more contributions from high wave number interaction are expected. A detailed knowledge of spectral transfer is also important in subgrid scale modeling where a cut-off wavenumber is introduced to divide the flow into resolved scales ($k < k_c$) and subgrid scales ($k > k_c$). The work of Yeung and Zhou (1996) is extended to the high Sc regime. In Large Eddy Simulations, only the large scales of the turbulent motion are simulated and the small scales, or the subgrid scales are modeled. Subgrid-scale turbulent diffusivity and Schmidt number, which are directly related to subgrid scalar transfer provide pivotal information for scalar subgrid modeling (Moin *etal.* 1991). It would be useful to see the dependence of subgrid-scale turbulent diffusivity and Schmidt number on the molecular Sc . Further literature review is given in the following Sec. 1.2.

1.2 Literature Review

Because of the essential role in turbulent mixing, combustion and pollutant dispersion, passive scalar provides part of the motivation for the study of turbulence itself. The major impetus for study scalars in the high Schmidt number regime comes from the theoretical hypothesis of Batchelor (1959) and Kraichnan (1968), in which a κ^{-1} scaling for scalar spectrum in viscous-convective range $\eta^{-1} \ll \kappa \ll \eta_B^{-1}$ is proposed, where κ is the wave number. Review by Warhaft (2000) shows that the experimental support for the the κ^{-1} range has been elusive. Miller and Dimotakis (1996) in their turbulent jet experiment for $Sc \sim 2000$ found no κ^{-1} range. Williams *etal.* (1997) found the scalar spectrum fell well below κ^{-1} in magnetically forced two-dimensional turbulence for $Sc \sim 2000$. On the other hand, there also exists experimental evidence supporting the κ^{-1} range from color dye concentration spectrum (Nye and Brodkey 1967) to temperature spectrum in the ocean (Dillon and Caldwell 1980). Gibson and Schwarz (1963) and Prasad and Sreenivasan (1990) also support the existence of κ^{-1} scaling. Numerical results based on two-dimensional synthetic velocity field (Holzer and Siggia 1994) appear to support Batchelor scaling of the

scalar spectrum.

In turbulence research on scalar mixing, much attention has been given to scalars with $Sc \sim O(1)$, e.g., heat transport in the air with $Pr \sim 0.7$ (Sreenivasan 1991, Warhaft 2000). For $Sc \approx 1$, a well-known result on scalar spectra is the $\kappa^{-5/3}$ scaling in the inertial-convective range between the large turbulence scale L and the Obukhov-Corrsin scale $\eta_{OC} = \eta Sc^{-3/4}$ at high Reynolds number proposed by Obukhov (1949) and Corrsin (1951) as a direct extension of Kolmogorov (1941) scaling for energy spectra in the inertial range. The Obukhov-Corrsin $\kappa^{-5/3}$ scaling is generally supported in the literature (Sreenivasan 1996). But there are relatively few results on weakly diffusive scalars of $Sc \gg 1$, partly due to the high resolution requirement for both experiments and numerical simulations. Antonia and Orlandi (2003) give a detailed review on the Schmidt number effects with emphasis on the scalar spectrum and the related second-order scalar structure functions $\langle (\Delta_r \phi)^2 \rangle$, where ϕ is the scalar fluctuation and r is the separation distance between two locations. They suggest the κ^{-1} scaling in viscous-convective range is ambiguous.

Since the major requirement for Batchelor scaling is a relatively wide range of separation between η_B and η without the requirement for high Reynolds number, DNS study of weakly diffusive scalars is made possible by keeping the Reynolds number relatively low in order to reduce the computational cost. This approach has been used by several authors (Bogucki *etal.* 1997, Yeung *etal.* 2000, 2002, Orlandi and Antonia 2002, Brethouwer *etal.* 2003) in simulations of scalars of $Sc > 1$ in isotropic turbulence at relatively low Reynolds number. In particular, Brethouwer *etal.* (2003) reported data for $Sc = 144$ at Taylor Reynolds number $R_\lambda \approx 20$. Gotoh *etal.* (2000) studied two-dimensional turbulence for $Sc = 1000$ at $R_\lambda \approx 3$. The main results for the work presented in this thesis are for Sc up to 64 at $R_\lambda \approx 38$ and Sc up to 1024 at $R_\lambda \approx 8$.

Unlike the velocity field, the scalar field shows strong evidence for departure from local isotropy predicted by Kolmogorov (1941) similarity hypothesis (Sreenivasan 1991, Warhaft 2000, Lumley and Yaglom 2001). The $\kappa^{-5/3}$ Kolmogorov and Obukhov-Corrsin scalings for velocities and scalars are based on the assumption that in the limit of infinite Reynolds number, scalars and velocities are isotropic at small scales. Local isotropy requires that

the odd order moments of scalar gradients vanish due to symmetry of scalar gradient fluctuations. Evidence for $Sc \sim O(1)$ (Shen and Warhaft 2000, Schumacher 2001) strongly suggests local anisotropy in the presence of mean scalar gradient at the level of third order moments up to seventh order. The deviation from local isotropy is believed to stem from the ramp-cliff structure of the scalar fluctuations (Gibson 1977, Sreenivasan and Antonia 1977). Considering the statistical uncertainty of higher order moments, the normalized third order moment, i.e., the skewness of scalar gradient is among the most important indicators of local anisotropy. It is reasonable to speculate that the scalar field may be more locally isotropic at high Sc because Batchelor scale η_B is less than than η and is further removed from the large scales, i.e., scalars at high Sc has wider range of scales than those at low Sc in the same turbulent flows. Schumacher *etal.* (2003) provides upper bound for derivative moments of scalar based on the approach of Batchelor (1959), in which the upper bounds for derivative moments of order n are shown to grow as $Sc^{n/2}$ for high Sc . Furthermore, combination of analytical and numerical results from his paper suggests that the normalized moments decrease with Sc , at least for odd orders.

Another important phenomenon that generally exist in turbulent flows is the concept of intermittency, which refers to sporadic large fluctuations that are localized in space. An intermittent signal is not self-similar. For example, a typical self-similar Gaussian random process displays a similar image for any portion of the signal. However, an intermittent process may have very strong signals in some portions whereas stay inactive for other portions. Intermittency implies that there are occasional large deviations from the mean value of the turbulent fluctuations. Such extremal events in statistics can be captured by normalized high-order moments, e.g., the flatness factor $F_4 = \langle v^4 \rangle / \langle v^2 \rangle^2$ of a turbulent quantity v . For self-similar and Gaussian signals, the flatness factor is usually small. In fact, $F_4 = 3$ for Gaussian process has been used as a benchmark for detecting intermittency. Intermittent turbulent quantities have a higher value of flatness factor due to the contribution from the “spikes” in the signal. For instance, flatness factor of turbulent dissipation rate is usually of order 10. Small-scale intermittency can be captured by the distribution and normalized even-order moments of such small-scale quantities as gradients, time derivative and

dissipation rate etc.

Kolmogorov's (1941) theory implies that turbulence is self-similar in inertial range, which is appreciably different from observation (Frisch 1995). The observed discrepancies between K41 theory and experiments have led to the development of Refined Similarity Hypothesis (Kolmogorov 1962). The discrepancies account for the intermittency effects in inertial range. For example, K41 theory predicts that the velocity structure function of order p over a separation distance l in inertial range grows as a power law of l with an exponent $p/3$, and more generally, it can be written as

$$\langle (\Delta v_{\parallel}(l))^p \rangle \propto l^{\zeta_p}. \quad (1.1)$$

Many experimental results show discrepancy of intermittency exponent ζ_p from $p/3$ predicted by K41 (Van Atta and Chen 1970, Anselmet *etal.* 1984). Other indicators of inertial range intermittency are based on statistics of the energy dissipation rate. In particular, local energy dissipation averaged over a sphere of size l follows the scaling

$$\langle \epsilon_l^p \rangle \propto l^{\tau_p}. \quad (1.2)$$

Under Obukhov's hypothesis (Obukhov 1962 or Frisch 1995), the two intermittency exponents ζ_p and τ_p based on velocity and energy dissipation, respectively, are related by

$$\zeta_p = p/3 + \tau_{p/3}. \quad (1.3)$$

Consequently, given measurement of either ζ_p or τ_p , the other can be deduced. The prediction of the intermittency exponents have been much investigated and many models are developed such as Kolmogorov's (1962) lognormal model, the β model (Frisch *etal.* 1978) and bi-fractal model, the multifractal model (Meneveau and Sreenivasan 1987,1991), and the mapping closure model (She and Orszag 1991). Borgas (1992) suggests that the multifractal model gives the most satisfactory predictions.

Experimental and numerical studies (Sreenivasan and Antonia 1997, Overholt and Pope 1996, Vedula *etal.* 2001) generally show that scalar field is more intermittent than velocity field. Moreover, even for a strictly Gaussian velocity field without intermittency, the scalar field is still intermittent (Kraichnan 1994). In this work, attempt is made to investigate

scalar intermittency as a function of Sc and the size of the scales. For scalars at high Sc , intermittency scaling in the viscous-convective range may exist. In particular, the scaling of local scalar dissipation χ_r over a cube of size r and the possible intermittency exponents in viscous-convective range are also studied. In the literature, two-point correlator $\langle \epsilon(x)\epsilon(x+r) \rangle$, which has equivalent scaling as $\langle \chi_r^2 \rangle$ (Sreenivasan and Kailasnath 1993), is often studied for intermittency exponents. In this work, the two-point correlator of energy and scalar dissipation are also calculated for comparison.

Energy transfer is an important physical process influencing the evolution of energy spectrum. In the transport equation for energy spectrum, the non-linear energy transfer causes the closure problem and is usually modeled as a function of energy spectrum through various hypothesis (Monin and Yaglom 1975). Domaradzki and Rogallo (1990) studied the energy transfer through local and non-local interactions using DNS and showed excellent agreement with the prediction based on eddy-damped quasnormal Markovian theory (EDQNM). However, the process of scalar transfer that appears in the equation of scalar spectrum is less investigated. Yeh and Van Atta (1973) provided some one-dimensional measurements. Yeung (1996) studied the triadic interactions of scalar transfer by extending the technique of computing energy transfer used by Domaradzki and Rogallo (1990) to scalar transfer. In this work, the work of Yeung and Zhou (1996) is extended to high Schmidt numbers.

Scalar subgrid transfer used in LES for solving the scalar transport equation has been modeled based on different approaches (Moin *et al.* 1991, Zhou and Vahala 1993, Pullion 2000). Lesieur and Rogallo (1989) performed LES using a subgrid viscosity proposed by Kraichnan (1976) and subgrid diffusivity from EDQNM theory. Detailed process of subgrid transfer has also been studied using numerical simulation by various authors (Domaradzki *et al.* 1987, 1993, Yeung and Zhou 1996). In this work, scalar subgrid transfer at high Sc based on Yeung and Zhou (1996) are studied by DNS.

The importance of differential diffusion has been well acknowledged (Bilger and Dibble 1982, Pope 1990). Saylor and Sreenivasan (1998) performed experiments using color dyes and showed significant differential diffusion effects even at scales much larger than the Batchelor scale. Smith *et al.* (1995) studied differential diffusion in turbulent jets of

H_2/CO_2 mixing with air suggesting that high-order statistics may be affected by differential diffusion even at high Reynolds number. Other experimental studies reported measurements on the coherency spectrum (Tong and Warhaft 1995, Sirivat and Warhaft 1982). Numerical simulations on differential diffusion include Yeung and Pope (1993), Yeung (1996), Nilsen and Kosály (1998). This thesis extends the studies in Yeung and Pope (1993), Yeung (1998) to high Sc regime.

1.3 Outline

The remaining thesis is organized as follows: Chapter 2 gives the numerical method of DNS, simulation parameters and data analysis. Basic statistics including scalar spectrum, structure functions and scalar gradient are discussed in Chapter 3, where local isotropy and its dependence on Sc are evaluated. In Chapter 4, discussions of scalar intermittency through various indicators such as the kurtosis and probability density function of scalar gradient, dissipation, structure functions are presented. Two-point statistics of energy and scalar dissipation as a function of Re , Sc and separation distance r are also discussed. In particular, the two-point correlator $\langle \chi(x)\chi(x+r) \rangle$, the second order moment of local dissipation $\langle \chi_r^2 \rangle$ and the variance of logarithmic local dissipation $Var(\ln \chi_r)$ are analyzed and compared, their corresponding intermittency exponents are computed and discussed. Chapter 5 present results on differential diffusion between two scalars, scalar transfer and sub-grid transfer at various Sc . Finally, conclusions and future work on weakly diffusive scalars are discussed in Chapter 6.

In the appendices, abstracts from relevant journal papers and conference meeting are attached. Appendices A and B are based on the DNS data for high Schmidt numbers at $R_\lambda \approx 38$ and 8, respectively, where most of the results are included in Chapter III. The conference paper in appendix C is on the Lagrangian statistics of three-particle dispersion. The conference presentation in appendix D studies the dispersion problem of molecules (scalars) by Lagrangian approach, where the velocities of molecules are modeled as the combination of the velocities of the fluid particles and 3-D Brownian motions. The work in appendices C and D is not included in this thesis.

CHAPTER II

NUMERICAL METHOD OVERVIEW

In this work, Direct Numerical Simulation is used to provide instantaneous velocity and scalar fields on a three-dimensional computational domain. Data from DNS are then analyzed by separate post-processing code. Section 2.1 reviews the techniques used in the DNS code. In Sec. 2.2, the methods of data analysis and simulation parameters are described.

2.1 Direct Numerical Simulation

In this thesis, stationary isotropic turbulence is simulated using a parallelized version of Rogallo's (1981) pseudo-spectral algorithm. Periodic boundary conditions are applied to turbulent fluctuations over a cube of length 2π units on each side. Turbulent velocity and scalar fields are both maintained statistically stationary in time, which allows multiple realizations of the flow field at different times to be treated as different samples for the purpose of ensemble averaging. In the absence of energy input, homogeneous, isotropic turbulence will decay due to viscous dissipation. An artificial forcing at the large scales is used to obtain stationarity. Various forcing schemes based on deterministic or stochastic approaches have been developed for DNS and no general consensus on what is the best scheme has been reached (Overholt and Pope 1998). On the other hand, details of forcing schemes do not alter the statistics of the small scales significantly (Sreenivasan 1998). Eswaran and Pope's (1988) stochastic forcing scheme is used in this work, which has been used by various authors.

The governing equations for incompressible turbulent flow are the continuity equation, momentum or Navier Stokes equations and the transport equation for passive scalars written as follows:

$$\frac{\partial u_i}{\partial x_i} = 0 \tag{2.1}$$

$$\frac{\partial u_i}{\partial t} + u_j \frac{\partial u_i}{\partial x_j} = -\frac{1}{\rho} \frac{\partial p}{\partial x_i} + \nu \frac{\partial^2 u_i}{\partial x_j \partial x_j} \tag{2.2}$$

$$\frac{\partial \phi}{\partial t} + u_j \frac{\partial \phi}{\partial x_j} = -u_j \frac{\partial \Phi}{\partial x_j} + D \frac{\partial^2 \phi}{\partial x_j \partial x_j} \quad (2.3)$$

where u_i ($i = 1, 2, 3$) denotes the velocity component along x_i direction, p is the pressure fluctuation and ϕ is the scalar fluctuation. The constant coefficients ν and D are the kinematic viscosity and molecular diffusivity, respectively, and Φ is the mean scalar field.

In this work, scalar field is also maintained stationary by velocity fluctuations acting upon the mean scalar gradient. The evolution of the scalar variance follows

$$\frac{\partial \langle \phi^2 \rangle}{\partial t} = -2 \langle u_j \phi \rangle \frac{\partial \Phi}{\partial x_j} - \langle \chi \rangle, \quad (2.4)$$

where $\langle \chi \rangle = 2D \langle (\partial \phi / \partial x_i)^2 \rangle$. In stationary state, the production term caused by the correlation of velocity and scalar fluctuations acting on the mean scalar gradient and the scalar dissipation term on the RHS are in balance with each other. For a homogeneous scalar field, the terms in Eq. 2.4 should be independent of spatial coordinates, which implies that the mean scalar gradient should be constant. In this work, a uniform mean scalar gradient $\nabla \Phi = (1, 0, 0)$ is used for all cases, where different choices of the magnitude of the mean scalar gradient will not alter the normalized statistics, neither does the direction of the mean scalar gradient affect the statistics due to isotropy. The introduction of a uniform mean scalar gradient in DNS helps maintain a stationary scalar field for the ease of ensemble averaging over multiple times. However, I realize that in experiments, the mechanisms of maintaining such a uniform mean scalar gradient can hardly be realistic. In the simulations, scalars are introduced into the flow after the velocity field has attained stationarity, starting with zero scalar fluctuations. After the scalar field reaches stationary state, the simulation is continued for of order 10 eddy turnover times in order to obtain multiple realizations of data field at appropriate time intervals. Data are extracted and analyzed at time interval of about one eddy turnover time, and processed as independent samples in ensemble averaging of multiple realizations (e.g. Yeung 1998).

Direct numerical simulation using spectral methods gives greater accuracy in the evaluation of the spatial derivatives in the Navier-Stokes equations compared to finite-difference methods. The conservation equations are solved in Fourier spectral space. After taking Fourier transforms of Eq. 2.1 – 2.3, the obtained the continuity equation, the momentum

equations and the scalar equation in Fourier space can be written as

$$k_j \hat{u}_j(\mathbf{k}, t) = 0, \quad (2.5)$$

$$\frac{d\hat{u}_j(\mathbf{k}, t)}{dt} = -\nu k^2 \hat{u}_j(\mathbf{k}, t) - ik_i P_{jm}(\mathbf{k}) \sum_{\mathbf{k}'} \hat{u}_m(\mathbf{k}', t) \hat{u}_i(\mathbf{k} - \mathbf{k}', t), \quad (2.6)$$

$$\frac{d\hat{\phi}(\mathbf{k}, t)}{dt} = -Dk^2 \hat{\phi}(\mathbf{k}, t) - \frac{\partial \Phi}{\partial x_j} \hat{u}_j - ik_j \sum_{\mathbf{k}'} \hat{u}_j(\mathbf{k}', t) \hat{\phi}(\mathbf{k} - \mathbf{k}', t), \quad (2.7)$$

where \mathbf{k} and \mathbf{k}' are wavenumber vectors, $i = \sqrt{-1}$, and $P_{jm}(\mathbf{k}) \equiv \delta_{jm} - k_j k_m / k^2$ is the projection tensor in wavenumber space.

In applying forcing, an additional term is added to Eq. 2.6 in the form

$$\frac{\partial \hat{\mathbf{u}}(\mathbf{k}, t)}{\partial t} = \hat{\mathbf{a}}(\mathbf{k}, t) + \hat{\mathbf{a}}^F(\mathbf{k}, t), \quad (2.8)$$

where $\hat{\mathbf{a}}(\mathbf{k}, t)$ represents the RHS of Eq. 2.6 and $\hat{\mathbf{a}}^F(\mathbf{k}, t)$ is the forcing term. Following Eswaran and Pope (1988), $\hat{\mathbf{a}}^F(\mathbf{k}, t)$ is non-zero only at large scales for all modes with a sphere of radius k_F centered at the origin (excluding the node at the origin), i.e., for all modes with magnitude of wavenumber satisfying $0 < k < k_F$. The k_F is normally chosen to be $\sqrt{2}$, 2 or $2\sqrt{2}$. The specification of the forcing term is based on Uhlenbeck-Ornstein (UO) random processes. A complex vector-valued stochastic process is formed based on combination of 6 independent UO processes with the same specified variance and time-scale. Projection of this vector process onto the plane normal to \mathbf{k} gives the forcing term $\hat{\mathbf{a}}^F$. Mathematical details can be found in Eswaran and Pope (1988).

A fully-spectral method for evaluating the convolution terms in Eq. 2.6 and Eq. 2.7 would require of order N^6 operations (each wavenumber mode involves N^3 multiplications, hence the total number of operations for all grid points N^6). To avoid this large cost, in pseudo-spectral method, the nonlinear terms in the Navier-Stokes equations are evaluated by first transforming the velocity field to physical space where the nonlinear terms $u_i u_j$ are formed and then transformed back to Fourier space. The computational cost for this procedure by multiplication is of order $N^3 \log N$ in operations. However, this procedure causes aliasing errors and the aliased terms with high wavenumbers are added to the low wavenumber terms in Fast Fourier Transform (FFT) algorithm which is used in the DNS code. In Rogallo's

(1981) scheme, aliasing errors are minimized by a combination of truncation and phase shifting methods.

The task is to solve Eqs. 2.6 and 2.7 as ordinary differential equations in time. A second-order Runge-Kutta method is used in predictor-corrector form. In the predictor step, a predictor velocity $\hat{\mathbf{u}}^*$ is estimated by

$$\hat{\mathbf{u}}^* = \hat{\mathbf{u}}(t_n) + \Delta t \hat{\mathbf{a}}(\hat{\mathbf{u}}(t_n)) \quad (2.9)$$

In the corrector step, an improved approximation is obtained by

$$\hat{\mathbf{u}}(t_{n+1}) = \hat{\mathbf{u}}(t_n) + \frac{\Delta t}{2} [\hat{\mathbf{a}}(\hat{\mathbf{u}}(t_n)) + \hat{\mathbf{a}}(\hat{\mathbf{u}}^*)] \quad (2.10)$$

For each time step, the predictor-corrector method requires four sets of Fourier transforms per flow variable, which are carried out by using machine optimized FFT software library. Fourier transforms are the most CPU expensive operations in the DNS code. In parallel computing as described further below, the communication time among all the processors also becomes a bottleneck, especially when the number of processors is large.

In an explicit time-advancement scheme, the size of time step is subject to a Courant number restriction necessary for numerical stability. In three-dimensions, the Courant number is defined as

$$C \equiv \left[\frac{|u|}{\Delta x} + \frac{|v|}{\Delta y} + \frac{|w|}{\Delta z} \right]_{max} \Delta t \quad (2.11)$$

where the maximum is taken over all grid points in physical space, u , v , and w are Cartesian velocity components and Δx , Δy and Δz are grid spacing in corresponding directions. In finite difference methods, explicit scheme usually requires Courant number less than unity in order to maintain numerical stability. Although no theoretical constraints of numerical stability in spectral method is known, Eswaran and Pope (1988) suggested that $C \leq 1$ is a necessary condition. In the simulation, Courant numbers at 0.6 or less is used to ensure stability. The tests also show that smaller Courant number should be used in simulating high- Sc scalars to avoid errors.

It is well-known that DNS approach is computationally intensive, especially at high Reynolds numbers. This is because the range of scales grows fast with increasing Reynolds

number, which means for the fixed largest scale, flows with higher Reynolds number have smaller dissipation scales, hence requires higher grid resolution. The required number of grid points increases as a power law of Reynolds number, i.e., $N^3 \sim R_\lambda^{9/2}$, where R_λ is the Reynolds number based on Taylor scale. DNS has to resolve all scales of turbulent flow, and hence resolution of the smallest scales is critical. An empirical criterion used in the simulations is $k_{max}\eta \geq 1.5$ for velocity field, where $k_{max} = \sqrt{2}N/3$ is the highest wavenumber resolved on an N^3 grid. For scalars of high Sc , the smallest scale η_B that needs to be resolved is smaller than η and resolution requirements for $Sc > 1$ are more demanding than those for velocity field. In other words, resolution requirement increases with both Reynolds number and Schmidt number for scalar field. One possible approach in simulating scalars at high Sc is to keep Reynolds number relatively low. In this work, the results include $Sc = 64$ at $R_\lambda \approx 38$ and $Sc = 1024$ at $R_\lambda \approx 8$, both with 512^3 grid points.

High-resolution DNS requires both longer CPU time and larger memory storage. The work in this thesis has been performed on IBM SP parallel computers at San Diego Supercomputer Center with resolution up to 512^3 . The parallel algorithms are based on a single-program multiple data (SPMD) approach suitable for distributed-memory parallel computers. Every processor runs the same code but operates on different sub-domain stored in its own memory. Distributed-memory computers are in contrast to shared-memory computers, in which all processors share the same memory but different processor may run different codes. Because of the large memory requirement in high-resolution DNS, distributed-memory computers are chosen. In the parallel DNS code, the three-dimensional cubic domain is evenly divided into a number of slabs in $x - y$ or $x - z$ plane, with the number of slabs equal to the number of processors. Data on each slab are stored in a different processor. Communication between processors is required when it is necessary for each processor to have access to the data stored on other processors. Such necessity arises when Fourier transforms are taken in y direction for data divided into $x - z$ slabs, because for data on $x - z$ slabs, Fourier transforms can only be taken in x and z directions. Each slab has only part of the data in y direction which is insufficient for Fourier transforms. In the DNS algorithm (see Yeung and Moseley 1995 for details), data are transposed between

$x - y$ and $x - z$ slabs in order to take Fourier transform in the third direction perpendicular to the original slab. This is accomplished by packing the data on each slab into “pencils” of data with the number of “pencils” equal to the number of processors, and each processor exchanges a “pencil” of data with another. This task of data exchanges is implemented using a portable standard Message Passing Interface (MPI). The tests show that the percentage of communication time spent on data transposition increases with the number of processors, and communication becomes the most time-consuming operation in high-resolution simulations. In the parallel DNS code, data are divided evenly among processors which execute the same operations and participate equally in communications, except that the output is usually written by just one of the processors. This way of even distribution of workload improves parallel efficiency.

The number of processors used in the DNS runs is based on considerations for the total CPU time and memory usage. The number of processors must be large enough so that the memory usage on each processor does not exceed the memory limit, since usage close to the limit can greatly reduce performance efficiency due to paging in the computer memory. Fixed arrays of large size and dynamic memory allocations are efficiently used to minimized the memory usage. On the other hand, using too many processors leads to a reduction in parallel efficiency (ratio between speedup and the number of processors) because of increased time spent in communication calls, especially for larger grid-resolutions.

2.2 Data Analysis and Simulation Parameters

In this sub-section, the data analysis of the turbulent flow fields produced from DNS are discussed, with emphasis on the methods used to calculate the statistics of locally averaged dissipation rate on parallel computers. Descriptions of the simulation parameters are also presented.

In this work, the velocity and scalar fields are statistically stationary in time, although substantial temporal variations of space-averaged statistics such as turbulence kinetic energy can occur (e.g., Overholt and Pope 1996). Stationarity allows data taken at different times to be used as multiple realizations for the purpose of ensemble averaging. In the DNS,

the three-dimensional velocity and scalar fields are saved at time intervals of about one eddy-turnover time (the ratio of longitudinal integral length scale to r.m.s. velocity) for the purpose of post-processing. One eddy-turnover time is chosen such that data at different times are statistically independent. The data from DNS are analyzed by separate post-processing codes.

The computation and sampling of local averages, such as the average local energy dissipation in a cube of linear size r , i.e., ϵ_r , is a non-trivial task that warrants some discussion. From a theoretical point of view (Kolmogorov 1962), in locally isotropic turbulence, or at least for scale sizes r much smaller than the integral length scales, it is best to average over a sphere of radius r , which in practice for Cartesian geometries is replaced by a cube of length r on each side. In experiments such 3-D box averages are generally not available and are routinely replaced by 1-D averages along a line of length r . However, most previous results from DNS (e.g. Chen *etal.* 1993, Wang *etal.* 1996) were also based on line averaging even though full three-dimensional fields are available in the simulations. Although some arguments can be made for the physics of using line averages of ϵ taken along the separation vector in the scaling of velocity structure functions (Wang *etal.* 1996), the main consideration has been CPU expense.

The CPU expense can be traced to the fact that in distributed-memory parallel codes the solution domain is divided among the processors as slabs of equal size. Each cubic box involved in a local average contains a number of grid planes, which in general may be spread over more than one slab. Partial sums are calculated on each processor that contains the data and final result is obtained by a communication call, which is time-consuming especially if a large number of processors must be used to accommodate the overall memory requirements for a given grid resolution. Since one communication call is required for every sample of the box average, the CPU cost is especially high for small boxes (i.e. small r) for which numerous samples exist in the solution domain. However, for large data sets (such as 1024^3) a great improvement is possible if memory constraints can be circumvented in order to allow the data analysis to be carried out using only a small number of processors (say 32 for 1024^3 versus 512 needed by the DNS code). This is achieved by first writing 3-D fields

of flow variables of interest (e.g. ϵ) onto external files and then running a stand-alone code which needs to hold only one variable at a time for the sole purpose of obtaining box-average statistics.

In order to save CPU time and simplify the algorithm, only non-overlapping boxes are considered where r is an integer multiple of the grid spacing and is varied in powers of 2: i.e. $r = 2^n \Delta x$, where $n = 0, 1, \dots$, up to $\ln_2(N)$. While statistics for large boxes (which are relatively few in number) may be subject to sampling limitations, inclusion of overlapping boxes would not result in much improvement because the overlap would reduce the degree of statistical independence among different samples for the same box size. On the other hand, because intermittency exponents are inferred from the slopes of linear regimes in log-log plots, the restriction to logarithmically spaced values of r does not have a great effect on the data quality.

The calculation of one- and two-dimensional averages and two-point correlators is much simpler, requiring communication calls only in collecting global statistics but not in forming individual samples. Comparisons are made for local averages computed in one dimension along a line, in two dimensions over a square, and in three dimensions over a box, all with the same linear dimension r . For the two-point correlator $\langle \epsilon(\underline{x})\epsilon(\underline{x} + \underline{r}) \rangle$ there is no difficulty in varying the distance r linearly (instead of logarithmically) along each coordinate axis. In isotropic turbulence, average is taken over three components and the result can be written in simpler notation as $\langle \epsilon(x)\epsilon(x+r) \rangle$, where r is taken to be $\Delta x, 2\Delta x, 3\Delta x, \dots$, etc. However, because homogeneity and periodic boundary conditions imply that two-point correlators are even functions of r , results are presented only for r up to half of the length of each side of the solution domain.

Major simulation parameters are summarized in Tables I-III. The simulations can be divided into three groups. In the first, the Schmidt number is varied from 1 to 64 while the Taylor-scale Reynolds number R_λ is kept approximately constant at 38. Table II gives the simulation parameters at $R_\lambda \approx 8$ with Sc varied from 1 to 1024. Part of the interest in scalar mixing at $Sc = 1024$ is that $Sc \sim 1000$ corresponds to the regime of color dyes used in fluid visualization experiments. Questions may arise as to whether turbulence at such

low Reynolds number may have proper scalings, at least for Kolmogorov's first hypothesis. It is known that several authors have reported simulation results at R_λ below 20. For instance, Brethouwer *etal.* (2003) presented limited data at $Sc = 144$ and $R_\lambda \approx 20$. Chen *etal.* (1993) studied far-dissipation range where $k\eta \gg 1$ at $R_\lambda \approx 15$. Gotoh *etal.* (2000) reported results at $Sc = 1000$ and $R_\lambda \approx 3$ in two-dimensional turbulence. Simulations in this work show (FIG. 2.1) that there is a good collapse of the energy spectrum in Kolmogorov scaling for R_λ at 8 and 38. This result suggests that the high- Sc scalar field driven by the dissipation-range motions in this flow is still physically realistic. However, it should be pointed out that the forcing at large scales at such a low Reynolds number may have some effects on the DNS results and it will be useful to compare with the cases without forcing for a decaying turbulence. Since the main objective of studying high- Sc scalars is to understand the behavior in viscous-convective range, which does not require a high Reynolds number, simulations at $R_\lambda \approx 8$ still provide insightful results for scalars. Caution is taken in simulating turbulence at such a low R_λ , where energy spectrum at very high wavenumbers falls to values so small that round-off errors become significant. To alleviate this problem, a double precision version of the DNS code is used, although at the cost of more memory requirements and somewhat larger CPU time per time step. In the third series of simulations, Reynolds number effects are addressed for $Sc \leq 1$. Simulation parameters at $R_\lambda \approx 140, 240$ and 390 are given in Table III. Energy spectra at $R_\lambda \approx 240$ and 390 appears to have a well-defined inertial range. The resolution criterion for $Sc > 1$ is that parameter $k_{max}\eta_B$ should be at least 1.5, where $k_{max} = \sqrt{2}N/3$ is the highest wavenumber resolved on an N^3 grid. Tables I and II show that this criterion is met for all $Sc \geq 1$. For simulations at $R_\lambda 140, 240$ and 390 , the corresponding criterion is that $k_{max}\eta$ should be no less than 1.5, although Table III shows $k_{max}\eta$ is slightly less than 1.5 in the high- re runs.

It can be seen from Tables I and II that, for fixed velocity parameters, scalar variance $\langle \phi^2 \rangle$ increases with Sc , while the scalar dissipation rate $\langle \chi \rangle$ remains nearly constant. When the scalar field is statistically stationary, balance between production of scalar variance due to the mean gradient and dissipation by molecular action requires that

$$-2\rho_u\phi u'\phi'G = \langle \chi \rangle, \quad (2.12)$$

where the primes denote root-mean-square fluctuations, and $\rho_{u\phi}$ is the velocity-scalar correlation coefficient. Tables I and II show that the magnitude of $\rho_{u\phi}$ decreases as Sc increases. Tables I-III also give the ratio of the mechanical time scale to the scalar time scale, $r_\phi = (K/\langle\epsilon\rangle)/(\langle\phi^2\rangle/\langle\chi\rangle)$, where K is the turbulent kinetic energy. The ratio r_ϕ is an important parameter in many studies of turbulent mixing (e.g., Warhaft and Lumley 1978, Eswaran and Pope 1988). In simplified mixing models, r_ϕ is often set to be 2 (Pope 2000). This ratio r_ϕ is also related to the time ratio between scalar Taylor time scale and Kolmogorov time scale (see Yeung and Sawford 2002 for details). Table III for high- R_λ simulations at $Sc \leq 1$, r_ϕ is between 2 and 3, which has very weak dependence on R_λ , but for high- Sc scalars at $R_\lambda \approx 38$ and 8, Tables I and II clearly show that r_ϕ decreases with Sc . For $R_\lambda \approx 8$, r_ϕ decreases from 0.96 at $Sc = 1$ to 0.17 at $Sc = 1024$, and it becomes systematically lower at high Sc . Thus, Schmidt number effects should be incorporated in modeling.

Table 2.1: Simulation parameters at $R_\lambda \approx 38$

N	256	256	256	256	512	512	512
R_λ	38	38	38	38	38	38	38
Sc	1	4	8	16	16	32	64
$k_{max}\eta$	6	6	6	6	12	12	12
$k_{max}\eta_B$	6	3	2	1.5	3	2	1.5
$\langle\phi^2\rangle$	2.1	3.1	3.6	4.1	4.0	4.5	5.0
$\langle\chi\rangle$	2.5	2.8	2.8	2.8	2.7	2.7	2.7
$\rho_{u\phi}$	-0.5	-0.5	-0.5	-0.4	-0.5	-0.4	-0.4
r_ϕ	1.6	1.3	1.1	1.0	1.0	0.9	0.8

Table 2.2: Simulation parameters at $R_\lambda \approx 8$

N	128	128	128	128	128	128	256	256	256	512	512	512
R_λ	8	8	8	8	8	8	8	8	8	8	8	8
Sc	1	4	8	16	32	64	64	128	256	256	512	1024
$k_{max}\eta_B$	12	6	4	3	2	1.5	3	2	1.5	3	2	1.5
$\langle\phi^2\rangle$	1.7	3.2	4.1	5.0	6.0	7.0	6.5	7.5	8.4	10	11	12
$\langle\chi\rangle$	2.1	2.3	2.4	2.4	2.4	2.4	2.3	2.2	2.2	2.5	2.5	2.4
$\rho_{u\phi}$	-0.7	-0.5	-0.5	-0.4	-0.4	-0.4	-0.4	-0.4	-0.3	-0.4	-0.3	-0.3
r_ϕ	1.0	0.6	0.4	0.4	0.3	0.3	0.3	0.2	0.2	0.2	0.2	0.2

Table 2.3: Simulation parameters at higher Reynolds numbers

N	256	256	512	512	1024	1024
R_λ	140	140	240	240	400	400
Sc	1/8	1	1/8	1	1/8	1
$k_{max}\eta$	1.4	1.4	1.4	1.4	1.4	1.4
$k_{max}\eta_{OC}$	7	1.4	6.6	1.4	6.5	1.4
$\langle\phi^2\rangle$	1.7	2.3	3.2	3.7	2.7	2.9
$\langle\chi\rangle$	2.0	2.0	3.3	3.3	2.5	2.4
$\rho_{u\phi}$	-0.6	-0.5	-0.6	-0.6	-0.6	-0.6
r_ϕ	3.1	2.4	2.7	2.3	2.5	2.3

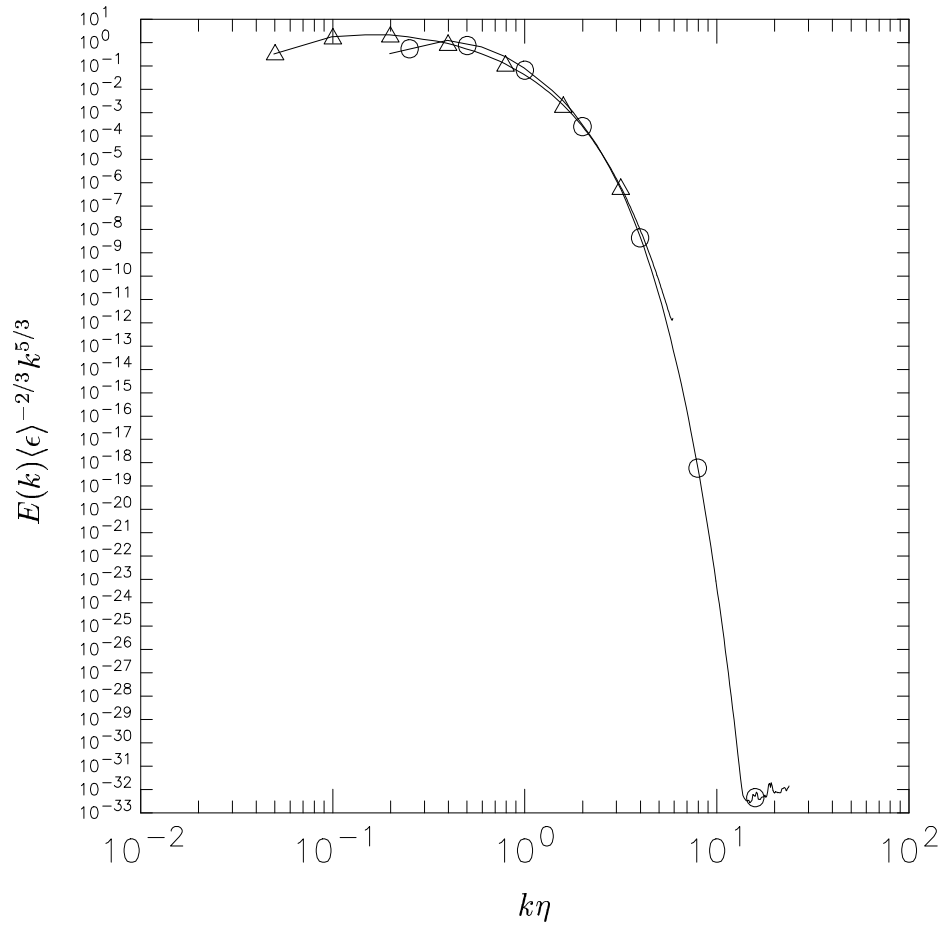


FIGURE 2.1. Comparison of Kolmogorov-scaled energy spectrum at $R_\lambda \approx 38$ (Δ) and $R_\lambda \approx 8$ (\circ), using double precision code.

CHAPTER III

SCALING PROPERTIES AND SMALL-SCALE CHARACTERISTICS

In this chapter, results based on scalar spectrum and structure functions are presented. In the latter part, discussions are made on the issues of local isotropy and intermittency and their Schmidt number dependence.

3.1 Scalar spectrum and structure functions

A. Moderately diffusive scalars

For scalars with $Sc \leq 1$, effects of molecular diffusion are dominant for scales smaller than the Obukhov-Corrsin scale, $\eta_{OC} = \eta Sc^{-3/4}$. Under similar high Reynolds number arguments as those of Kolmogorov (1941), Obukhov (1949) and Corrsin (1951) predicted the scalar spectrum in inertial convective range of wavenumbers $1/L \ll k \ll 1/\eta_{OC} \leq 1/\eta$ has the form

$$E_\phi(k) = C_\phi^* \langle \chi \rangle \langle \epsilon \rangle^{-1/3} k^{-5/3}, \quad (3.1)$$

where C_ϕ^* is the Obukhov-Corrsin constant in three-dimensional spectrum. To compare the DNS data with Eq. 3.1, Fig. 3.1 shows the “compensated” three-dimensional spectrum corresponding to the suggested scaling, for scalars at $Sc = 1/8$ and 1 for four different Reynolds numbers. A narrow flat region around $k\eta \approx 0.04$ begins to emerge at $R_\lambda \approx 140$ for scalar with $Sc = 1/8$. At the highest $R_\lambda \approx 390$, a pronounced inertial-convective range of about a decade wide appears beginning from $k\eta \approx 0.008$. For $Sc = 1$ a spectral “bump” following the inertial-convective range can also be observed, which is most pronounced at around $k\eta \approx 0.2$, independent of the Reynolds number. The existence of a spectral bump has not been fully understood. Falkovich (1994) pointed out that viscous suppression of small-scale modes makes non-linear energy transfer less efficient and leads to a pile-up of

energy around the inertial scales. It is possible that a combination of viscous and diffusive effects causes the scalar spectral bump. Reynolds number similarity is also reflected by the “collapse” at high wavenumbers for different R_λ but fixed Sc . On the other hand, a similar collapse occurs at low wavenumbers for different Sc but fixed R_λ . The latter feature is consistent with previous studies of differential diffusion, in which scalars with different molecular diffusivities differ primarily in small scales (Yeung and Pope 1993, Yeung 1996, Saylor and Sreenivasan 1998).

Although it is straightforward to compute the spectrum in Eq. 3.1 as a function of wavenumber magnitude in three-dimensional space, in experiments usually only the one-dimensional version $E_{1\phi}(k)$ is available. However, if isotropy is assumed to hold, there is the spectral relation (Monin and Yaglom 1975)

$$E_\phi(k) = -k \frac{dE_{1\phi}(k)}{dk}. \quad (3.2)$$

This relation implies that C_ϕ^* should be 5/3 of the one-dimensional constant C_ϕ . It follows that the experimental value (Sreenivasan 1996) of $C_\phi \approx 0.4$ corresponds to $C_\phi^* = 0.4(5/3) = 0.67$. Eq. 3.2 can also be used to test the isotropy of the spectrum and it holds well except in the two lowest wavenumber shells, which correspond to the largest scales for which only a limited number of samples exist in the computational domain.

Figure 3.2 shows the one-dimensional compensated spectrum, for scalars with $Sc = 1/8$ and 1 at $R_\lambda \approx 390$. To infer C_ϕ accurately, a linear ordinate is used and a dashed line corresponding to the experimental value in Sreenivasan (1996) is included. Although the range is narrow, there is some evidence for scaling with Obukhov-Corrsin constant close to the dashed line 0.4. The spectral bump for $Sc = 1$ is quite conspicuous. The bump occurs within about the same range of normalized wavenumbers as observed in the higher-Reynolds number grid experiments of Mydlarski and Warhaft (1998) for temperature fluctuations in air with $Sc = 0.7$. Experimental data from Fig. 12 of Mydlarski & Warhaft (1998) is included in figure 2 for comparison. The authors considered the apparent Obukhov-Corrsin constant in their data to be in broad agreement with the estimates by Sreenivasan (1996). In Yeung *et al.* (2002), a similar result is shown at $R_\lambda \approx 240$. The simulation results in

Fig. 3.1 and Fig. 3.2 show that spectral bump occurs at $Sc = 1$ for R_λ between 90 and 390 and it does not seem to depend on Reynolds number, whereas in Mydlarski & Warhaft scalar spectrum at higher Reynolds number show a more distinct bump. Instead, the DNS results show that the scalar spectral bump occurs at Schmidt number close to unity or higher. The Schmidt number effects are weaker, as will be seen in the later part of this section that spectral bump does not occur at relatively low Reynolds number even for high Schmidt numbers. The presence of spectral bump at $Sc = 1$ affects the $-5/3$ scaling range: Without the bump it is likely that one would see a more extensive stretch of the $-5/3$ scaling.

The bump effect is particularly striking in the second-order structure function, which is the spatial equivalent of the one-dimensional spectrum. The classical result for spatial separations in the inertial-convective range is given by

$$D_{\phi\phi}(r) \equiv \langle (\Delta_r \phi)^2 \rangle = C_2 \langle \chi \rangle \langle \epsilon \rangle^{-1/3} r^{2/3}, \quad (3.3)$$

where, as shown in Monin and Yaglom (1975), $C_2 = 1.5\Gamma(1/3)C_\phi \approx 4.02C_\phi$. In this flow configuration, distinction should be made between two-point differences in directions parallel and perpendicular to the mean scalar gradient, as $\Delta_{\parallel}\phi(r)$ and $\Delta_{\perp}\phi(r)$. However, because isotropy at the intermediate scales is implied in Eq. 3.3, it is appropriate to make comparisons using DNS data averaged over r taken in three different coordinate directions.

Figure 3.3 shows the component-averaged structure function $\langle (\Delta_r \phi)^2 \rangle$ normalized by the Obukhov-Corrsin variables as suggested in Eq. 3.3. It can be seen that, as the Reynolds number increases, results for $Sc = 1$ show a tendency towards a flat scaling region. The apparent scaling constant suggested by the data is higher than 1.61 (corresponding to $C_\phi = 0.4$) for $Sc = 1$ and lower for $Sc = 1/8$. In other words, in contrast to the behavior observed in the spectrum, the apparent scaling constant in structure functions shows a significant dependence on Schmidt number. This could be an artifact of the spectral bump which succeeds in masking the limited scaling region in the Fourier-transformed version. In support of this inference, it is noted that this apparent dependence on the Schmidt number weakens with increasing Reynolds number. It is also noted that the scaling region

at $R_\lambda \approx 390$ for $Sc = 1$ stretches over more than one decade with a power law exponent a little less than $2/3$ as suggested in Eq. 3.3. But the scaling trend with Reynolds number implies that as Reynolds number further increases, the scaling in inertial-convective range approaches a power law of $r^{2/3}$. On the other hand, since results at $Sc = 1/8$ behave as power law of $r^{2/3}$, it is possible that the scaling exponents at $Sc = 1$ may be affected by the presence of spectral bump.

The limiting behaviors in Fig. 3.3 for small and large scale separation are both amenable to theoretical analysis, and can therefore be used as checks on the quality of the simulation data. In the limit of small r (i.e. $r \ll \eta_{OC}$), Taylor series arguments yields the result

$$\frac{\langle(\Delta_r \phi)^2\rangle}{\langle\chi\rangle\langle\epsilon\rangle^{-1/3}r^{2/3}} = \frac{1}{6} \left(\frac{r}{\eta_{OC}}\right)^{4/3}, \quad (3.4)$$

which is indicated by a dotted line. Its perfect agreement with the data indicates that the small scales are adequately resolved. For large r , as values of ϕ at two points far apart in space become statistically independent, $\langle(\Delta_r \phi)^2\rangle$ is expected to approach a constant value equal to $2\langle\phi^2\rangle$. The inset shows the ratio $\langle(\Delta_r \phi)^2\rangle/\langle\phi^2\rangle$, which approaches a value close to 2 at large r . The asymptotic behavior at large r implies that the normalized form shown in the main body of Fig. 3.3 should decrease as $r^{-2/3}$. Indeed by using the time-scale ratio $(K/\langle\epsilon\rangle)/\tau_\eta \approx (3/2\sqrt{15})R_\lambda$ the large-separation asymptote can be derived as

$$\frac{\langle(\Delta_r \phi)^2\rangle}{\langle\chi\rangle\langle\epsilon\rangle^{-1/3}r^{2/3}} \approx \frac{3R_\lambda Sc^{1/2}}{\sqrt{15}r_\phi} \left(\frac{r}{\eta_{OC}}\right)^{-2/3}, \quad (3.5)$$

where $r_\phi \equiv (K/\langle\epsilon\rangle)/(\langle\phi^2\rangle/\langle\chi\rangle)$ is the mechanical-to-scalar time scale ratio (See Tables I-III). Because of the periodic boundary conditions used on the computational domain, it is meaningful to compute the structure functions only for r up to half of the length L_0 of each side of the solution domain. However, because of finite domain size (with L_0 only about six times of the integral length scale of the scalar field, which is 40% longer in the direction of the mean scalar gradient), the rate of approach to the large r asymptote is somewhat distorted.

The scaling in inertial-convective range based on the argument of Kolmogorov (1941),

Obukhov (1949) and Corrsin (1951) for any order structure function can be written as

$$\langle (\Delta_r u)^m (\Delta_r \phi)^n \rangle \sim \epsilon^{m/3-n/6} \chi^{n/2} r^{(m+n)/3}, \quad (3.6)$$

where $\Delta_r u$ is the velocity difference over a linear length of r . In particular, the mixed third-order structure function, defined as $D_{L\phi\phi}(r) \equiv \langle \Delta_r u (\Delta_r \phi)^2 \rangle$ where $\Delta_r u$ is a longitudinal velocity increment in space, has a more fundamental role in similarity scaling. An exact result for intermediate r in the inertial-convective range was given by Yaglom (1949) , as

$$\langle \Delta_r u (\Delta_r \phi)^2 \rangle = -(2/3) \langle \chi \rangle r . \quad (3.7)$$

(Note that this relation was originally given by Yaglom with half the present scalar dissipation rate, and so the coefficient here was 4/3 instead of the present 2/3.) In the limit of small r , the velocity and scalar difference can be related to their corresponding gradients as

$$\langle \Delta_r u (\Delta_r \phi)^2 \rangle \approx S_{u\phi} \left\langle \left(\frac{\partial u}{\partial x} \right)^2 \right\rangle^{1/2} \left\langle \left(\frac{\partial \phi}{\partial x} \right)^2 \right\rangle r^3, \quad (3.8)$$

where $S_{u\phi}$ is the mixed gradient skewness defined by (see Kerr 1985)

$$S_{u\phi} \equiv \left\langle \left(\frac{\partial u}{\partial x} \right) \left(\frac{\partial \phi}{\partial x} \right)^2 \right\rangle / \left\langle \left(\frac{\partial u}{\partial x} \right)^2 \right\rangle^{1/2} \left\langle \left(\frac{\partial \phi}{\partial x} \right)^2 \right\rangle . \quad (3.9)$$

Considerations of local isotropy for both velocity and scalar fields lead to the normalized form

$$\frac{\langle \Delta_r u (\Delta_r \phi)^2 \rangle}{\langle \chi \rangle r} \approx \frac{S_{u\phi}}{6\sqrt{15}} \left(\frac{r}{\eta_B} \right)^2 . \quad (3.10)$$

In the large r limit, isotropy of the velocity field implies that $\langle \Delta_r u (\Delta_r \phi)^2 \rangle$ approaches zero.

Figure 3.4 shows DNS results for the mixed structure function, in normalized forms suggested by Eqs. 3.7, where an average is taken over three coordinate components. With $S_{u\phi}$ taken to be of order -0.5 (see Table 3.1), the behavior at small r is indeed seen to follow Eq. 3.10 for all Reynolds and Schmidt numbers in the data. It can be seen that as Reynolds number increases, the scaling range of the mixed structure function becomes wider and the normalized mixed structure function increases toward a plateau of height 2/3 (centered around $r/\eta_B \approx 50$ at R_λ 390 and $Sc = 1$). At larger values of r the curves become more

widely spaced among each other as the range of scales become wider with increasing R_λ and Sc . A rapid drop is seen in the limit as $\langle \Delta_r u (\Delta_r \phi)^2 \rangle$ approaches zero.

The assumptions used to derive Eq. 3.7 are that the scalar field is stationary and isotropic. Yaglom's (1949) transport equation for scalar structure function, which is based on Kármán & Howarth (1938)'s equation for two-point correlations, has the form

$$D_{L\phi\phi}(r) - 2D \frac{dD_{\phi\phi}(r)}{dr} = -\frac{2}{3} \langle \chi \rangle r. \quad (3.11)$$

Eq. 3.7 is thus derived under the assumption that the diffusive term on the left-hand-side of Eq. 3.11 can be neglected in the inertial-convective range. In fact, both the DNS simulations and recent studies by Orlandi and Antonia (2002) for decaying turbulence suggest that the diffusive term is indeed small compared to the other terms in Eq. 3.11 in intermediate scale ranges. In the simulations, nonstationarity contributions vanish when averaged over a sufficiently long period of time. Deviations from Eq. 3.7 and Eq.3.11 must be caused mainly by departures from local isotropy. Significant anisotropy is indeed seen in Fig. 3.5, which shows a comparison between normalized structure functions taken in different coordinate directions for $Sc = 1$ at $R_\lambda \approx 390$. In particular, the structure function is systematically larger for r taken parallel to the mean gradient direction. Since in experiments structure functions are often measured in only one direction, this result suggests caution for inferences on Yaglom's relation.

The scaling behavior of structure functions in inertial-convective range is a major issue in Kolmogorov's (1941) theory. In this work, velocity and scalar structure functions from order 2 up to order 8 at R_λ up to 390 are also obtained. Figure 3.6 shows compensated even-order scalar structure functions normalized based on Eq. 3.6, where average is taken over separation along the three coordinate directions. The compensation power law $r^{\zeta_{m,n}}$ is chosen based on trial and error such that the structure functions show a flat scaling region. The odd-order scalar structure functions should vanish under the assumption of local isotropy in homogeneous turbulence. However, the simulation results in Fig. 3.7 for odd-order scalar structure functions with separation taken in the direction parallel to the mean scalar gradient show an unambiguous scaling range and the scaling exponents are

in sequence with those of even-order structure functions. This is consistent with the fact that odd-order moments of scalar gradient in the direction parallel to the mean gradient have magnitude of order 1 even at very high Reynolds number (Sreenivasan 1991, Warhaft 2000), e.g., the presence of mean scalar gradient causes anisotropy to some extent. Similar findings for the odd-order scalar structure functions have also been reported by Antonia and Van Atta (1978) and Mydlarski and Warhaft (1998).

It is also shown in figure 3.8 and 3.9 the compensated longitudinal velocity structure functions. The deviation of $\zeta_{m,n}$ from the KOC prediction of $n/3$ in Eq. 3.6 for any structure function of order n accounts for the intermittency in inertial or inertial-convective range, except for the third-order longitudinal velocity structure function where the scaling is exact according to the Kolmogorov's four-fifth law

$$\langle(\Delta_r u)^3\rangle = -\frac{4}{5}\langle\epsilon\rangle r, \quad (3.12)$$

with which the DNS simulation result agrees. The scaling power law exponent $\zeta_{m,n}$ for both velocity and scalar structure functions are shown in Fig. 3.10 at the highest $R_\lambda \approx 390$ with $Sc = 1$ for scalar. Fig. 3.10 also includes Mydlarski and Warhaft (1998)'s results for scalar structure functions at $R_\lambda \approx 461$ and $Sc \approx 0.7$ for grid turbulence, Dasi (2004)'s result for scalars in turbulent boundary layer at $Sc \approx 1000$ and results for velocity structure functions at $R_\lambda \approx 536$ for a jet from Anselmet *etal.* (1984). The KOC prediction of $n/3$ is plotted as a dashed line for comparison. Figure 3.10 suggests that scaling behaviors of both velocity and scalar structure functions deviate from KOC theory. But the behavior of scalar field deviates far more than that of velocity field. The power law exponents obtained in the simulations are smaller than those of Mydlarski and Warhaft (1998) and Anselmet *etal.* (1984). Especially for the exponents of scalar structure functions, there is considerable difference between the DNS results and those of Mydlarski & Warhaft, which can be partly explained by the difference of R_λ and Sc . The DNS results for scalars are close to those of Dasi's (2004) for up to the fourth-order, however, Dasi's data for higher order scalar structure functions are well above the DNS results. Figure 3.10 supports the general perception that scalar field is more intermittent than velocity field in inertial-convective

range.

B. Weakly diffusive scalars

For $Sc \gg 1$ Batchelor's result for the scalar spectrum is

$$E_\phi(k) = q \langle \chi \rangle (\nu / \langle \epsilon \rangle)^{1/2} k^{-1} \exp(-q(k\eta_B)^2), \quad (3.13)$$

where the non-dimensional coefficient q was assumed to be universal. Batchelor's theory was based on an assumption of persistent straining of the scalar field by the small scale motions of the characteristic time $\tau_\eta = (\nu / \langle \epsilon \rangle)^{1/2}$. The essential fact underlying Batchelor's analysis is that the strain rate is approximately uniform over the viscous-convective range. Later Kraichnan (1968) proposed a more refined treatment which accounted for fluctuations of the strain rate and arrived at the form

$$E_\phi(k) = q \langle \chi \rangle (\nu / \langle \epsilon \rangle)^{1/2} k^{-1} (1 + (6q)^{1/2} k\eta_B \exp(-(6q)^{1/2} (k\eta_B))) . \quad (3.14)$$

The main difference between the two expressions is in the viscous-diffusive range, $k\eta_B > 1$. In the viscous-convective range $1/\eta \ll k \ll 1/\eta_B$ both expressions give

$$E_\phi(k) = q \langle \chi \rangle (\nu / \langle \epsilon \rangle)^{1/2} k^{-1} \quad (3.15)$$

which is commonly referred to as k^{-1} scaling. A substantial scale separation between η and η_B is required to observe this feature: this requires a high Schmidt number, but not necessarily a high Reynolds number. The value of q is generally estimated by reference to either measurements or closure theories, but without general agreement. For example, Batchelor (1959) took $q = 2$, whereas Qian (1995) suggested $q = 2\sqrt{5}$. The latter was used for comparisons with DNS by Bogucki *et al.* (1997) .

Figure 3.11(a) and (b) show un-normalized scalar spectra for Sc from 1/4 to 64 at $R_\lambda \approx 38$ and Sc from 64 to 1024 at $R_\lambda \approx 8$, respectively. As Sc increases, weaker molecular diffusivity reduces the length scales at which scalar dissipation occurs and more scalar fluctuations arise at high wavenumbers. At both R_λ , a clear k^{-1} scaling range appears and becomes well-defined with increasing Sc . The spectrum progressively spreads out toward wavenumbers higher than $1/\eta$ with increasing Sc . At low wavenumbers, the spectrum is

almost independent of Sc , which confirms the Reynolds number similarity at large scales, similar as in Fig. 3.1. The spectra for $Sc = 256$ computed from 256^3 and 512^3 simulations in Fig. 3.11(b) appear to virtually coincide, which suggests $k_{max}\eta_B = 1.5$ gives sufficient resolution, at least for second-order statistics.

In order to compare the scaling behavior at high Sc with the KOC scaling, it is shown in Fig. 3.12(a) and (b) the scalar spectrum normalized by KOC variables. Instead of a flat region indicating KOC's $k^{-5/3}$ law, a scaling range with slope $2/3$ appears suggesting a power law behavior of k^{-1} . It is noticed in Fig. 3.12(a) at $R_\lambda \approx 38$, the scaling range lies at scales larger than η ; in Fig. 3.12(b) at $R_\lambda \approx 8$ for higher Schmidt numbers, the k^{-1} range shifts toward scales smaller than η .

Figure 3.13(a) and (b) show the DNS data at $R_\lambda \approx 38$ and $R_\lambda \approx 8$ for the spectrum normalized by Batchelor variables (as a function of $k\eta_B$) and compared with the expressions of Batchelor and Kraichnan, where $q = 2\sqrt{5}$ is used according to Qian (1995). The data suggest the presence of k^{-1} scaling for $k\eta_B < 0.1$. Kraichnan's form is more accurate in the viscous-diffusive range, within which good agreement is found even for $Sc = 1$. To infer the value of q needed for the best fit, the log-linear scale plot is also shown in the inset for the quantity $kE_\phi(k)(\langle\epsilon\rangle/\nu)^{1/2}/\langle\chi\rangle$ versus $k\eta_B$, such that q would be the height of a plateau at $k\eta_B \ll 1$. It appears that the value of q required for an optimum fit increases with Sc somewhat, being about 3.5 for $Sc = 1$ but 5.5 for $Sc = 64$ at $R_\lambda \approx 38$. At $R_\lambda \approx 8$, the optimum fit for q varies from 4.3 for $Sc = 64$ to 5.2 for $Sc = 1024$.

Although classical arguments suggest that the width of an apparent k^{-1} scaling range is primarily contingent upon having a sufficiently high Schmidt number, it is of interest to ascertain whether there is also a Reynolds number dependence. To address this question, Fig. 3.14 compares the normalized spectra for three Reynolds and Schmidt number combinations. An increase of Sc from 64 to 1024 with R_λ held constant (at 8) produces, as expected, results closer to k^{-1} scaling with a wider range. However, a similar effect can also be observed when R_λ is increased (from 8 to 38) while Sc is held constant (at 64). These results suggest that the actual requirement for high Sc may be weakened (say, towards only

moderately large values) if the Reynolds number is high. The difference between the scalar spectrum at $R_\lambda \approx 38$, $Sc = 64$ and $R_\lambda \approx 8$, $Sc = 1024$ is that the k^{-1} scaling range lies more in the viscous-convective range between η_B and η for scalar of higher Schmidt number, whereas for scalar at higher Reynolds number with relatively low Schmidt number, the Batchelor scaling range shifts toward larger scales than those in the viscous-convective range.

The effects of Schmidt number on the scaling of second-order structure function for $Sc > 1$ are shown in Fig. 3.15(a) and (b). For small r the Taylor-series result (Eq. 3.4) in terms of Obukhov-Corrsin variables is seen to continue to hold, even for $Sc \gg 1$. Whereas an increase in Reynolds number has been seen (Fig. 3.3) to promote a plateau in the normalized structure function, an increase of Schmidt number apparently has no such effect. In the limit of large r the data conforms to Eq. 3.5 which is valid at all Schmidt numbers. Since the scaling used in Fig. 3.15 is chosen to produce a universal “collapse” at the small scales, the “fanning-out” of curves with increasing Schmidt number also reflects the existence of a wider range of scales in the scalar field at higher Sc . It is noted that the second-order structure function for $Sc = 256$ from the 256^3 and 512^3 simulations almost coincides, similar as in Fig. 3.12(b).

Corresponding results for the mixed third-order structure function for high Schmidt numbers at $R_\lambda \approx 38$ and $R_\lambda \approx 8$ are shown in Fig. 3.16(a) and (b). It is interesting to note that, although Yaglom’s relation (Eq. 3.7) is traditionally associated with the inertial-convective range for $Sc \leq 1$ at high Reynolds number, the arguments leading to it are also increasingly valid at high Sc . Indeed it can be seen that the results at high Sc appear to approach the limit of Yaglom’s relation for intermediate r .

3.2 Local Isotropy: Schmidt number effects

Local isotropy is the central assumption in KOC scaling. In the limit of infinite Reynolds number and Schmidt number, scalar and velocity fields are assumed to be isotropic at small scales. Many indicators of varying degrees of sensitivity can be used as tests of local isotropy.

For example in Sec. 3.1, isotropy relations between spectra in one and three dimensions have been discussed, and it is noted that structure functions show some differences depending on the direction of the spatial separation. Here, the focus is mainly on statistics of scalar gradients parallel ($\nabla_{\parallel}\phi$) and perpendicular ($\nabla_{\perp}\phi$) to the mean gradient, including their relationships with velocity gradient fluctuations.

Because of reflectional symmetry in the plane perpendicular to the mean gradient, all odd-order moments of $\nabla_{\perp}\phi$ are expected to be zero. Furthermore, local isotropy requires odd-order moments of $\nabla_{\parallel}\phi$ to vanish, and even-order moments of $\nabla_{\parallel}\phi$ and $\nabla_{\perp}\phi$ to be equal. Table 3.3-3.5 show that the second-order moment of $\nabla_{\parallel}\phi$ and $\nabla_{\perp}\phi$ are very close to each other and without definite trend with Reynolds number or Schmidt number, suggesting that the second-order moment of scalar gradient is not a sensitive indicator of local isotropy. Figures 3.17(a), (b) and (c) show higher-order moments of scalar gradients as a function of Schmidt number at $R_{\lambda} \approx 38$ with Sc varying from 1/4 to 64 and $R_{\lambda} \approx 8$ with Sc from 1 to 1024 (also listed in Tables 3.3 and 3.5). The skewness of $\nabla_{\parallel}\phi$ in Fig. 3.17(a) slightly increases at low Sc at both R_{λ} , then for $Sc \geq 1$ at $R_{\lambda} \approx 38$ and $Sc \geq 8$ at $R_{\lambda} \approx 8$, the skewness decreases steadily as an approximate power law of Sc . A weaker trend of decrease at high Peclet number may also be present in results by Holzer and Siggia (1994) based on two-dimensional synthetic velocity fields. Between $Sc = 4$ and 64, the skewness at $R_{\lambda} \approx 38$ and $R_{\lambda} \approx 8$ is close to each other, although it has a slightly faster decreasing rate at $R_{\lambda} \approx 38$. In Fig. 3.17(a), the skewness factors from Mydlarski and Warhaft (1998), Tong and Warhaft (1994) for grid turbulence at $Pr = 0.71$ for R_{λ} up to over 700 are also included for comparison and they are reasonably close to the DNS results. From Tables 3.3-3.5, it can be seen that the value of skewness of $\nabla_{\parallel}\phi$ for $Sc \leq 1$ at all Reynolds numbers is typically between 1 and 2 with the smallest value (~ 0.3) occurring at the highest Schmidt number ($Sc=1024$). This apparent trend of decreasing skewness at high Schmidt number is, however, just one facet of the deeper question of whether local isotropy would be recovered in the limit of infinite Schmidt number. In any case, the results suggest that local isotropy is a better approximation at high Schmidt number. This positive skewness itself is usually thought to be due to the occurrence of ramp-cliff structures of preferred orientation induced

by the mean gradient, e.g., Antonia and Van Atta (1978). If so, a reduction of skewness may be the result of the orientation of these structures in space becoming more randomized. The effects of high Schmidt number on these structures have not yet been investigated in detail though a beginning has been made in Schumacher (2003).

It is emphasized that the observed values of the skewness of $\nabla_{\parallel}\phi$ as shown in Tables 3.3-3.5 do not decrease with increasing Reynolds number, which is consistent with various results at high Reynolds number in the literature (Warhaft 2000). On the other hand, the flatness factors show increasing closeness between $\nabla_{\parallel}\phi$ and $\nabla_{\perp}\phi$ at high Schmidt numbers. It is also noted that the flatness of $\nabla_{\parallel}\phi$ and $\nabla_{\perp}\phi$ monotonically increases with Reynolds number. For a more complete picture, higher-order moments are also studied. Normalized third, fifth and seventh moments (μ_3, μ_5, μ_7) of $\nabla_{\parallel}\phi$, shown in Fig. 3.17(c), seem to decrease with Sc . (The situation for moments of yet higher orders is unclear because they are subject to large uncertainties in statistical sampling.) The rates of decrease depend on the order of the moment. It is clear that, if the seventh order moment is to ultimately reach the isotropic value of zero, the Schmidt number would have to be extremely high. It is noticed that at small Sc the odd-order moments of $\nabla_{\parallel}\phi$ are larger for higher Reynolds number, but as Sc increases, the odd-order moments decrease faster at higher Reynolds number, which suggests that better approximation of local isotropy can be achieved in the limit of both high Sc and Re .

A positive skewness for $\nabla_{\parallel}\phi$ as seen in Fig. 3.17(a) and 3.17(c) means that large positive fluctuations are more likely than negative ones. The probability density function (PDF) of $\nabla_{\parallel}\phi$ in normalized form is shown in Fig. 3.18(a) and (b) at $R_{\lambda} \approx 38$ and $R_{\lambda} \approx 8$ for various Schmidt numbers. The PDF becomes more nearly symmetric at higher Sc , which is consistent with the reduction in skewness noted above. Schmidt number effects appear to be primarily felt via increased probabilities for large negative fluctuations. The increasing “width” of the PDF at high Schmidt number also indicates increased non-Gaussianity and intermittency. Comparison of Fig. 3.18(a) and Fig. 3.18(b) shows that the PDF of scalar gradient is “wider” at higher Reynolds number, which suggests increased intermittency with Reynolds number and is consistent with the flatness of $\nabla_{\parallel}\phi$ shown in Tables 3.3-3.5. The

form of the PDF is apparently close to exponential in the range between 5 to 15 standard deviations. However, because of sampling limitations, the behavior at the extreme tails is somewhat uncertain.

Statistical relationships between velocity gradient and scalar gradient fluctuations expressed as “mixed” derivative moments are also relevant tests of isotropy. Similar to the mixed gradient skewness $S_{u\phi}$ (Eq. 3.9), the mixed gradient flatness is defined by

$$F_{u\phi} \equiv \left\langle \left(\frac{\partial u}{\partial x} \right)^2 \left(\frac{\partial \phi}{\partial x} \right)^2 \right\rangle / \left\langle \left(\frac{\partial u}{\partial x} \right)^2 \right\rangle \left\langle \left(\frac{\partial \phi}{\partial x} \right)^2 \right\rangle . \quad (3.16)$$

Similar quantities $S_{v\phi}$, $S_{w\phi}$ and $F_{v\phi}$, $F_{w\phi}$ defined in the other (y and z) coordinate directions are also calculated. Numerical values of $S_{u\phi}$ and $F_{u\phi}$ listed in Tables 3.1 and 3.2 show that the mixed skewness and flatness are generally larger in the direction of the mean scalar gradient. The contrast among different coordinate directions is strongest for low Schmidt number, but becomes less so at higher Reynolds number and/or Schmidt number. If gradients of velocity and scalar were statistically independent, the mixed skewness would be zero, and the mixed flatness would be unity. However, the data do not show a clear trend towards these asymptotic states.

In addition to single-point statistics presented above, it is useful to consider the degree of local isotropy as a function of scale size. In Fig. 3.19(a) and (b), it is shown that the skewness structure function

$$\mu_3(r) \equiv \frac{\langle [\Delta_{\parallel} \phi(r)]^3 \rangle}{\langle [\Delta_{\parallel} \phi(r)]^2 \rangle^{3/2}} . \quad (3.17)$$

This is the skewness of the increment $\Delta_{\parallel} \phi(r)$. Similar to measurements in grid turbulence with transverse temperature gradient (Mydlarski and Warhaft 1998), this function is found to be non-negative for all scale sizes r . Furthermore, contrary to local isotropy, this skewness becomes larger as r becomes smaller. At r of order η_B or less, different curves are seen to approach plateaus of different heights, corresponding to the skewness of $\nabla_{\parallel} \phi$ (see Tables 3.3-3.5). All curves approach zero for large r , because $\Delta_{\parallel} \phi(r)$ would then become a difference between two independent random variables. For high Sc (e.g., curve H for $Sc = 64$ and curve I for $Sc = 1024$), there is some hint of an intermediate scaling range at the highest Sc for both cases, where the skewness becomes nearly independent of r . This observation

suggests the emergence of a viscous-convective range, where a small deviation from local isotropy exists at the level of the third-order moment.

3.3 Intermittency: effects for high Schmidt numbers

The small-scale intermittency of the passive scalar field is usually expressed in terms of the statistical properties and spatial structure of scalar gradients and the dissipation rate. The prime concern in this chapter is how the small-scale intermittency depend on the Schmidt number, with observations of Reynolds number dependence also providing a useful contrast. In Chapter 4, intermittency as a function of scale size is discussed through two-point statistics of dissipation.

Tables 3.3-3.5 also present several moments of the scalar dissipation rate, and of its logarithm. Because χ is a non-negative random variable, both its skewness and flatness factors are indicators of the occurrence of intense fluctuations that are large compared to the mean value. In addition, the ratio $\sigma_\chi/\langle\chi\rangle$ (where σ_χ is the standard deviation) as well as the variance of $\ln\chi$ provide information on intermittency characteristics (Monin and Yaglom 1975, Frish 1995). From Tables 3.3-3.5 it is clear that, for a fixed Schmidt number, intermittency increases with Reynolds number.

To interpret Schmidt number effects it is noted first that, for the same Reynolds number and Schmidt number, all measures of intermittency from simulations at higher grid resolutions are consistently stronger than those at lower resolutions. Such cases include $Sc = 16$ at $R_\lambda \approx 38$, $Sc = 64$ and $Sc = 256$ at $R_\lambda \approx 8$, which suggest that intermittency may be underestimated if the grid resolution is not sufficiently refined. In other words, it is likely that the intermittency at $Sc = 64$, $R_\lambda \approx 38$ and $Sc = 1024$, $R_\lambda \approx 8$ (as well as at $Sc = 1$ for $R_\lambda = 140, 240$ and 390) is somewhat stronger than suggested in Tables 3.3-3.5. The flatness of the scalar dissipation, which is highly intermittent, is also subject to substantial statistical uncertainty. However, it is worth noting that, although the ensemble-averaged moments individually depend on Sc , a scatter plot of the flatness versus skewness (with one data point for each realization) from all realizations at all Reynolds

number ($R_\lambda \approx 8, 38, 140, 240, 390$) and all Schmidt numbers (Sc from $1/8$ to 1024), as shown in Fig. 3.22, is essentially universal independent of Sc and R_λ . In other words, despite the substantial variability expected for higher-order moments, all realizations obey a systematic trend, which in Fig. 3.22 is represented as a power-law variation with an exponent of 2.33 by least-square fit. It is interesting to note that all realizations at different Reynolds numbers and Schmidt numbers have similar scaling behavior, although some deviations appear for $R_\lambda \approx 8$ and $R_\lambda \approx 390$. In Yeung *et al.* (2002), results at the same $R_\lambda \approx 38$ appear to have better power law scaling.

Some general conclusions on Schmidt number dependence can be drawn. It has been seen in Tables 3.3-3.5 and Fig. 3.17(b) that the flatness factor of scalar gradients increases with Sc for low values of Sc , but varies little at higher Sc . Overall, it can be said that, consistent with other works in the literature (Bogucki *et al.* 1997, Vedula *et al.* 2001), all measures of intermittency for scalar dissipation at $Sc = 1$ are more pronounced than those for energy dissipation. In addition, it seems clear that the flatness of scalar gradient stops increasing for Sc greater than ~ 10 . This saturation of the flatness data suggests that some asymptotic state is reached as $Sc \rightarrow \infty$. Data on the skewness of $\ln \chi$ indicate that χ is more symmetric or closer to lognormal at higher Reynolds numbers: $\mu_3(\ln \chi)$ remains between -0.2 to -0.5 at $R_\lambda \approx 8$ and 38 , whereas its magnitude is less than 0.1 at higher Reynolds number cases. Theories (Chertkov *et al.* 1998) based on rapidly varying Gaussian velocity fields suggest that χ has a stretched-exponential PDF in the limit of very high Schmidt number.

Finally, before a more detailed discussion on intermittency in inertial-convective range and viscous-convective range in the next chapter, let us consider intermittency as a function of scale size in terms of scalar structure functions for the quantities $\Delta_{\parallel} \phi(r)$ and $\Delta_{\perp} \phi(r)$ with separation distance taken in the parallel and perpendicular directions, respectively, as shown in Fig. 3.20 and 3.21 for $R_\lambda \approx 38$ and $R_\lambda \approx 8$ respectively. It can be seen that although, for $Sc > 4$ at $R_\lambda \approx 38$ and higher Sc at $R_\lambda \approx 8$, the increasing trend ceases to hold for small scales, it does persist for intermediate scale sizes. This is especially true in the parallel direction. At $R_\lambda \approx 8$, the flatness structure function curves are closer at high

Sc indicating closer approximation of high Sc limit. At lower Schmidt numbers $\Delta_{\parallel}\phi(r)$ is more intermittent than $\Delta_{\perp}\phi(r)$, but this difference (which is an indication of anisotropy at scale size r) appears to vanish in the $Sc \gg 1$ limit.

In this Chapter, discussions have been given for the DNS results on scalar spectrum and structure functions at Reynolds numbers that are high enough to have inertial-convective range. The DNS data support the KOC $-5/3$ scaling in inertial-convective range. The scalar spectrum at high Schmidt numbers appears to have a Batchelor k^{-1} scaling range. Discussions on the issues of local isotropy and small-scale intermittency at high Schmidt numbers are also given through statistics of scalar gradient and scalar dissipation. Local isotropy appears to be a better approximation at high Schmidt numbers and small-scale intermittency tends to approach an asymptotic level in the high Schmidt limit.

Table 3.1: Mixed gradient skewness and flatness at R_λ up to 390.

N	256	256	256	256	512	512	512	256	256	512	512	1024	1024
R_λ	38	38	38	38	38	38	38	140	140	240	240	390	390
Sc	1	4	8	16	16	32	64	1/8	1	1/8	1	1/8	1
$S_{u\phi}$	-0.7	-0.6	-0.6	-0.6	-0.6	-0.5	-0.5	-0.6	-0.6	-0.6	-0.6	-0.6	-0.5
$S_{v\phi}$	-0.4	-0.5	-0.5	-0.5	-0.5	-0.5	-0.5	-0.4	-0.4	-0.4	-0.5	-0.5	-0.5
$S_{w\phi}$	-0.4	-0.5	-0.5	-0.5	-0.5	-0.5	-0.4	-0.4	-0.5	-0.5	-0.5	-0.5	-0.5
$F_{u\phi}$	2.1	2.0	1.9	1.9	1.9	1.9	1.8	2.0	2.0	2.3	2.2	2.3	2.3
$F_{v\phi}$	1.7	1.8	1.8	1.7	1.8	1.7	1.7	1.7	1.8	2.0	2.0	2.2	2.3
$F_{w\phi}$	1.7	1.7	1.7	1.7	1.7	1.7	1.7	1.8	1.8	2.0	2.0	2.2	2.2

Table 3.2: Mixed gradient skewness and flatness at $R_\lambda \approx 8$.

N	128	128	128	128	128	128	256	256	256	512	512	512
R_λ	8	8	8	8	8	8	8	8	8	8	8	8
Sc	1	4	8	16	32	64	64	128	256	256	512	1024
$S_{u\phi}$	-0.6	-0.5	-0.5	-0.5	-0.5	-0.5	-0.5	-0.5	-0.5	-0.5	-0.5	-0.5
$S_{v\phi}$	-0.3	-0.4	-0.5	-0.5	-0.5	-0.5	-0.5	-0.5	-0.5	-0.5	-0.5	-0.5
$S_{w\phi}$	-0.3	-0.4	-0.5	-0.5	-0.5	-0.5	-0.5	-0.5	-0.5	-0.5	-0.5	-0.5
$F_{u\phi}$	1.9	1.7	1.6	1.6	1.6	1.5	1.5	1.5	1.5	1.5	1.5	1.5
$F_{v\phi}$	1.3	1.4	1.4	1.5	1.5	1.5	1.4	1.4	1.4	1.4	1.5	1.5
$F_{w\phi}$	1.3	1.4	1.5	1.5	1.5	1.5	1.4	1.4	1.4	1.5	1.5	1.5

Table 3.3: Statistical moments of scalar gradients and the scalar dissipation at $R_\lambda \approx 38$.

N	256	256	256	256	512	512	512
R_λ	38	38	38	38	38	38	38
Sc	1	4	8	16	16	32	64
$\frac{\text{Var}(\nabla_{\parallel}\phi)}{\text{Var}(\nabla_{\perp}\phi)}$	1.1	1.1	1.1	1.1	1.0	1.0	1.0
$\mu_3(\nabla_{\parallel}\phi)$	1.7	1.5	1.3	1.0	1.0	0.8	0.5
$\mu_3(\nabla_{\perp}\phi)$	-0.1	-0.1	0.	0.	0.	0.	0.
$\mu_4(\nabla_{\parallel}\phi)$	12	13	13	13	14	14	13
$\mu_4(\nabla_{\perp}\phi)$	9	11	11	11	12	12	12
$\mu_3(\chi)$	6	7	7	7	8	8	8
$\mu_4(\chi)$	61	91	95	81	121	120	101
$\text{Var}(\ln \chi)$	2.6	3.4	3.7	3.5	3.9	4.1	3.8
$\mu_3(\ln \chi)$	-0.1	-0.2	-0.2	-0.2	-0.3	-0.3	-0.2
$\mu_4(\ln \chi)$	2.9	2.8	2.9	2.8	2.9	2.9	2.8

Table 3.4: Statistical moments of scalar gradients and the scalar dissipation at R_λ up to 390.

N	256	256	512	512	1024	1024
R_λ	140	140	240	240	390	390
Sc	1/8	1	1/8	1	1/8	1
$\frac{\text{Var}(\nabla_{\parallel}\phi)}{\text{Var}(\nabla_{\perp}\phi)}$	1.0	1.1	1.1	1.1	1.0	1.0
$\mu_3(\nabla_{\parallel}\phi)$	1.72	1.5	2.1	1.6	2.1	1.4
$\mu_3(\nabla_{\perp}\phi)$	-0.1	-0.1	0.	0.	0.	0.
$\mu_4(\nabla_{\parallel}\phi)$	12	15	19	21	25	28
$\mu_4(\nabla_{\perp}\phi)$	10	13	15	18	22	25
$\mu_3(\chi)$	7	8	10	11	13	35
$\mu_4(\chi)$	78	103	192	204	372	–
$\text{Var}(\ln \chi)$	2.9	3.3	3.2	3.6	3.9	4.0
$\mu_3(\ln \chi)$	-0.1	-0.1	0.	0.	0.	0.1
$\mu_4(\ln \chi)$	2.9	2.8	2.9	2.9	2.8	2.8

Table 3.5: Statistical moments of scalar gradients and the scalar dissipation at $R_\lambda \approx 8$.

N	128	128	128	128	128	128	256	256	256	512	512	512
R_λ	8	8	8	8	8	8	8	8	8	8	8	8
Sc	1	4	8	16	32	64	64	128	256	256	512	1024
$\frac{\text{Var}(\nabla_{\parallel}\phi)}{\text{Var}(\nabla_{\perp}\phi)}$	0.8	0.9	1.0	1.0	1.0	1.0	1.0	1.0	1.0	1.1	1.1	1.1
$\mu_3(\nabla_{\parallel}\phi)$	1.0	1.2	1.2	1.1	0.9	0.7	0.7	0.6	0.4	0.5	0.4	0.3
$\mu_3(\nabla_{\perp}\phi)$	-0.1	-0.1	0.	-0.1	-0.1	0.	0.1	0.1	0.1	-0.1	0.	0.
$\mu_4(\nabla_{\parallel}\phi)$	5.3	7.5	8.5	9.2	9.4	9.1	9.4	9.7	9.5	11	10	10
$\mu_4(\nabla_{\perp}\phi)$	4.4	6.0	6.7	7.4	8.0	8.1	8.8	9.0	8.8	10	10	10
$\mu_3(\chi)$	3.3	4.2	4.6	4.9	5.3	5.3	6.2	6.2	5.8	6.3	6.4	6.3
$\mu_4(\chi)$	18	30	36	44	51	53	73	73	64	76	82	78
$\text{Var}(\ln \chi)$	1.5	2.1	2.4	2.7	3.0	3.0	3.2	3.4	3.3	3.7	3.9	3.7
$\mu_3(\ln \chi)$	-0.4	-0.3	-0.3	-0.3	-0.3	-0.3	-0.4	-0.4	-0.3	-0.5	-0.5	-0.4
$\mu_4(\ln \chi)$	3.4	3.0	2.9	2.9	2.9	2.9	3.0	3.0	2.9	3.1	3.1	2.9

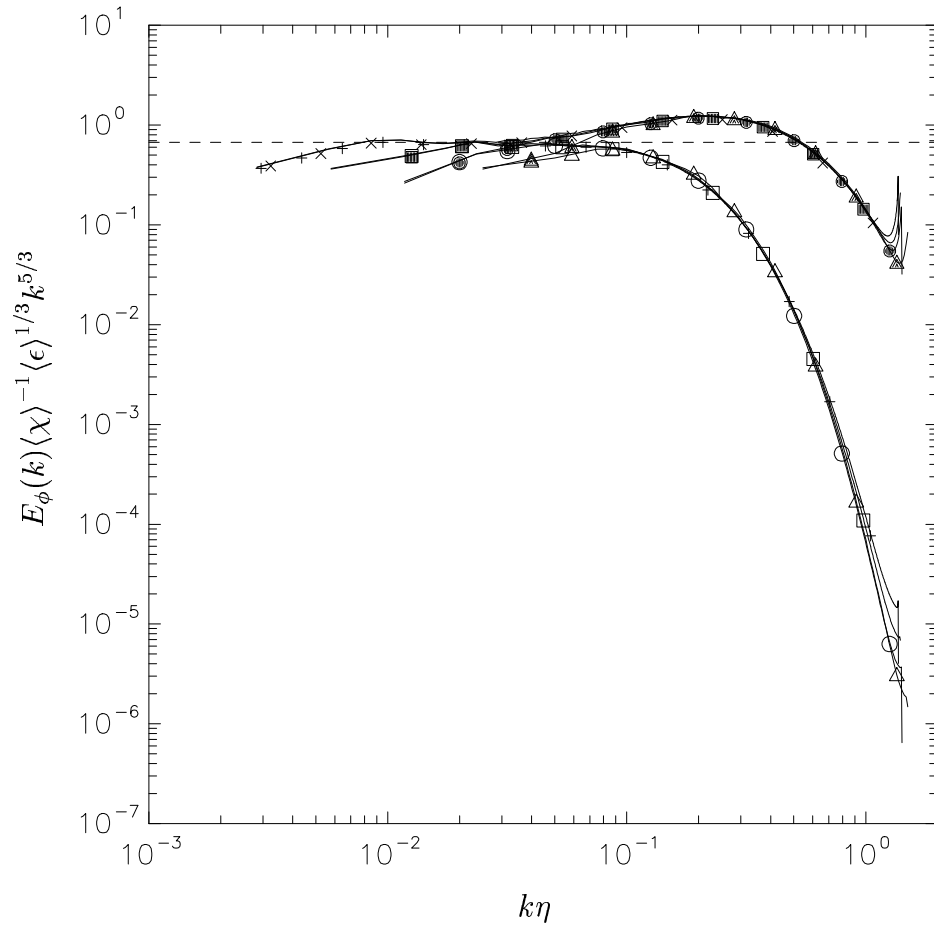


FIG. 3.1. Compensated spectrum according to Obukhov-Corrsin variables (Eq. 3.1) for passive scalars at different Schmidt numbers (open symbols for 1/8, closed symbols for 1.0). Triangles, circles and squares denote Reynolds number at 90, 140 and 240 respectively. Cross and plus denote $Sc = 1$ and 1/8, respectively, at $R_\lambda \approx 390$. Dashed line at 0.67 is for comparison with experiments.

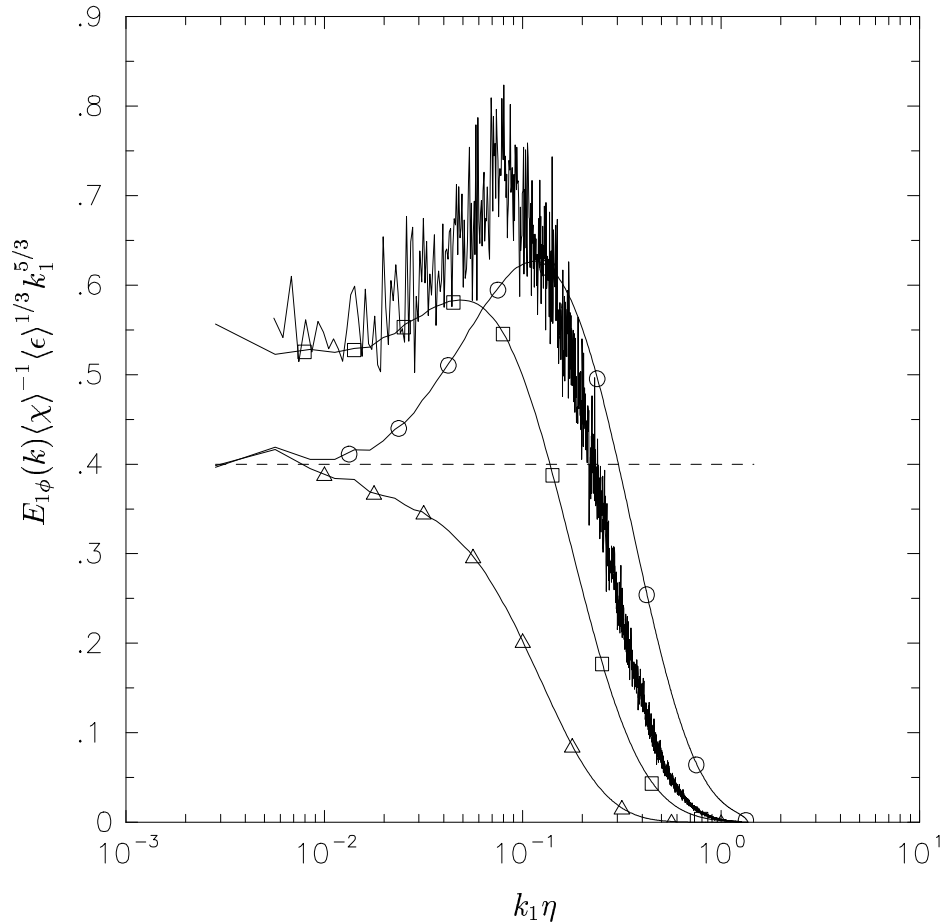


FIG. 3.2. Compensated one-dimensional spectrum for scalars of $Sc = 1/8$ (triangles) and $Sc = 1$ (circles) at $R_\lambda \approx 390$. Dashed line at 0.4 is for comparison with experiments (Sreenivasan 1996). Also shown for comparison are: Squares for one-dimensional longitudinal energy spectrum in DNS, and unmarked solid line for data on scalar spectrum from Mydlarski & Warhaft (1998) at $R_\lambda \approx 582$ and Prandtl number of 0.71.

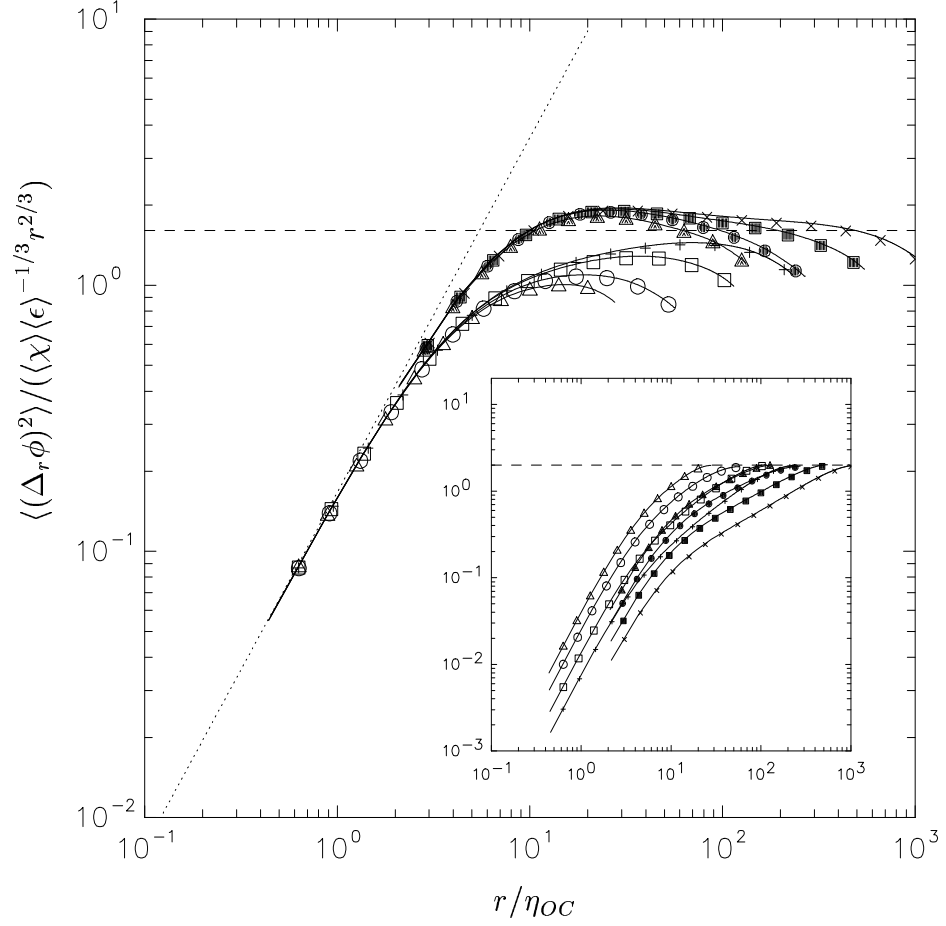


FIG. 3.3. Obukhov-Corrsin scaling of component-averaged second-order structure function of passive scalars at different Schmidt numbers (open symbols for 1/8, closed symbols for 1.0). Triangles, circles and squares denote Reynolds number at 90, 140 and 240 respectively. Cross and plus denote $Sc = 1$ and 1/8, respectively, at $R_\lambda \approx 390$. The dotted line shows the small r asymptote (Eq. 3.4). Dashed line at 1.608 is for comparison with experiments. The inset shows second-order structure function normalized by the scalar variance (which is not dependent on r), with dashed line at the value 2.0.

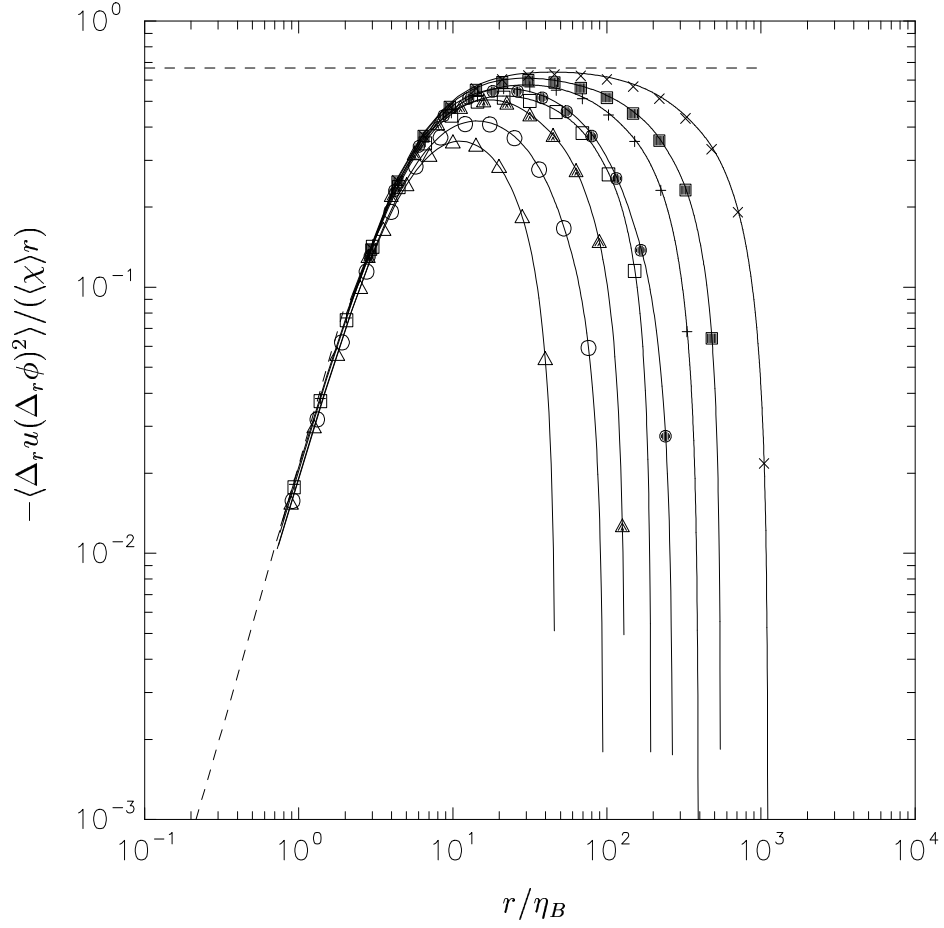


FIG. 3.4. Scaling of mixed third-order velocity-scalar structure function, compared with Yaglom's relation (Eq. 3.7). Symbols are same as in Fig. 3.3. Dashed line at $2/3$ is for comparison with Yaglom's exact result.

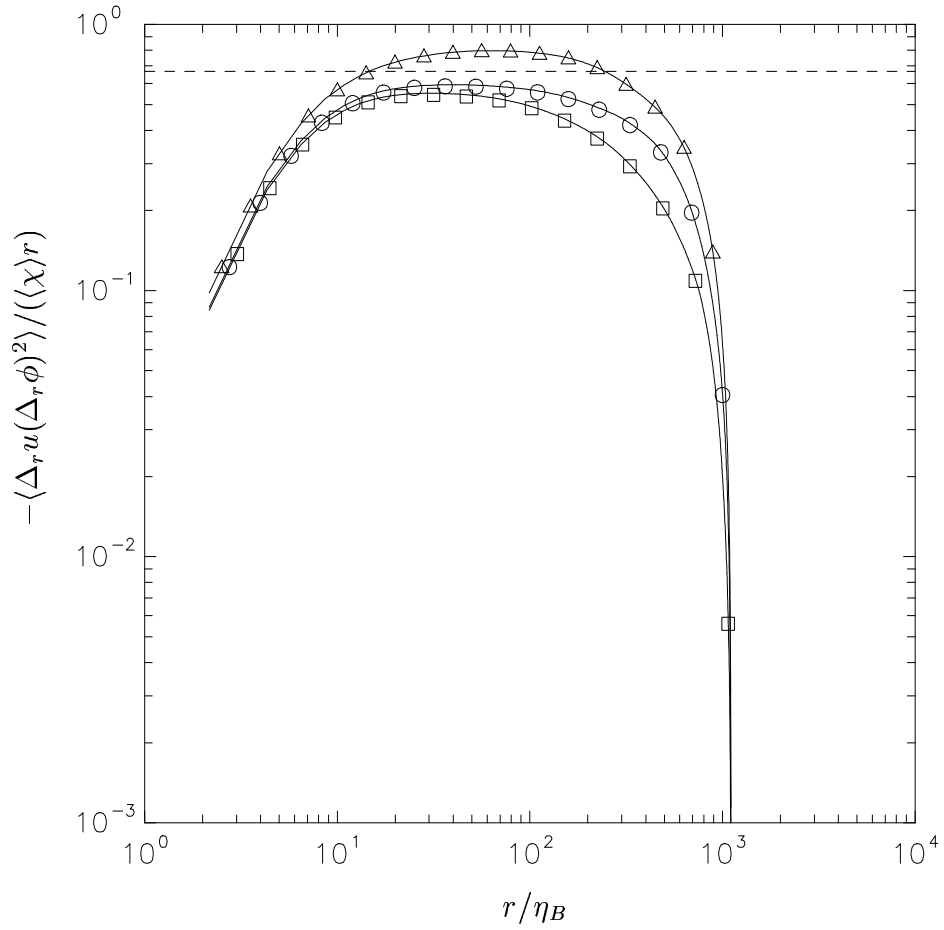


FIG. 3.5. Normalized third-order velocity-scalar structure function for $Sc = 1$ at $R_\lambda \approx 390$, with separation distance r taken in different coordinate directions (triangles, circles and squares for x , y , z , respectively).

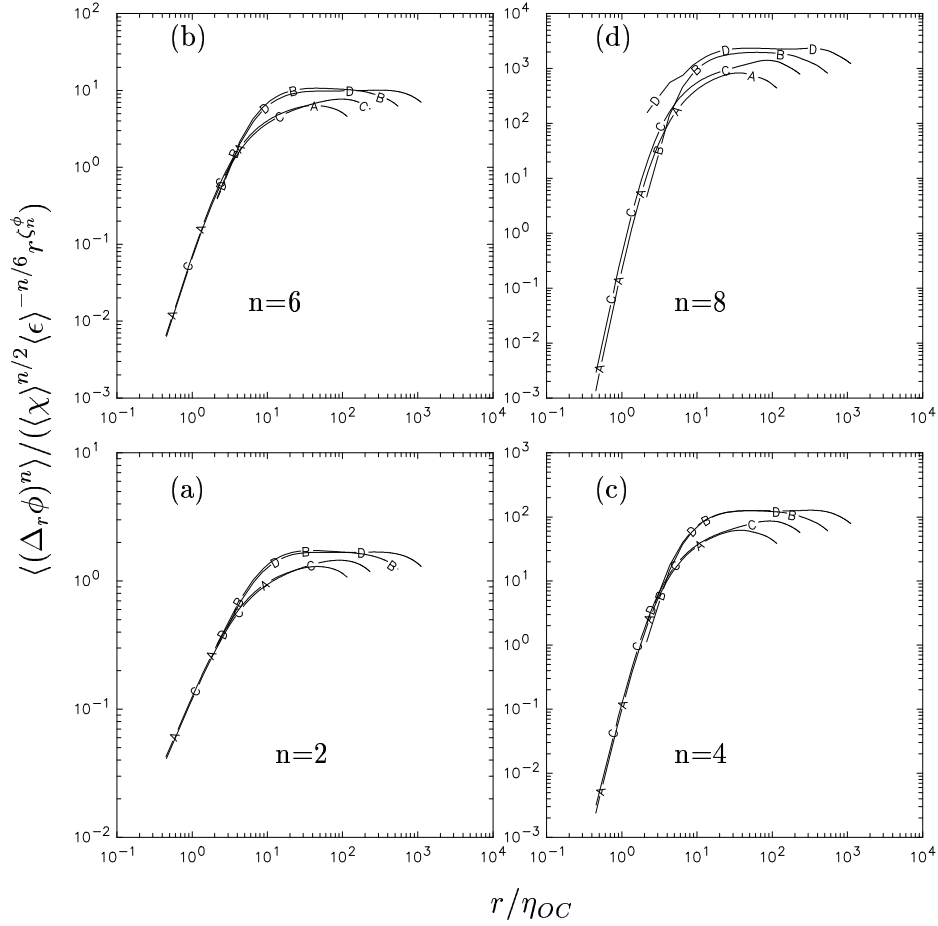


FIG. 3.6. Even-order compensated scalar structure functions. Curves *A* and *B* are at $R_\lambda \approx 240$ for $Sc = 1/8$ and $Sc = 1$, respectively. Curves *C* and *D* are at $R_\lambda \approx 390$ for $Sc = 1/8$ and $Sc = 1$, respectively. Compensation power law exponents for $Sc = 1$ at $R_\lambda \approx 390$ are $\zeta_2^\phi = 0.6$, $\zeta_4^\phi = 0.85$, $\zeta_6^\phi = 1.0$ and $\zeta_8^\phi = 1.1$.

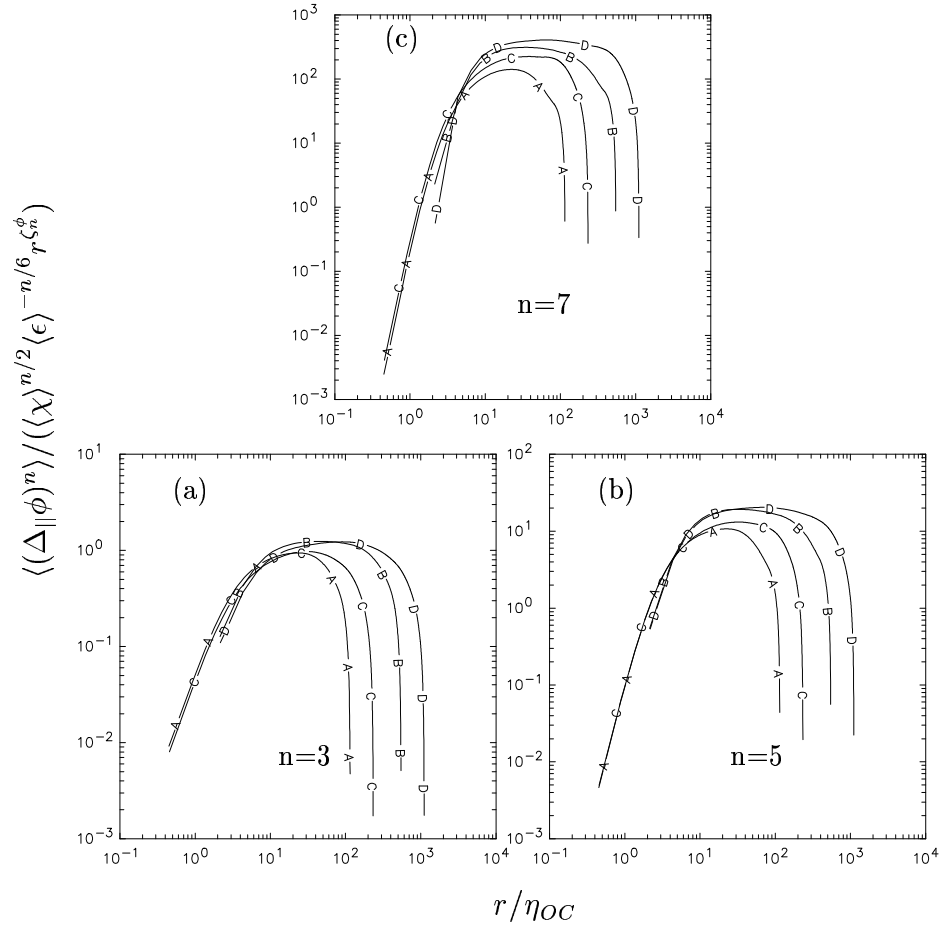


FIG. 3.7. Odd-order compensated scalar structure functions, where the notations for each curve are the same as FIG. 3.6. $\zeta_3^\phi = 0.75$, $\zeta_5^\phi = 0.95$, and $\zeta_7^\phi = 1.05$ for $Sc = 1$ at $R_\lambda \approx 390$.

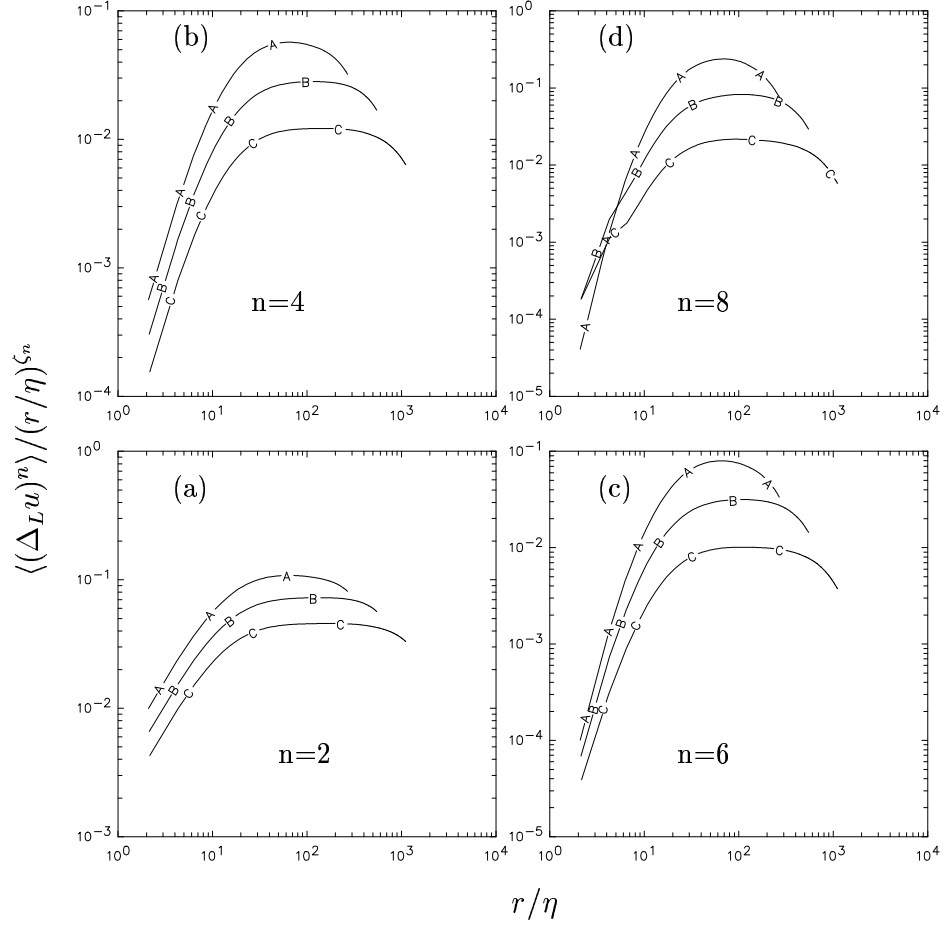


FIG. 3.8. Even-order compensated longitudinal velocity structure functions. Curves A , B and C are at $R_\lambda \approx 140$, $R_\lambda \approx 240$ and $R_\lambda \approx 390$, respectively. Compensation power law exponents at $R_\lambda \approx 390$ are $\zeta_2 = 0.68$, $\zeta_4 = 1.26$, $\zeta_6 = 1.75$ and $\zeta_8 = 2.15$.

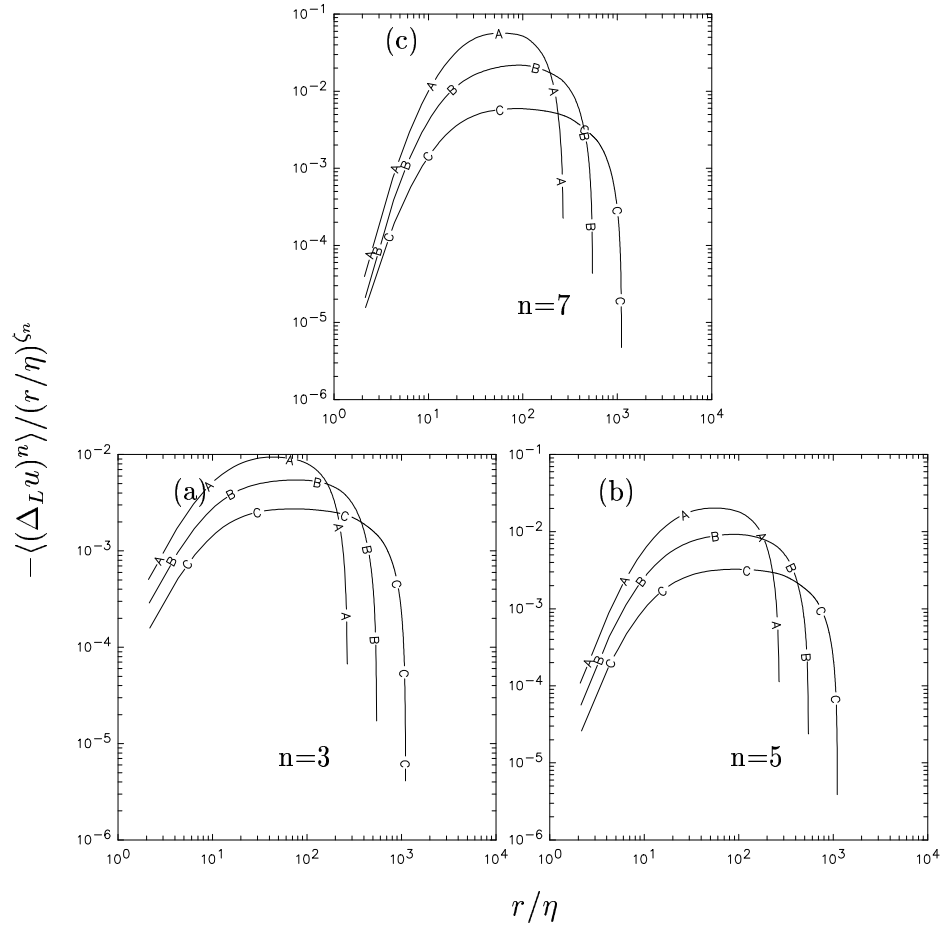


FIG. 3.9. Same as FIG. 3.8 for odd-order structure functions. $\zeta_3 = 1$, $\zeta_5 = 1.5$, and $\zeta_7 = 1.96$.

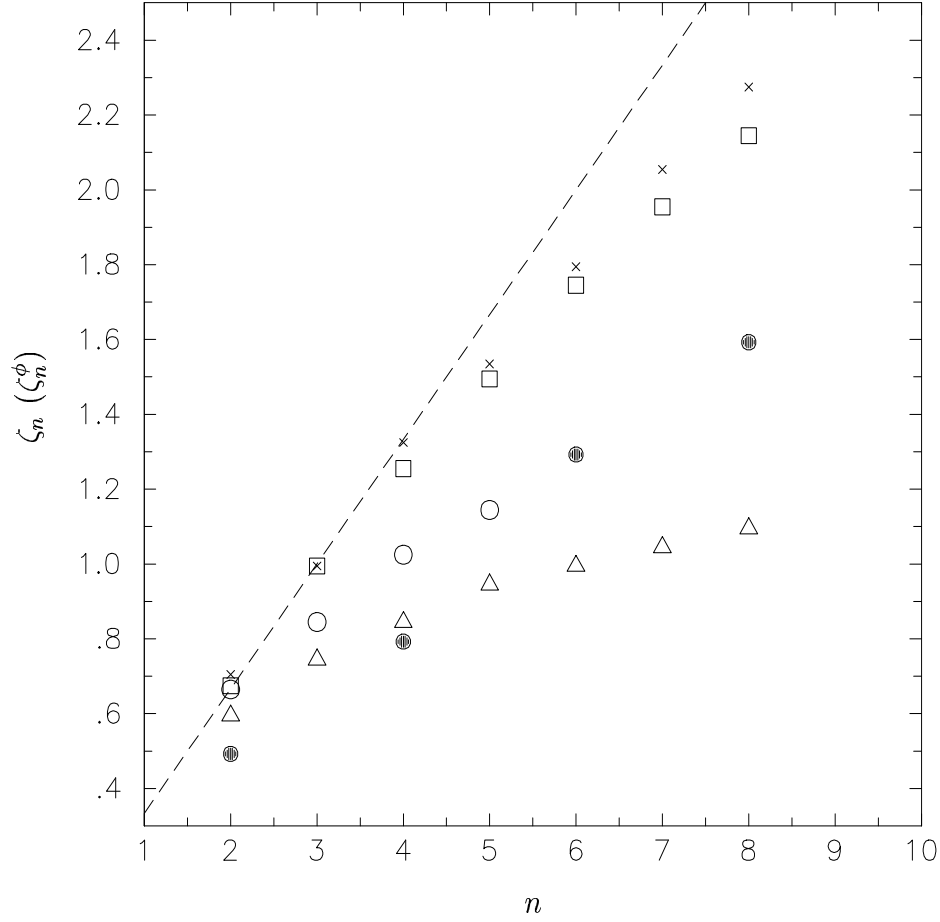


FIG. 3.10. Scaling exponents for scalar structure functions and longitudinal velocity structure functions. Triangles and squares are DNS results at $R_\lambda \approx 390$, for scalar structure functions and longitudinal velocity structure functions, respectively. Circles are for scalar structure functions at $R_\lambda \approx 461$ and $Pr \approx 0.71$ from Mydlarski and Warhaft (1998) for temperature field in grid turbulence. Crosses are for longitudinal velocity structure functions at $R_\lambda \approx 536$ from Anselmet *et al.* (1984) for a turbulent jet. Dashed line with a slope of $1/3$ is shown to represent KOC prediction. Solid circles are from p.166(c) of Dasi (2004) for $Sc \approx 1000$ at $Re10000$, $x = 2m$ for turbulent boundary layers.

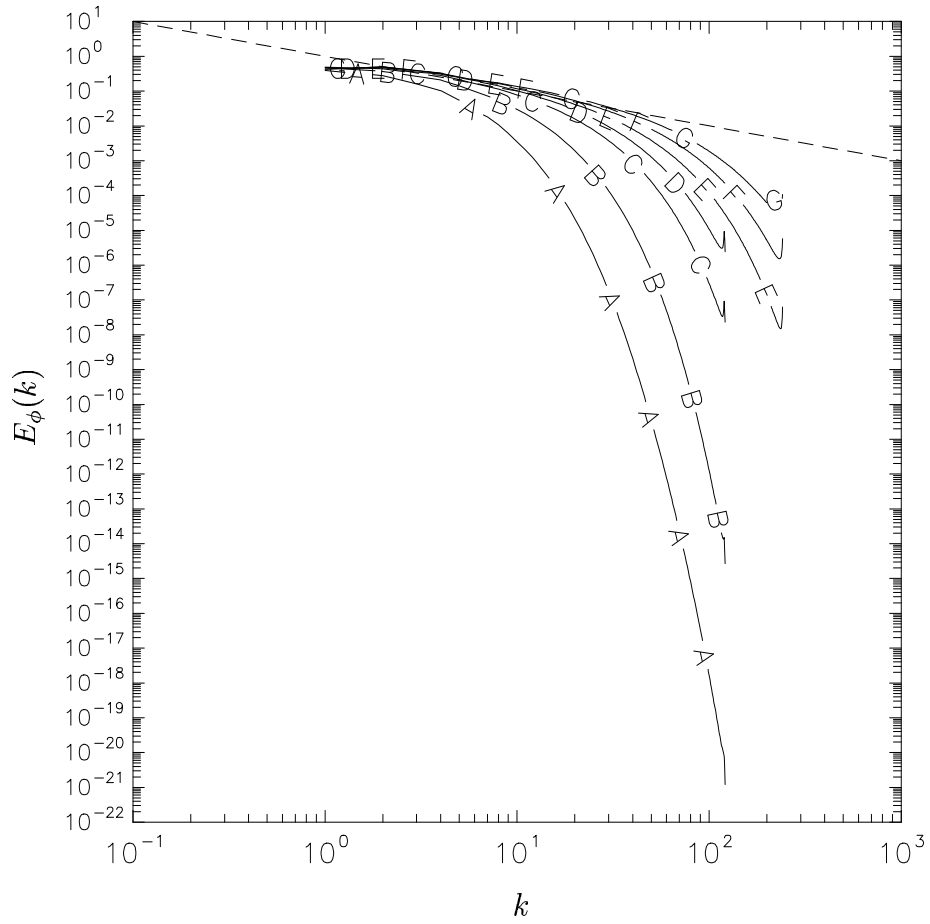


FIG. 3.11(a). Three-dimensional spectra at $R_\lambda \approx 38$ for scalars of Schmidt numbers $1/4, 1, 4, 8, 16, 32, 64$ (lines A to G respectively). The dashed line has a slope of -1 on logarithmic scales.

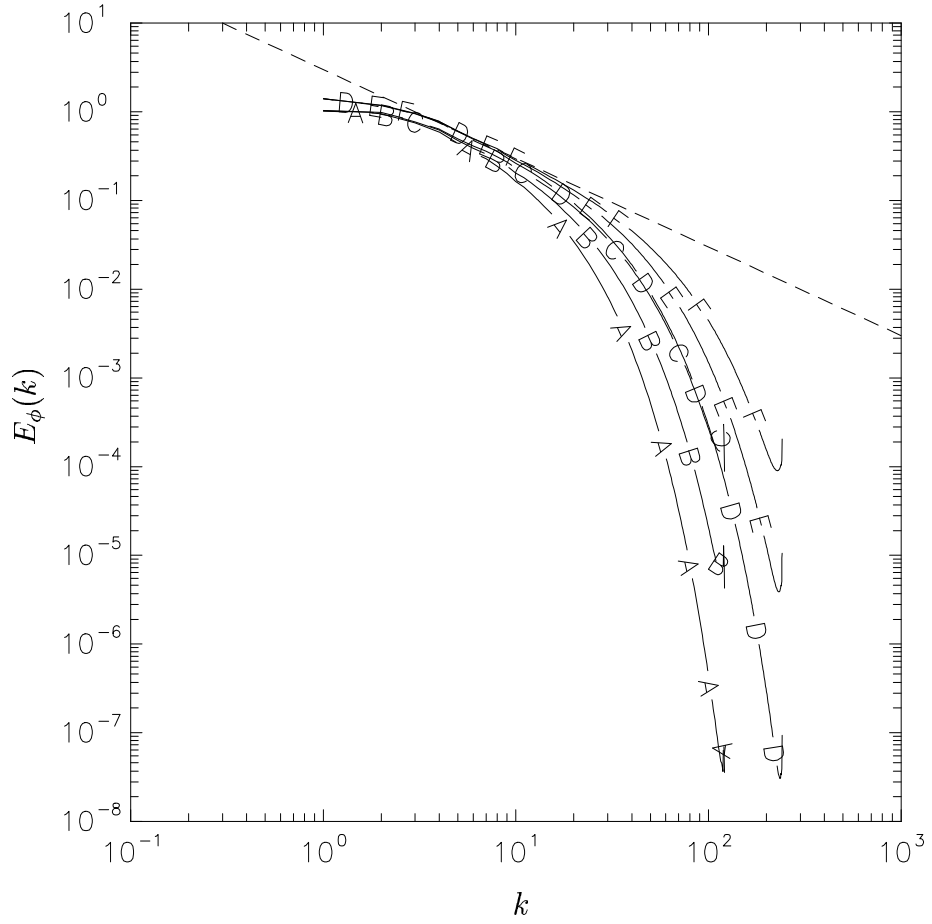


FIG. 3.11(b). Three-dimensional spectra at $R_\lambda \approx 8$ for scalars of Schmidt numbers 64, 128, 256 (256^3) and 256, 512, 1024 (512^3) (lines A to F respectively). The dashed line has a slope of -1 on logarithmic scales.

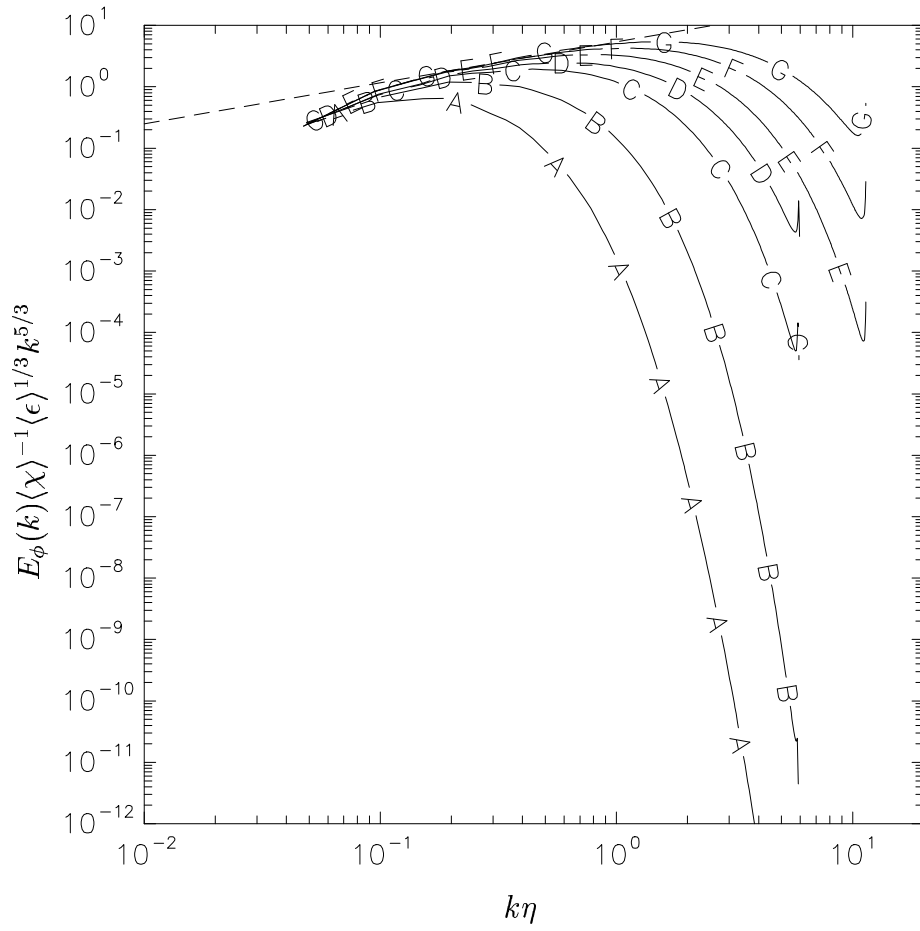


FIG. 3.12(a). Three-dimensional spectra normalized by Kolmogorov scaling. Same data as FIG. 3.11(a). The dashed line has a slope of $2/3$.

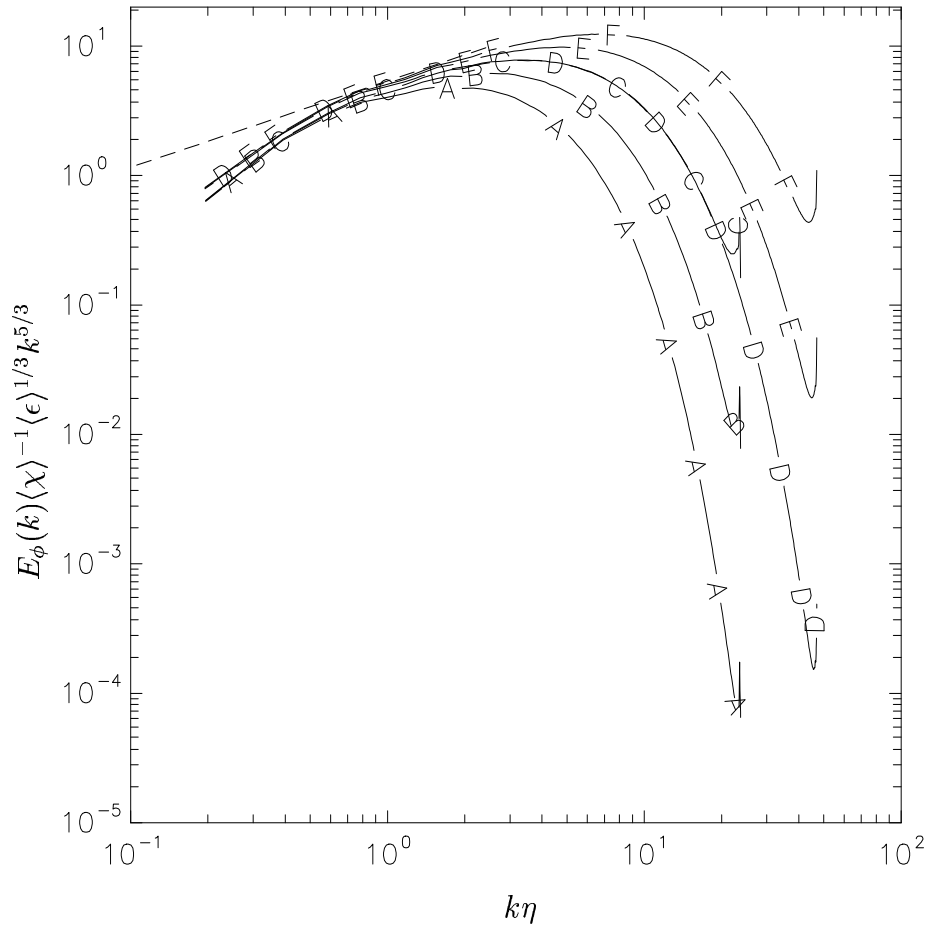


FIG. 3.12(b). Same as FIG. 3.12(a), except at $R_\lambda \approx 8$ for $Sc = 64, 128, 256$ (256^3) and $Sc = 256, 512, 1024$ (512^3) (line A to F, respectively).

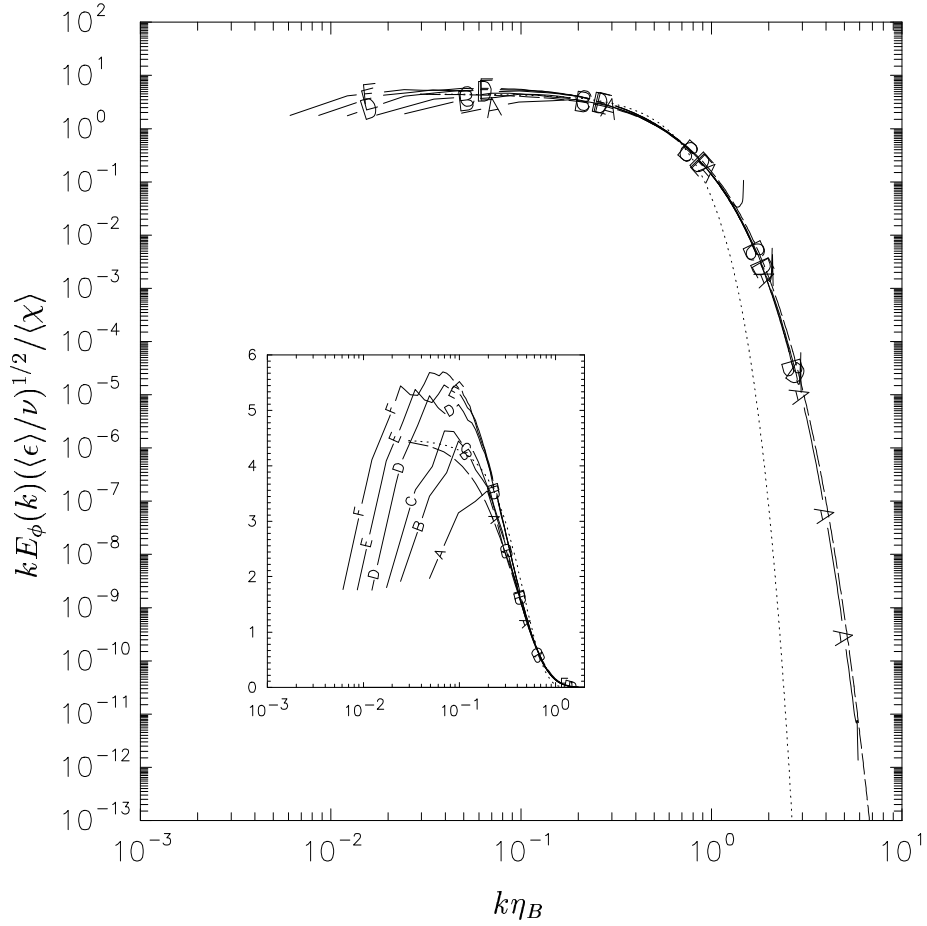


FIG. 3.13(a). Three-dimensional scalar spectrum normalized by Batchelor variables at $R_\lambda \approx 38$ for $Sc = 1, 4, 8, 16, 32, 64$ (lines A-F, respectively). Dotted curve for Batchelor's expression (Eq. 3.13), dashed curve for Kraichnan's (Eq. 3.14). Inset shows the same data in log-linear scales.

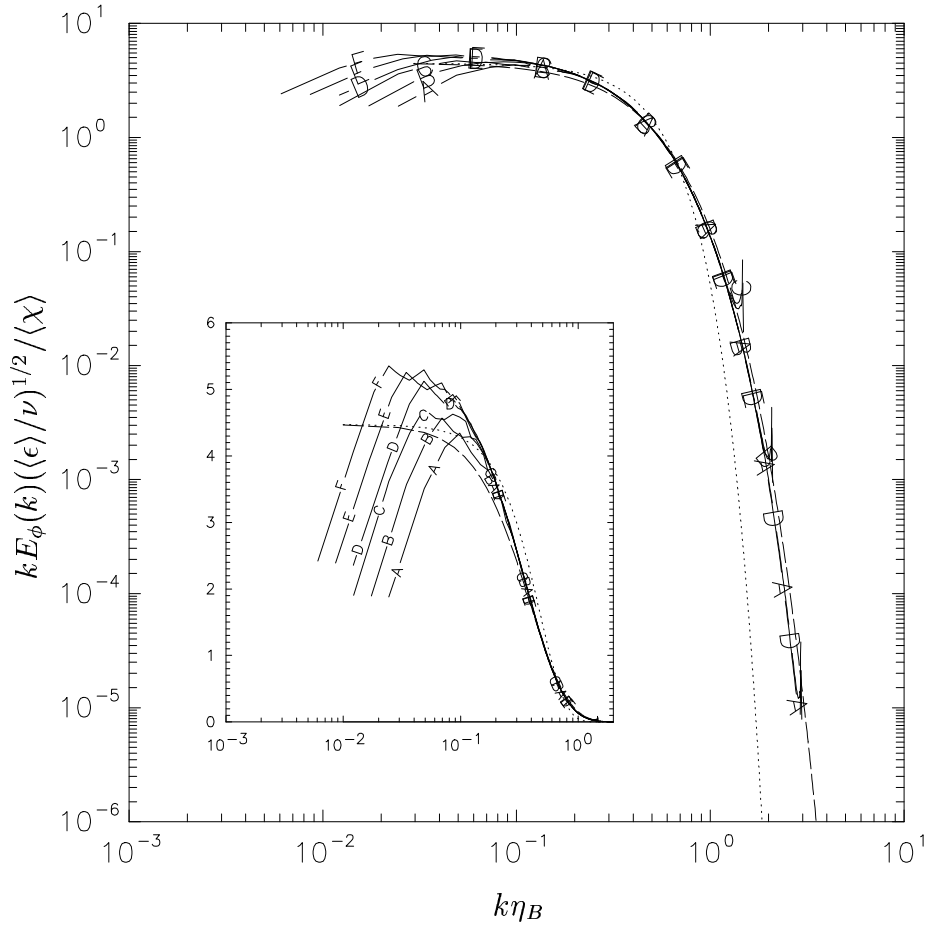


FIG. 3.13(b). Same as FIG. 3.13(a), except at $R_\lambda \approx 8$ for $Sc = 64, 128, 256$ (256^3) and $256, 512, 1024$ (512^3) (lines A-F, respectively).

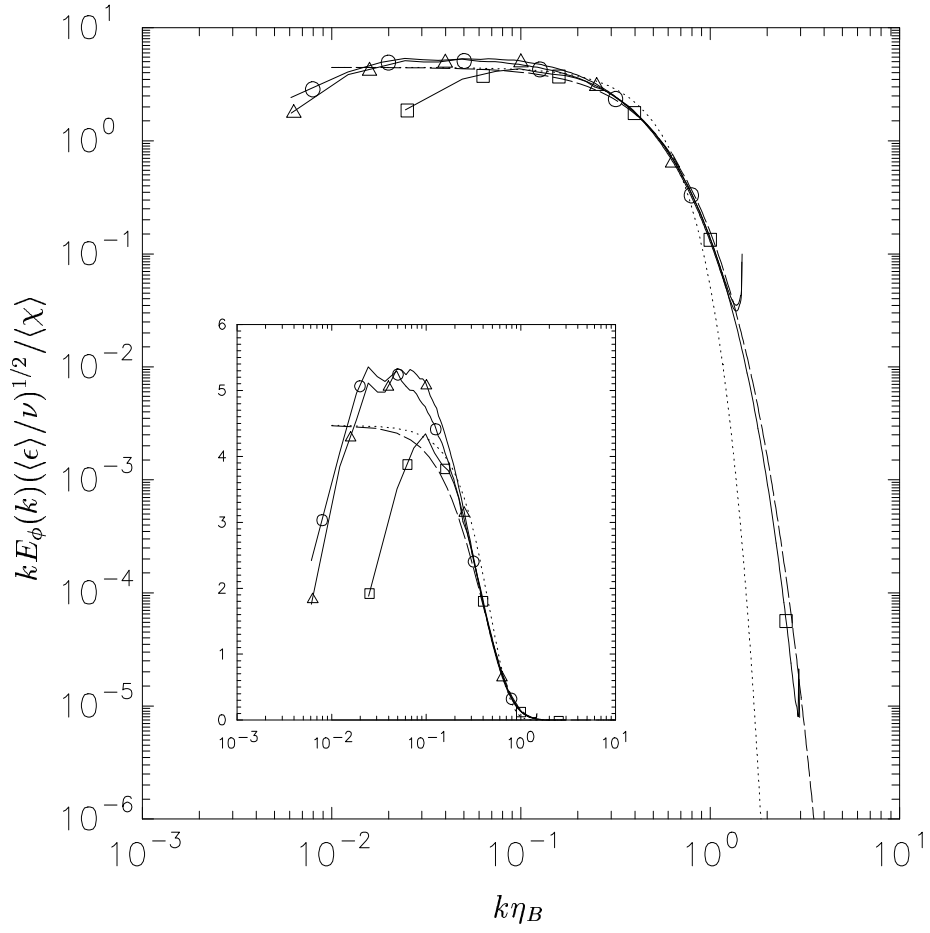


FIG. 3.14. Same as FIG. 3.13(a), except for $R_\lambda \approx 38$ and $Sc = 64$ (triangle), $R_\lambda \approx 8$ and $Sc = 64$ (square) and $R_\lambda \approx 8$ and $Sc = 1024$ (circle).

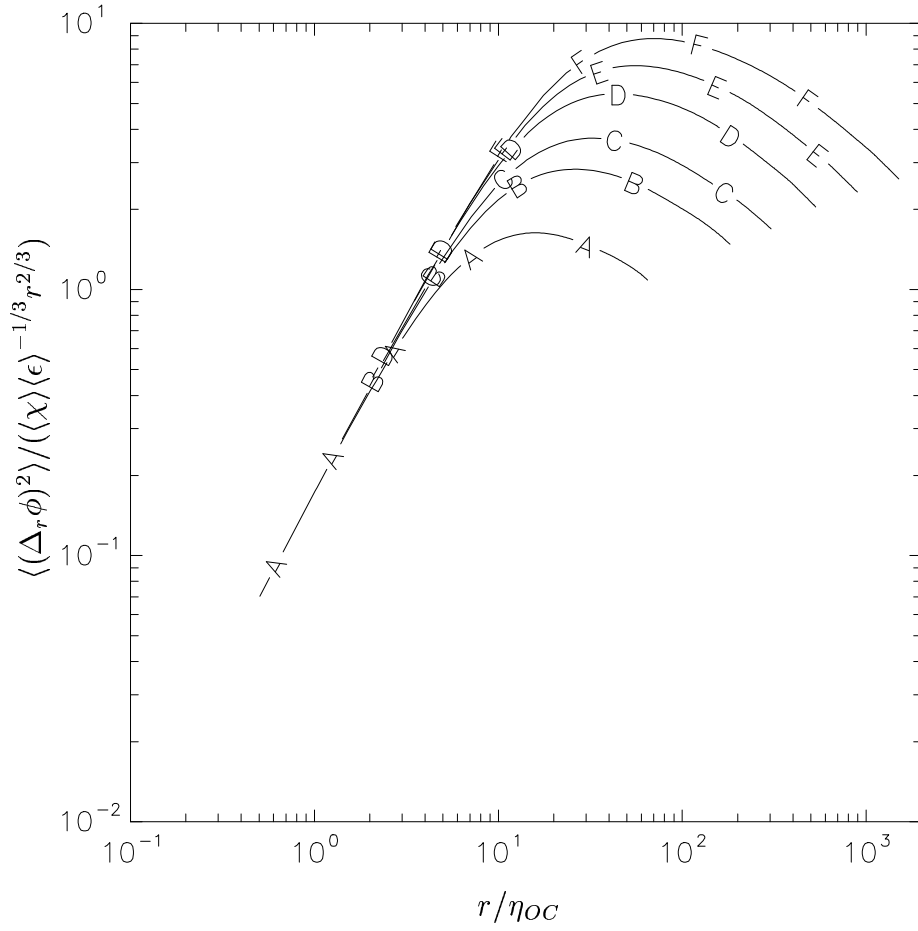


FIG. 3.15(a). Scaling of second-order scalar structure function (similar to FIG. 3.3) for scalars of $Sc = 1, 4, 8, 16, 32, 64$ (lines A-F, respectively) at $R_\lambda \approx 38$.

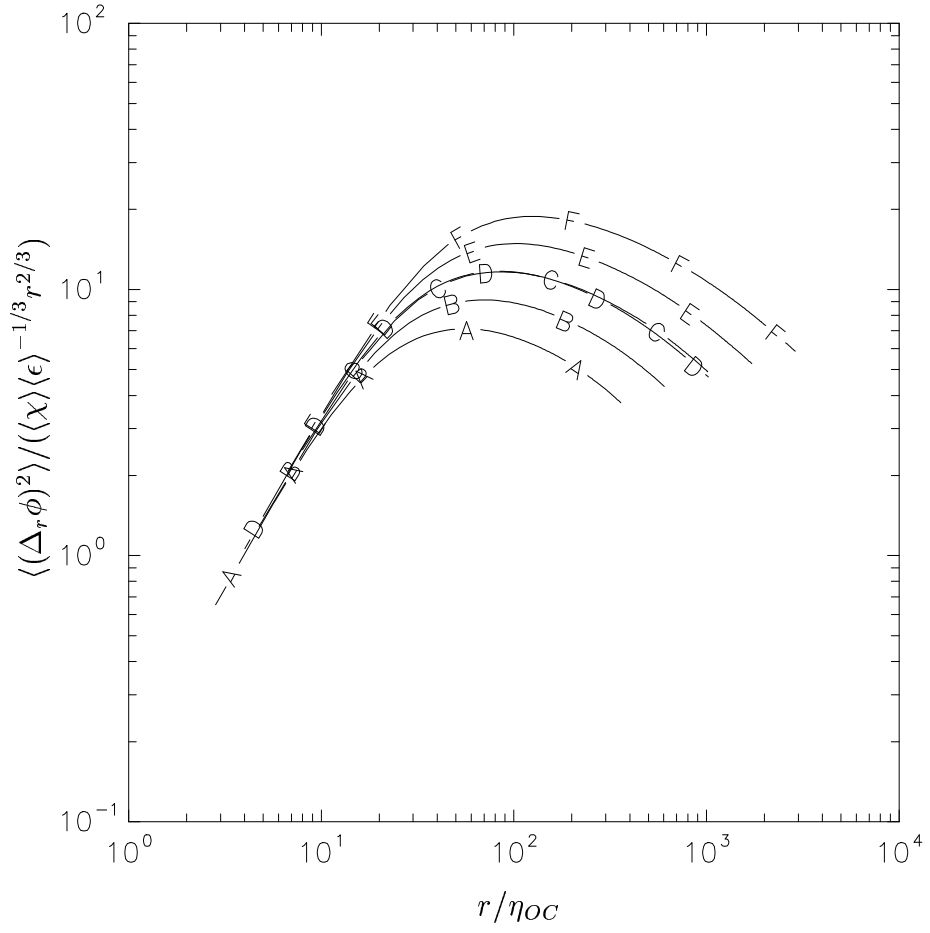


FIG. 3.15(b). Same as FIG. 3.15(a) except for $Sc = 64, 128, 256$ (256^3) and $Sc = 256, 512, 1024$ (512^3) at $R_\lambda \approx 8$ (lines A-F, respectively).

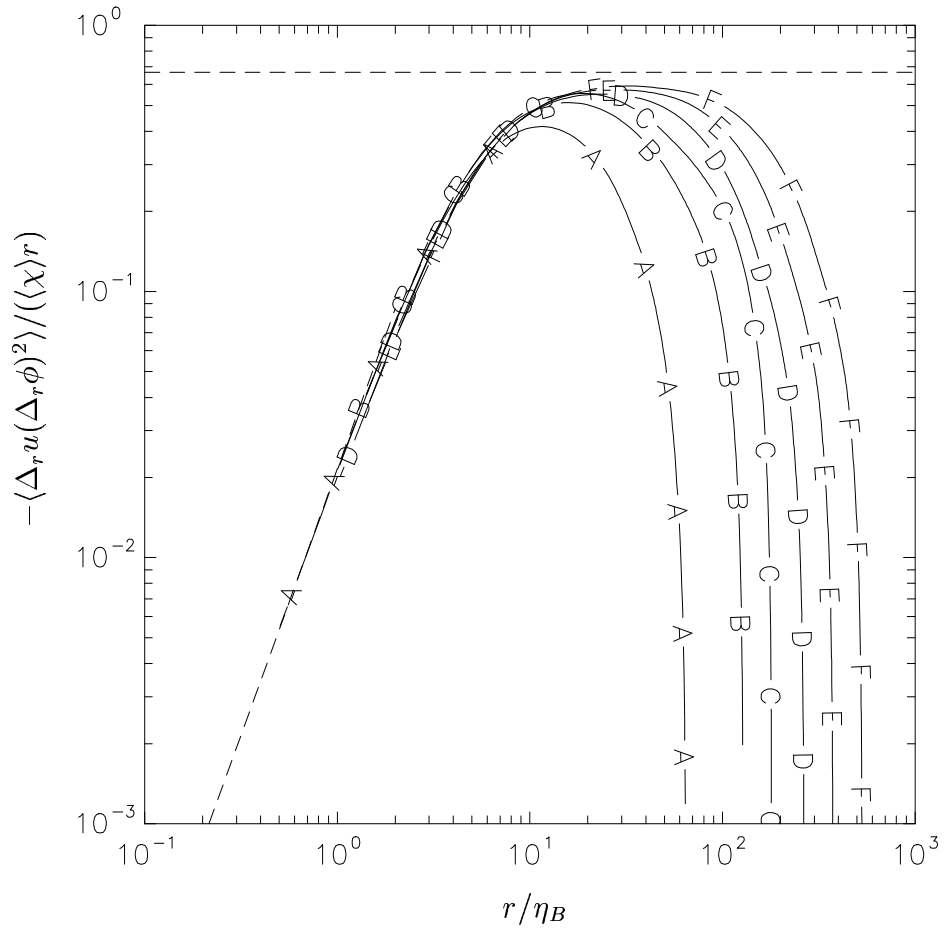


FIG. 3.16(a). Scaling of mixed third-order velocity-scalar structure function (similar to FIG. 3.4) for scalars with $Sc = 1, 4, 8, 16, 32, 64$ (lines A-F, respectively) at $R_\lambda \approx 38$.

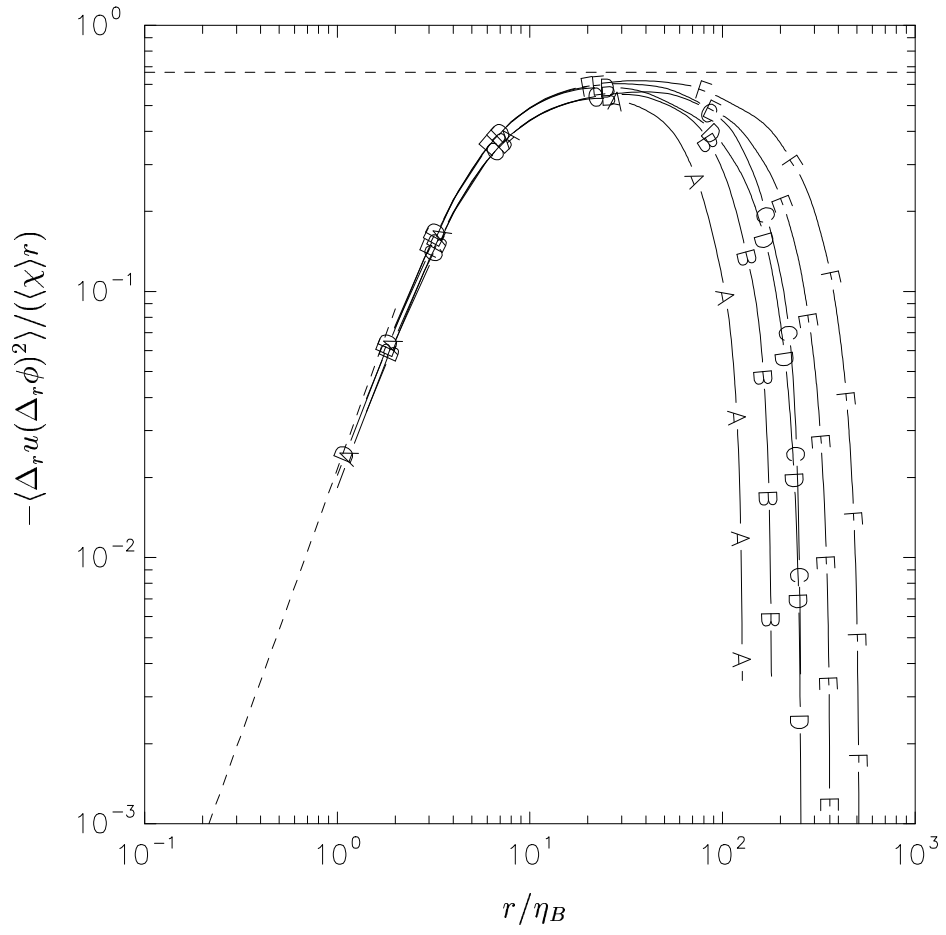


FIG. 3.16(b). Same as FIG. 3.16(a) except for $Sc = 64, 128, 256$ (256^3) and $Sc = 256, 512, 1024$ (512^3) at $R_\lambda \approx 8$ (lines A-F, respectively).

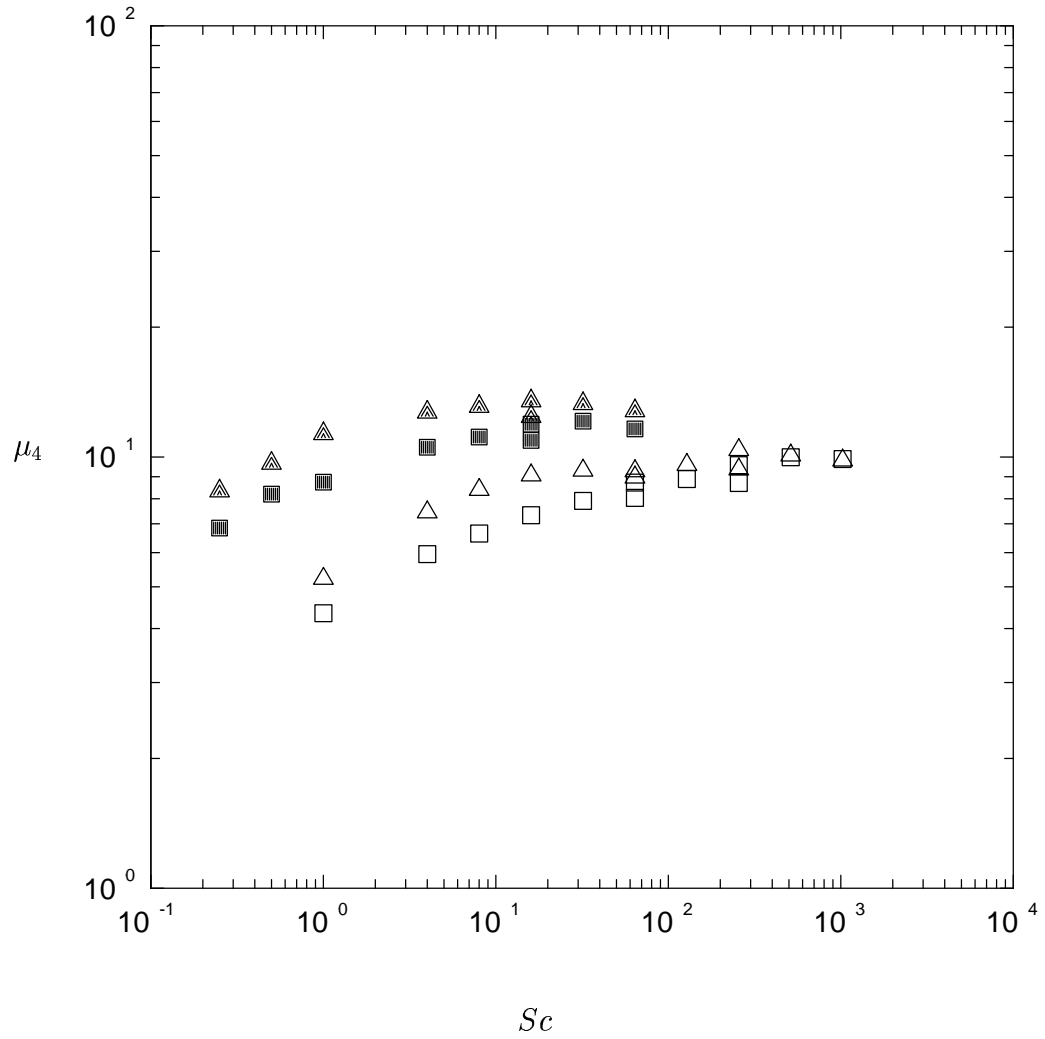


FIG. 3.17(b). Kurtosis of scalar gradients. Triangles are for $\Delta_{\parallel}\phi$ and squares are for $\Delta_{\perp}\phi$. Close symbols are for $R_{\lambda} \approx 38$, and open symbols for $R_{\lambda} \approx 8$.

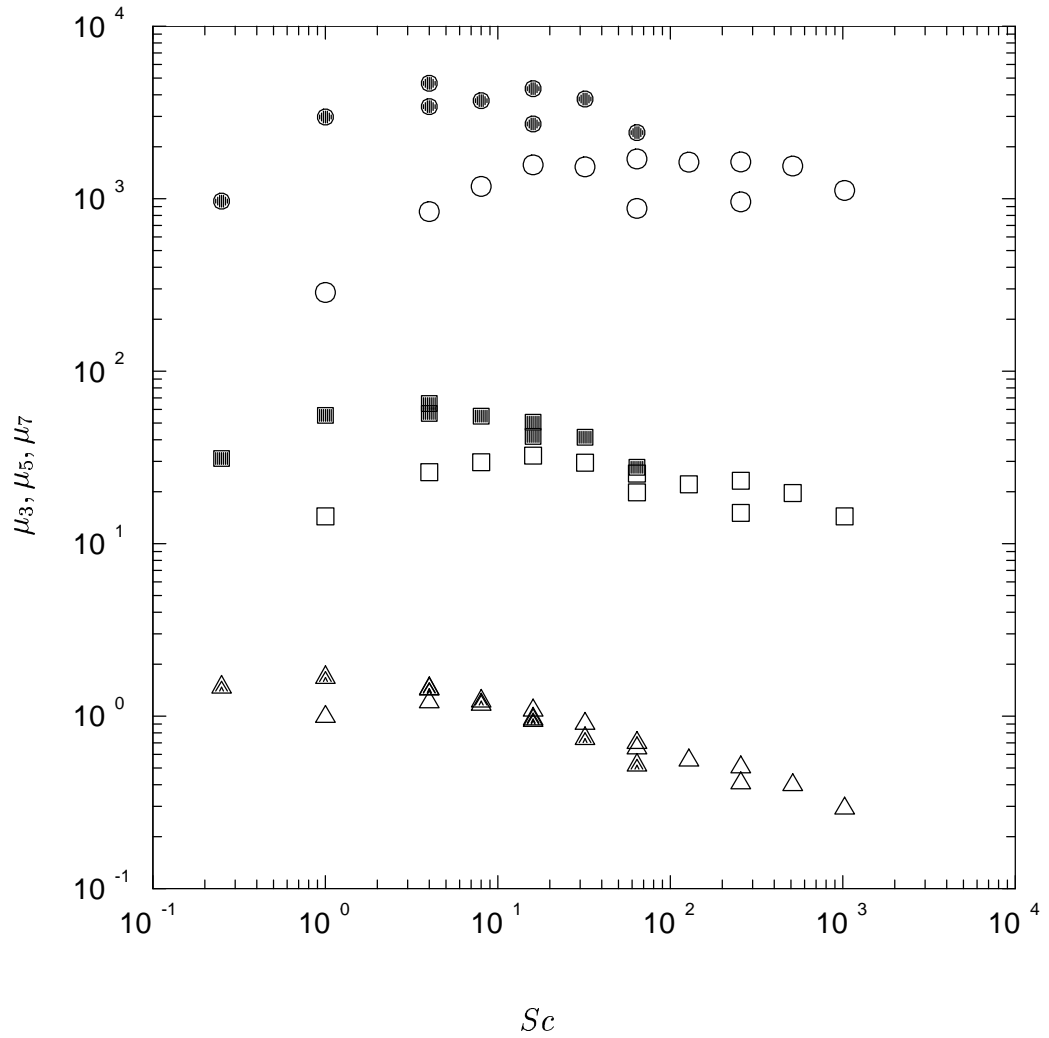


FIG. 3.17(c). Normalized odd-order moments of scalar gradients. Triangles are for μ_3 , squares are for μ_5 and circles are for μ_7 . Close symbols are for $R_\lambda \approx 38$, and open symbols for $R_\lambda \approx 8$.

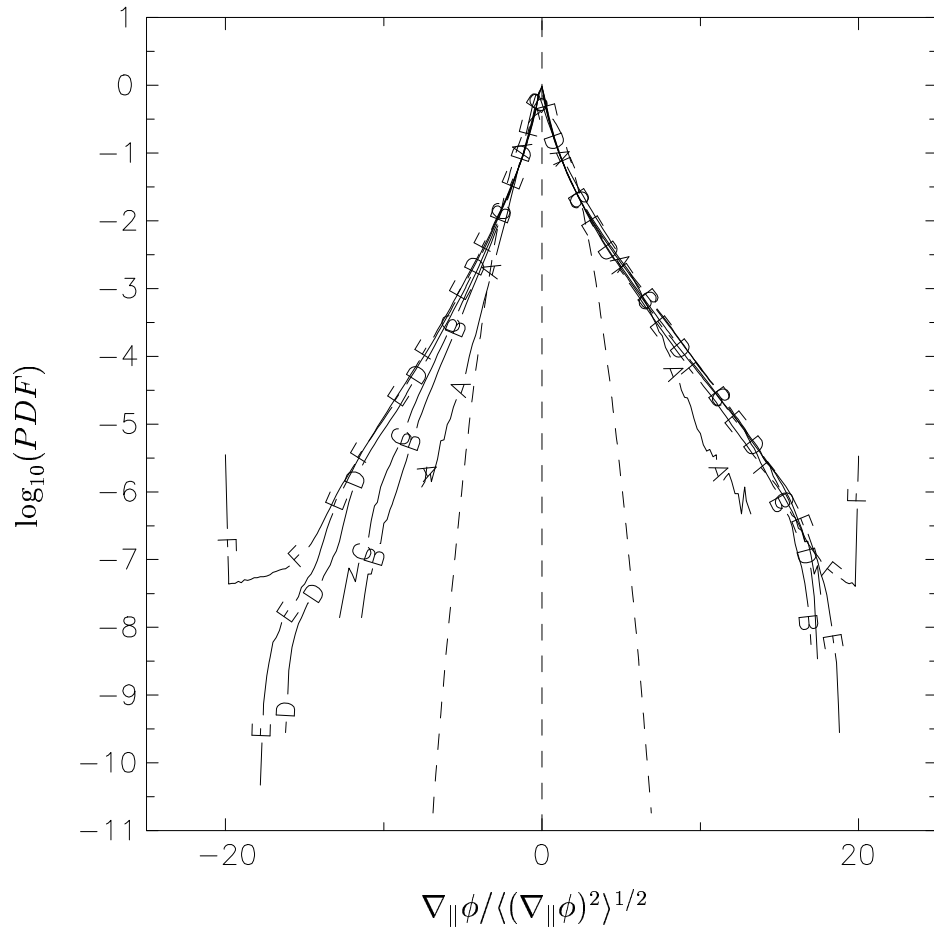


FIG. 3.18(a). Standardized probability density function (shown as base-10 logarithm) of $\nabla_{\parallel} \phi$ for scalars of Schmidt numbers 1, 4, 8, 16, 32, 64 (lines A to F respectively) at $R_{\lambda} \approx 38$. Dashed curve shows a Gaussian distribution for comparison.

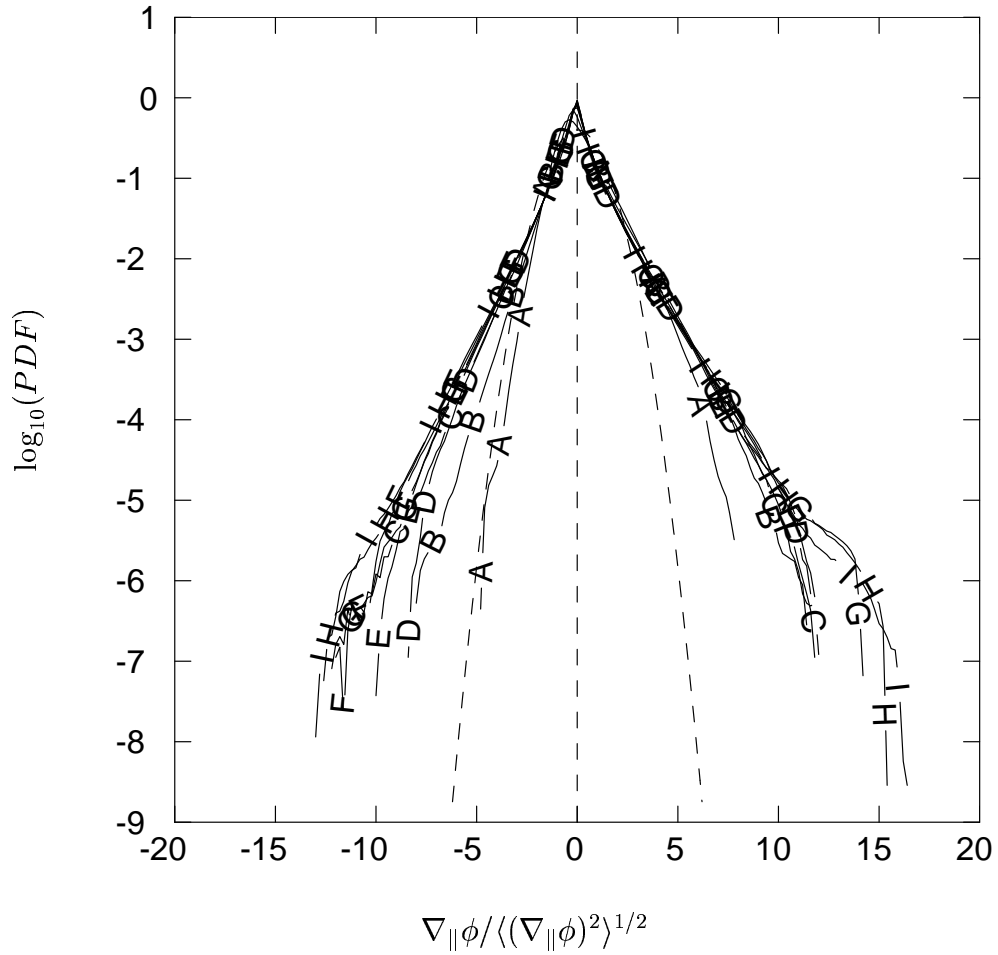


FIG. 3.18(b). Standardized probability density function (shown as base-10 logarithm) of $\nabla_{\parallel}\phi$ for scalars of Schmidt numbers 1, 8, 64 (lines A-C, 128^3), 64, 128, 256 (lines D-F, 256^3) and 256, 512, 1024 (lines G-I, 512^3) at $R_{\lambda} \approx 8$. Dashed curve shows a Gaussian distribution for comparison.

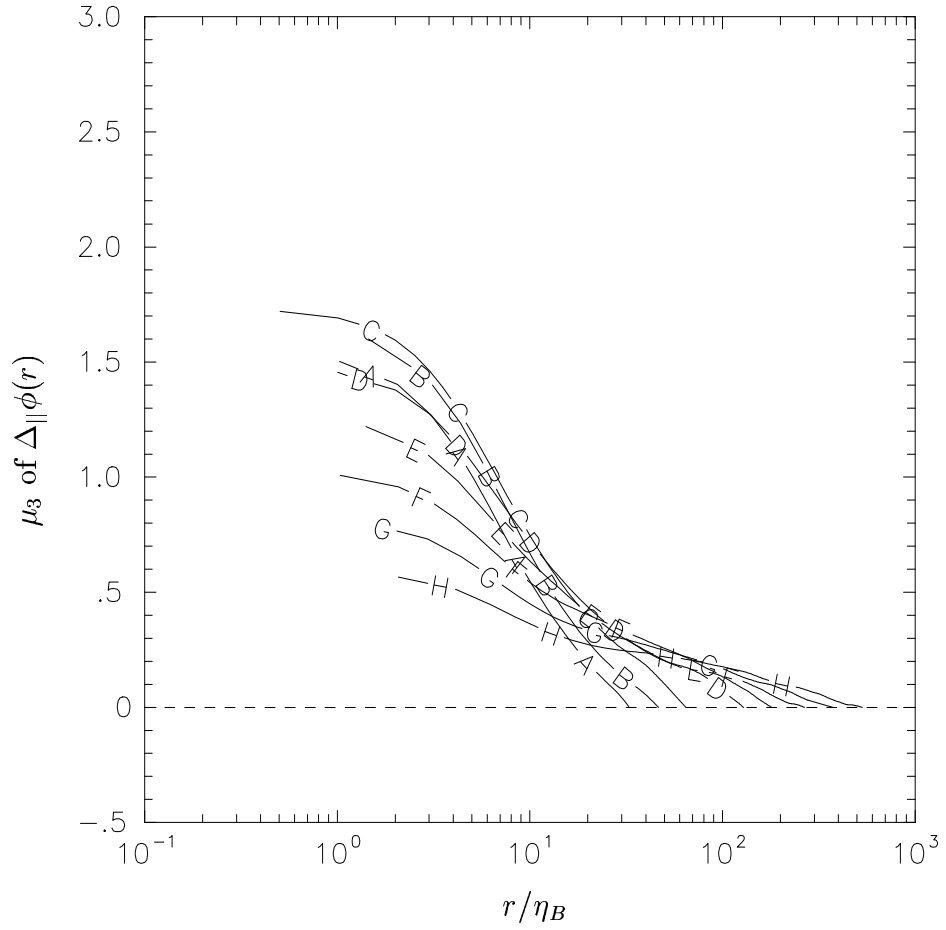


FIG. 3.19(a). The skewness structure function of $\nabla_{\parallel}\phi$ (Eq. 3.17) as a function of separation on Batchelor scales, for scalars of Schmidt numbers 1/4, 1/2, 1, 4, 8, 16, 32, 64 (lines A to H respectively) at R_{λ} 38. Dashed line shows Gaussian value of 0.

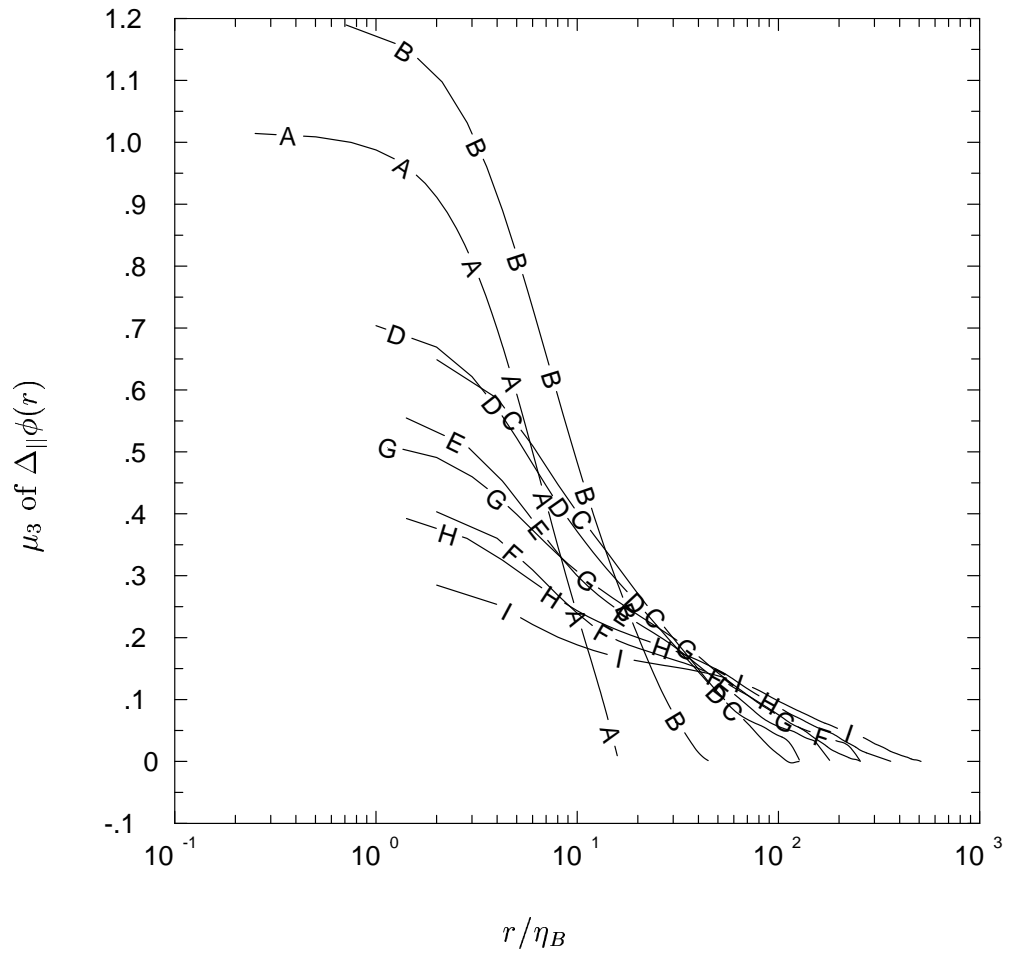


FIG. 3.19(b). Same as FIG. 3.19(a), except for Schmidt numbers 1, 8, 64 (lines A-C, 128^3), 64, 128, 256 (lines D-F, 256^3) and 256, 512, 1024 (lines G-I, 512^3).

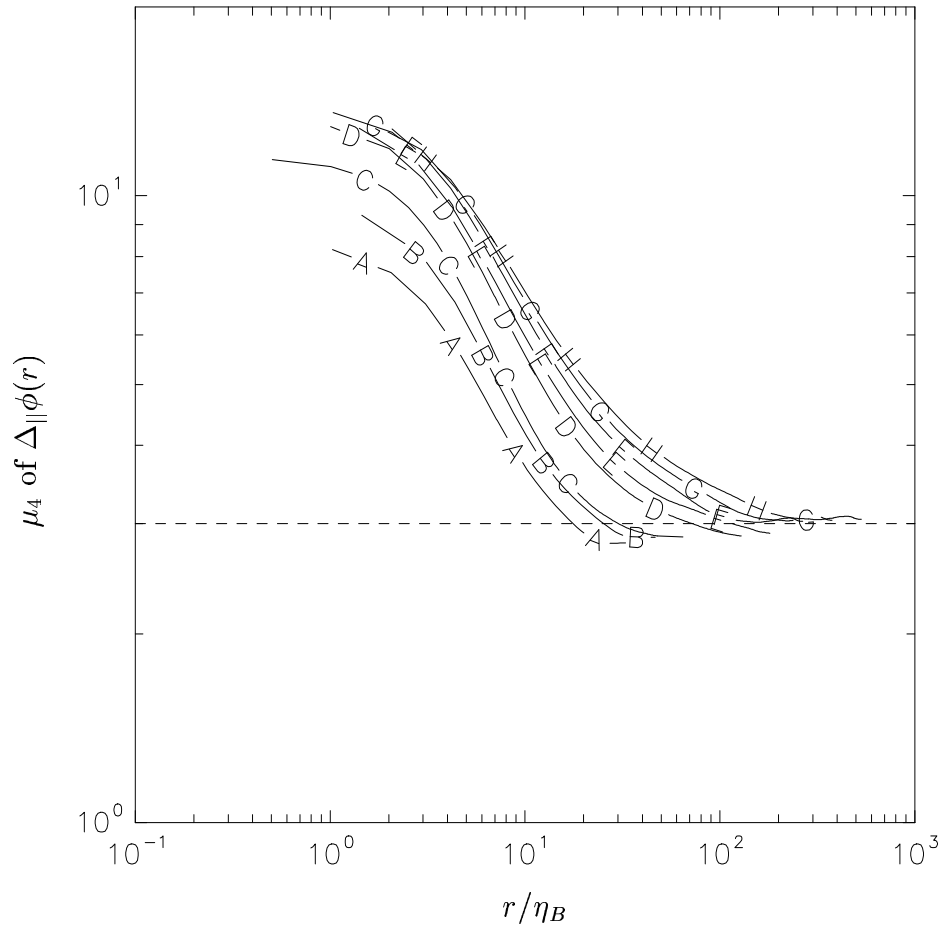


FIG. 3.20(a). The flatness structure function of $\nabla_{\parallel}\phi$ with symbols same as FIG. 3.19(a). Dashed line shows Gaussian value of 3.

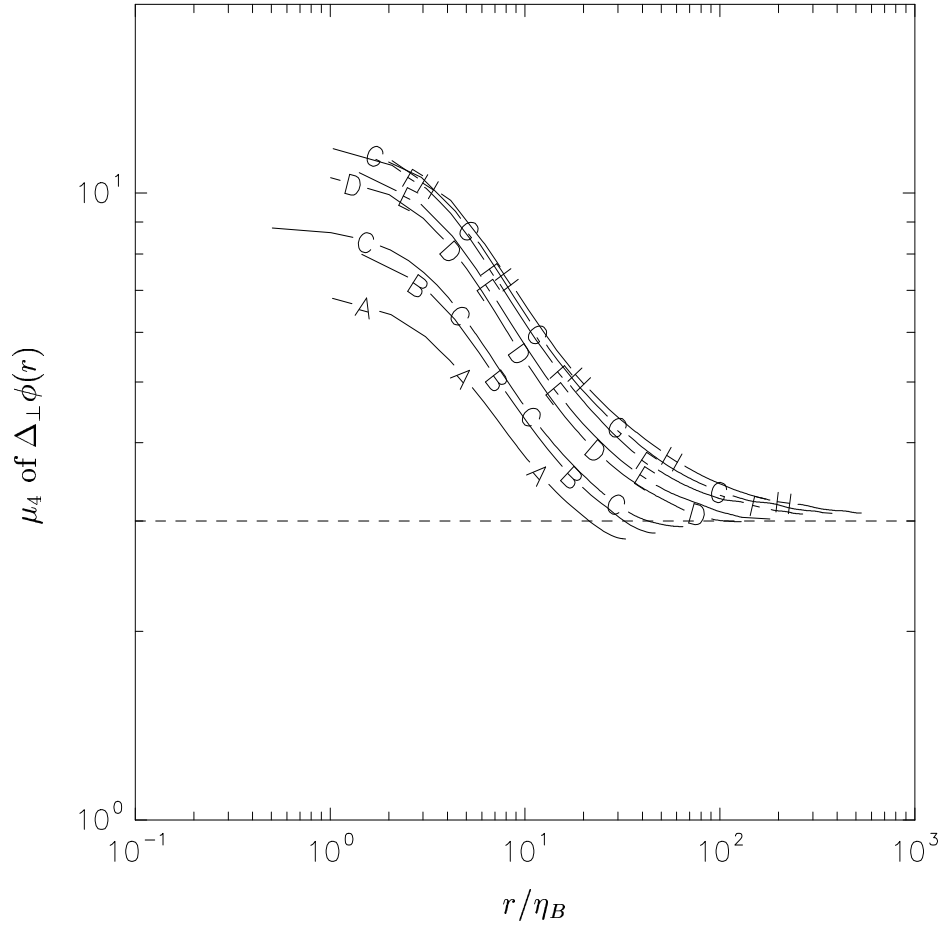


FIG. 3.20(b). The flatness structure function of $\nabla_{\perp}\phi$ with symbols same as FIG. 3.20(a).

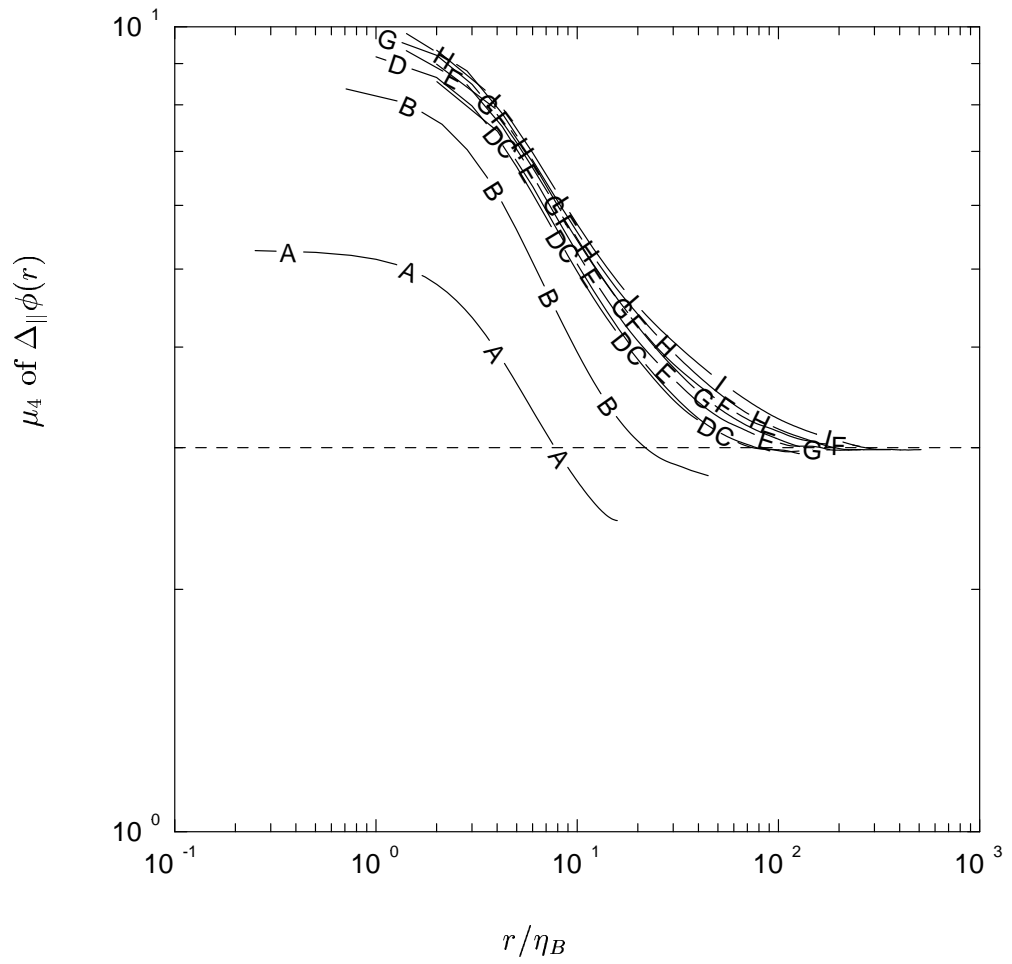


FIG. 3.21(a). The flatness structure function of $\nabla_{\parallel}\phi$ with symbols same as FIG. 3.19(b).

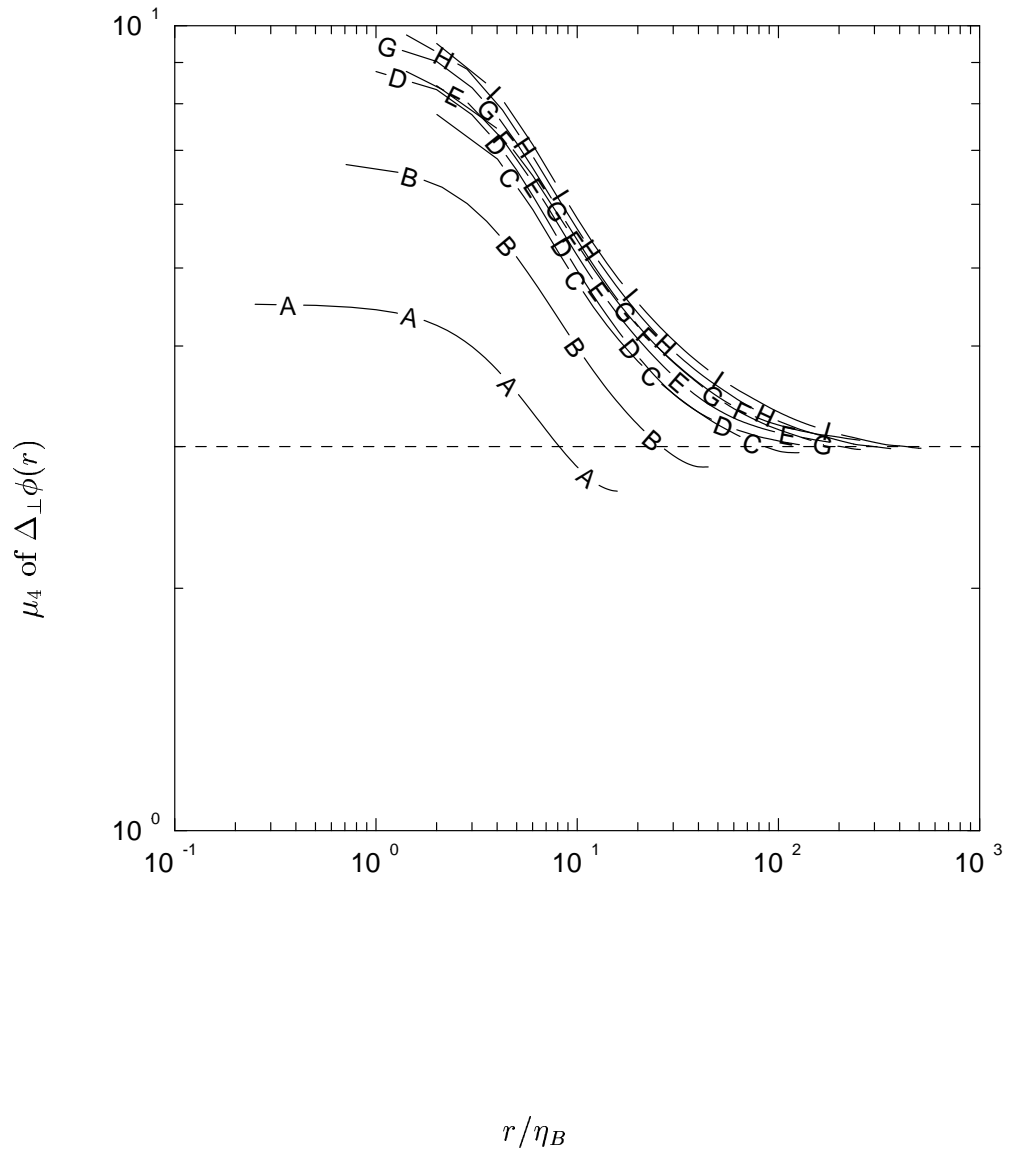


FIG. 3.21(b). The flatness structure function of $\nabla_{\perp}\phi$ with symbols same as FIG. 3.19(b).

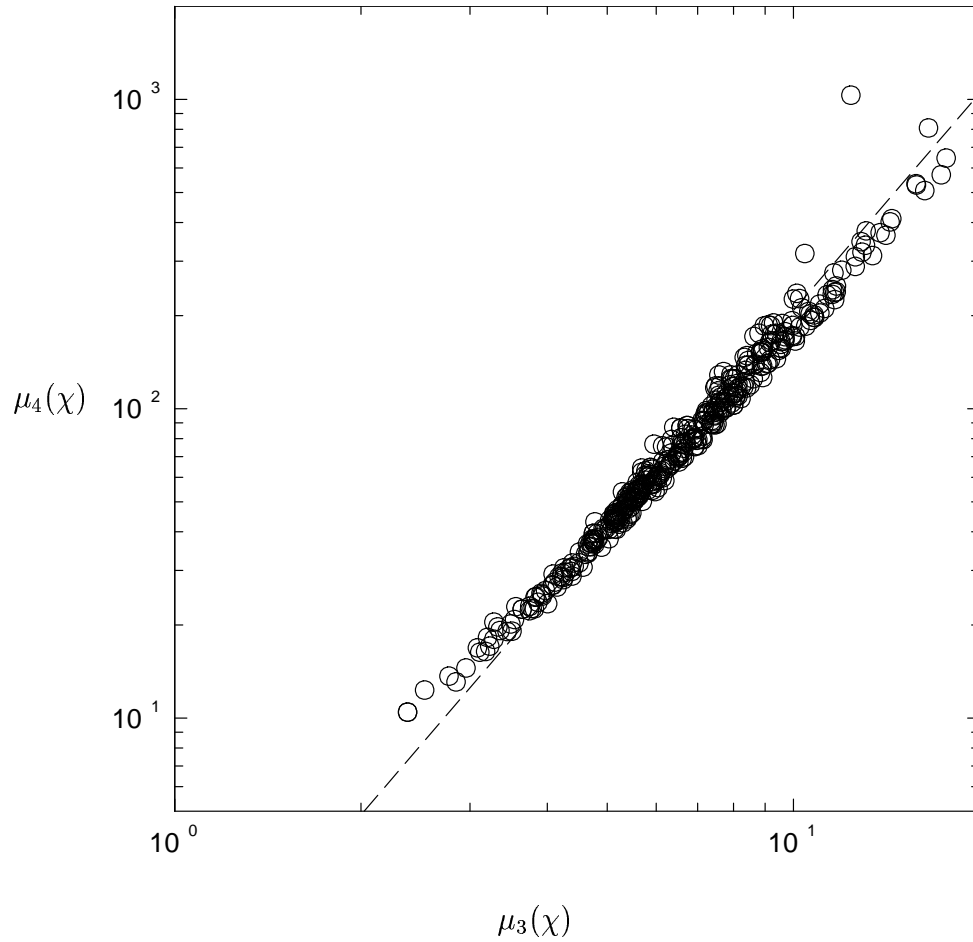


FIG. 3.22. Plot of flatness versus skewness for the scalar dissipation. Each data point represents one realization taken from our data sets at various Reynolds numbers of $R_\lambda \approx 8$, $R_\lambda \approx 38$, $R_\lambda \approx 140$, $R_\lambda \approx 240$ and $R_\lambda \approx 390$. The dashed line is a least-square fit, with a slope of 2.33.

CHAPTER IV

INTERMITTENCY EXPONENTS OF ENERGY AND SCALAR DISSIPATION

In this chapter, the two-point statistics of energy and scalar dissipation are studied, which contain information on intermittency at different scale sizes. The effects of Schmidt number and Reynolds number on the intermittency properties are discussed through intermittency exponent, which is the power law exponent of the two-point statistics in a certain scaling range.

4.1 Background

Inertial range intermittency in turbulence has been found in many experimental and numerical investigations, which show discrepancies of scaling exponents from the prediction of self-similar theories of Kolmogorov (1941), Obukhov (1949) and Corrsin (1951). Kolmogorov (1962) introduced the log-normal model for energy dissipation, which provides adjustment to the scaling exponent of local energy dissipation ϵ_r averaged over a sphere of diameter r . Inclusion of intermittency effects will affect the scaling of spectrum in wavenumber space, structure functions and the two-point statistics of dissipation.

In the literature (Sreenivasan and Kailasnath 1993) several related definitions for intermittency exponents have been used. Three definitions of the intermittency exponent are considered, two of which are based on the local average ϵ_r and one is derived from the two-point correlators of ϵ evaluated at spatial separations in the inertial range. Kolmogorov (1962) conjectured that the second-order moments of local energy dissipation has scaling behavior

$$\langle \epsilon_r^2 \rangle \sim r^{-\mu_1}, \quad (4.1)$$

where μ_1 is a positive constant that is usually referred to as the intermittency exponent. It

follows from the lognormal assumption that the n^{th} order moment of ϵ_r scales as

$$\langle \epsilon_r^n \rangle \sim r^{-n(n-1)\mu_1/2}. \quad (4.2)$$

The corresponding structure functions scale as

$$\langle (\Delta_r u)^n \rangle \sim r^{n[1-1/6\mu_1(n-3)]/3}, \quad (4.3)$$

where the term containing μ_1 is the intermittency correction to the Kolmogorov's (1941) $r^{n/3}$ scaling. The inertial range spectrum will also be modified according to

$$E(k) \sim k^{-(5/3+\mu_1/9)}. \quad (4.4)$$

Hence, determination of the intermittency exponent μ_1 is useful for assessing intermittency correction to the energy spectrum, structure functions and the two-point statistics of dissipation. The behavior of ϵ_r and the value of μ_1 is often of great interest in various intermittency models such as the multifractal model (Meneveau and Sreenivasan 1987, 1991) and the mapping closure model (She and Orszag 1991), to name a few. The general relation between the structure functions and moments of local energy dissipation that is independent of specific intermittency model is

$$\langle (\Delta_r u)^m \rangle \sim r^{m/3} \langle \epsilon_r^{m/3} \rangle, \quad (4.5)$$

i.e., $\zeta_m = m/3 + \tau_{m/3}$, where $\langle (\Delta_r u)^m \rangle \sim r^{\zeta_m}$ and $\langle \epsilon_r^m \rangle \sim r^{-\tau_m}$.

Kolmogorov (1962) also suggests that the variance of $\ln \epsilon_r$ varies with r in the form

$$\sigma_{\ln \epsilon_r}^2 = A + \mu_2 \ln(L/r), \quad (\eta \ll r \ll L), \quad (4.6)$$

where L is a large-eddy length scale, and A is a coefficient dependent on the large scales. However, accurate evaluation of the statistics of ϵ_r is difficult because averaging over many data points is required to produce each sample of ϵ_r , especially in three dimensions. It is easier to use the two-point correlator

$$\langle \epsilon(x)\epsilon(x+r) \rangle \sim \langle \epsilon \rangle^2 (r/L)^{-\mu_3}, \quad (\eta \ll r \ll L), \quad (4.7)$$

which expresses the statistical relationships between fluctuations of ϵ at two points at distance r apart in space. If a line average is used to define ϵ_r then an exact relationship applicable for homogeneous turbulence is (Monin & Yaglom 1975, p. 618)

$$\langle \epsilon(x)\epsilon(x+r) \rangle = \frac{1}{2} \frac{d^2}{dr^2} (r^2 \langle \epsilon_r^2 \rangle) . \quad (4.8)$$

This relation implies that if a well-defined scaling range exists then μ_1 and μ_3 should be equivalent to each other, although not necessarily equal to μ_2 .

Most of the known results in the literature (Sreenivasan *etal.* 1993, Sreenivasan & Antonia 1997) suggest intermittency exponent μ_1 and μ_3 for the energy dissipation rate to be about 0.25 ± 0.05 , with no strong dependence on the Reynolds number. A considerable fraction of the known data on this subject has been derived from experiments, where, because of measurement limitations, one-dimensional surrogates (e.g. the squared velocity gradient, $(\partial u/\partial x)^2$) are typically studied in place of the full dissipation rate, and Taylor's frozen turbulence hypothesis is often invoked to convert time derivatives to space derivatives. However, there is no guarantee that the full dissipation rate would have the same behavior. Recent work comparing longitudinal and transverse velocity structure functions (e.g. Chen *etal.* 1997, Shen & Warhaft 2000) also suggest that longitudinal and transverse velocity gradients have different scaling exponents. Exponents for symmetric and anti-symmetric components of the velocity gradient tensor leading to energy dissipation and enstrophy (vorticity squared) respectively may also differ, at least at moderate Reynolds numbers. A detailed understanding of possible differences in inertial-range intermittency of different components of velocity gradients is thus important, and would also help resolve the issue (Nelkin 1999) of whether observed differences in the intermittency of enstrophy and energy dissipation would vanish in the high Reynolds number limit. In addition to the velocity field, important questions also arise in characterizing the intermittency of the dissipation rate of passive scalar fluctuations as a function of the Schmidt number which can vary widely in applications.

For the scalar dissipation rate, the scaling range of interest depends on the Schmidt number. In particular, two ranges are considered: (a) the inertial-convective range $\{\eta, \eta_{OC}\} \leq$

$r \leq L$ based on the Obukhov-Corrsin scale $\eta_{OC} = \eta Sc^{-3/4}$ for scalars with $Sc = O(1)$ or less at high Reynolds number, and (b) the viscous-convective range $\eta > r > \eta_B$ based on the Batchelor scale $\eta_B = \eta Sc^{-1/2}$ for scalars with $Sc \gg 1$.

In Sec. 4.2, discussions of results on intermittency exponents of the velocity field for energy dissipation and enstrophy and issues of one-dimensional surrogacy for energy dissipation are given. Section 4.3 provides discussions on intermittency exponents of scalar dissipation, including the issues of Reynolds number and Schmidt number effects and the properties of one-dimensional surrogates represented by one component of scalar gradient.

4.2 *Velocity field intermittency*

In this section, basic results are presented on inertial-range intermittency exponents of the energy dissipation rate and enstrophy at different Reynolds numbers. The effects of surrogacy and dimensionality of local averaging are also studied.

For some background information, it is necessary to refer to several one-point statistics of the dissipation as given in Table 4.1. The mean dissipation rate is mainly set by forcing parameters (i.e. energy input at the large scales) and hence almost the same in the higher Reynolds number runs where the viscosity has been varied while the forcing parameters are kept fixed. The increase of intermittency with Reynolds number can be seen directly via the ratio $\langle \epsilon^2 \rangle / \langle \epsilon \rangle^2$, as well as the skewness and flatness of ϵ , which reflect the emergence of wide tails in the probability density function (PDF) of the dissipation rate. The variance of $\ln \epsilon$ also increases with Reynolds number. Although the log-normality hypothesis is known to be inaccurate for high-order moments, the skewness and flatness values of $\ln \epsilon$ are closer to Gaussian (0 and 3 respectively) at higher Reynolds number.

Fig. 4.1(a,b,c) shows the quantities $\sigma_{\ln \epsilon_r}^2$, $\langle \epsilon_r^2 \rangle$ and $\langle \epsilon(x)\epsilon(x+r) \rangle$ (normalized by $\langle \epsilon \rangle^2$) as a function of Kolmogorov-scaled separation at different Reynolds numbers. In principle, in the limit of $r \rightarrow 0$ these quantities should approach the single-point moments in Table 4.1, with both $\langle \epsilon_r^2 \rangle / \langle \epsilon \rangle^2$ and $\langle \epsilon(x)\epsilon(x+r) \rangle / \langle \epsilon \rangle^2$ approaching the dimensionless ratio $\langle \epsilon^2 \rangle / \langle \epsilon \rangle^2$. The DNS results at low Reynolds number agree with this expectation since data points

for r a few times smaller than the Kolmogorov scale are available. In the higher Reynolds number cases, the resolution is $\Delta x \approx 2\eta$ which is not fine enough to reach the small r limit for the second-order moments. This indicates that dissipation fluctuations are highly localized in space and their full resolution demands $\Delta x \ll \eta$ which unfortunately cannot be readily accommodated using the resources available. At the other extreme, as r approaches the size of the solution domain, ϵ_r approaches the global average $\langle \epsilon \rangle$, and $\langle \epsilon(x)\epsilon(x+r) \rangle / \langle \epsilon \rangle^2$ approaches unity as the values of ϵ at two points far apart become statistically independent.

Plots in the form of Fig. 4.1 (giving μ_1 , μ_2 and μ_3 from parts (a), (b) and (c) of the figure respectively) are used to evaluate intermittency exponents, i.e., the slopes of linear segments in the range of r/η that provides the closest resemblance of inertial range behavior. Because a wide scaling range is not expected at Reynolds numbers currently reachable in DNS, the range of r/η for measuring exponents must be chosen very carefully. Based on Anselmet *etal.* (1984), the third-order velocity structure function (whose classical inertial-range form is described by an exact expression free of empirical constants) are used. The DNS results of $\langle (\Delta_r u)^3 \rangle / \langle \epsilon \rangle / r$ (e.g. Fig. 7 in Yeung & Zhou 1997) are plotted and for each curve a range of r is selected such that it appears to be closest to a plateau and also satisfies the condition $\eta \ll r \ll L$. The scaling exponents are taken as the slope of a straight line approximated by least-square method for the data points in the chosen scaling range. The intermittency exponents are also calculated by the method of logarithmic derivatives, i.e., $\frac{d \log \langle \epsilon_r^2 \rangle}{d \log (r/\eta)}$ (Praskovsky and Oncley 1997). Results from these two procedures are quite similar. The inset in Fig. 4.1(c) for the two-point correlator at R_λ 390 shows the logarithmic slopes as a function of r/η where μ_3 is taken as the value of the logarithmic slope at $r/\eta \approx 80$ where the curve is seen to flatten slightly.

The best estimates of the intermittency exponents for energy dissipation and enstrophy (to be discussed later) at $R_\lambda \approx 140, 240$ and 390 are given in Table 4.2. The ranges of r/η where these exponents are measured are also included. As expected, the applicable scaling range widens with increasing Reynolds number. The exponent μ_3 obtained from the two-point correlator shows a significant increase with the Reynolds number, which is consistent with data trends found in experiments by Mydlarski & Warhaft (1998) but may also be

an effect of moderate Reynolds number in DNS. For the case of highest R_λ (390), the exponents μ_1 and μ_3 obtained from Fig. 4.1(b) and (c) are $0.2 - 0.23$ and $0.17 - 0.21$, which are somewhat less than, but still reasonably close to the mid-range value 0.25 in Sreenivasan *etal.* (1993). Furthermore, it can be seen that μ_1 , μ_2 and μ_3 become closer together at higher R_λ , which is consistent with the development of a wider and better-defined scaling range.

As noted in Sec. 1, the dimensionality of the averaging domain may affect the statistics of the local dissipation ϵ_r . In Fig. 4.2 Comparisons are made for $\langle \epsilon_r^2 \rangle$ obtained by averaging in 1D, 2D and 3D respectively. The data trends seen in parts (a) and (b) of the figure for $R_\lambda \approx 140$ and 390 are quite similar except that the latter exhibits a wider range of scales and stronger intermittency overall. For all values of r the value of $\langle \epsilon_r^2 \rangle$ is found to become smaller with increasing averaging dimensions. This is because, for a given value of r , averaging in two- and three-dimensions involve progressively more grid points in each sample of ϵ_r , such that contributions from highly localized fluctuations are diluted somewhat by lower values of ϵ elsewhere in the domain of averaging. The effect is more pronounced at intermediate values of r , and would be more so if higher-order moments were considered. It appears that the intermittency exponents are slightly larger by three-dimensional averaging than two and one-dimensional averaging, though the dependence is rather weak.

Because of the widespread (and often inevitable) use of the one-dimensional surrogate $\epsilon' = 15\nu(\partial u/\partial x)^2$ in investigations of dissipation intermittency, it is important to determine the nature of differences between results based on ϵ' and ϵ . Some past efforts at resolving this issue include the DNS studies in Chen (1993) and Wang *etal.* (1996), and more recently Cleve *etal.* (2003) which is based on measurements of more than one velocity gradient component in an atmospheric boundary layer. The results in Cleve *etal.* suggest that although the statistics of ϵ and ϵ' differ at the small scales their intermittency exponents are almost the same. Figure 4.3(a,b) show, at two different Reynolds numbers, the normalized two-point correlators of the full energy dissipation, and the squares of longitudinal and transverse velocity gradients. (Note the directions along which r is taken, as stated in the figure captions.) It can be seen that at the small scales, both $(\partial u/\partial x)^2$ and $(\partial u/\partial y)^2$

are more intermittent than ϵ , which can be understood by noting that ϵ is the sum of contributions from both longitudinal and transverse velocity gradients. In the inertial range the normalized two-point correlators of ϵ and $(\partial u/\partial x)^2$ are almost the same, especially at high Reynolds number, which suggests that the use of longitudinal gradients squared as a 1-D surrogate for energy dissipation in inferring intermittency exponents is acceptable. However, it should be noted that the transverse gradient $(\partial u/\partial y)^2$ is more intermittent and has a much shorter scaling range. These results are consistent with Cleve *et al.* (2003).

For completeness, results of two-point correlator for different coordinate components of the velocity gradient squared are also included, which in general can be written as $\langle (\partial u_\alpha/\partial x_\beta)^2(\underline{x})(\partial u_\alpha/\partial x_\beta)^2(\underline{x}+r\mathbf{e}_\gamma) \rangle$, with summation taken over repeated Greek subscripts and normalization based on the mean square of $\partial u_\alpha/\partial x_\beta$. If local isotropy is assumed, then there are five statistically distinct combinations, namely (i) $\alpha = \beta = \gamma$; (ii) $\alpha = \beta \neq \gamma$; (iii) $\alpha \neq \beta, \alpha = \gamma$; (iv) $\alpha \neq \beta, \beta = \gamma$; (v) $\alpha \neq \beta \neq \gamma$. Cases (i) and (iv) correspond to the data in Fig. 4.3. All five combinations are shown in Fig. 4.4, at $R_\lambda \approx 390$. Except for the case of (v), it is found that, as in Fig. 4.3, the differences are mainly significant at the small scales and they tend to become smaller in the inertial range. This suggests the use of one-dimensional surrogates in experiments may give adequate results at sufficient high Reynolds number.

Another indirect method for obtaining the dissipation intermittency exponent is through the sixth-order velocity structure function. It is based on a scaling relation suggested by Frisch *et al.* (1978), namely

$$\langle \epsilon(x)\epsilon(x+r) \rangle \sim \langle (\Delta_r u)^6 \rangle / r^2 \quad (4.9)$$

where $\Delta_r u$ is a longitudinal velocity increment over a distance r in the inertial range. Frisch (1978) noted that this relation may be justified in part by estimates of energy transfer in the inertial range, and that it is satisfied by both the lognormal (Kolmogorov 1962) and the β -models (Frisch *et al.* 1978) of intermittency. Figure 4.5 shows the normalized sixth-order structure function at $R_\lambda \approx 140, 240, \text{ and } 390$. The logarithmic slope shown in the inset illustrates clearly the trend towards a wider scaling range as the Reynolds number

increases. The intermittency exponent inferred from this figure is close to 0.25 (as marked by the dashed line), which is consistent with the values in preceding figures obtained by other means. The utility of Eq. 4.9 is that (despite challenges in sampling) sixth-order velocity structure functions are easier to measure than the full, three-dimensional dissipation rate. However, it has no analog for other flow variables such as enstrophy and scalar dissipation.

Finally, Fig. 4.6(a,b,c) show results for enstrophy $\Omega \equiv \omega^2$ similar as in Fig. 4.1. At small r the highest values seen in these curves compared to those in Fig. 4.1 indicate that enstrophy is more intermittent than dissipation as measured by single-point moments: e.g. $\langle \Omega^2 \rangle / \langle \Omega \rangle^2$ is larger than $\langle \epsilon^2 \rangle / \langle \epsilon \rangle^2$. However, the inertial-range intermittency exponents obtained in Table 4.1 are close to those for the energy dissipation, especially if viewed in terms of μ_2 based on the logarithms of the local averages. The DNS data also support some suggestions in the literature (Nelkin 1999) that the scaling of dissipation and enstrophy become similar in the inertial range at high Reynolds number.

4.3 Intermittency of scalars

In this section, the intermittency of scalar dissipation is studied via the scaling behavior of quantities analogous to those for energy dissipation, namely the logarithmic variance $\sigma_{\ln \chi_r}^2$, the mean-squared box average $\langle \chi_r^2 \rangle$, and the two-point correlator $\langle \chi(x)\chi(x+r) \rangle$. Although many studies of scalar gradient and scalar dissipation statistics (e.g. Antonia & Chambers 1980, Overholt & Pope 1996, Wang, Chen & Brasseur 1999, Vedula, Yeung & Fox 2001) show that the scalar field is more intermittent than the velocity, the value of the scalar dissipation intermittency exponent obtained from the quantities above, and as a function of Schmidt number, is not well determined in the literature. It is necessary to distinguish between two scaling ranges, namely the inertial-convective range at high Reynolds number, and the viscous-convective range at high Schmidt number. Before presenting detailed results for the scalar dissipation, the issue of scalar gradient surrogacy for scalar dissipation, which may be affected by deviations of scalar field from local isotropy, is also reviewed.

A. Scalar gradient surrogacy for scalar gradients

The square of a scalar gradient component is often used as a one-dimensional surrogate for the scalar dissipation although Sreenivasan *etal.* (1977) has pointed out that direct measurement of χ is not as difficult as ϵ since only three separate components are involved. The latter can be defined as $\chi_\alpha = 2D(\partial\phi/\partial x_\alpha)^2$ for $\alpha = 1, 2, 3$, whose characteristics may depend on orientation relative to the direction of the mean scalar gradient in the flow. From the identity $\chi = \sum_{\alpha=1}^3 \chi_\alpha$, it can be written the two-point correlator of χ as the sum of three terms of the form $\langle \chi_\alpha(x)\chi_\alpha(x+r) \rangle$ and six “cross” terms of the form $\langle \chi_\alpha(x)\chi_\beta(x+r) \rangle$ (with $\alpha \neq \beta$).

Figure 4.7(a,b) compare the two-point correlators of the scalar dissipation, where components parallel and perpendicular to the mean gradient are distinguished as χ_{\parallel} and χ_{\perp} , respectively. For χ , average is taken for the two-point correlator over r in three coordinate directions, whereas for χ_{\parallel} and χ_{\perp} , r is chosen in the same direction as the gradient component. To put the results in the context of local isotropy (or deviation therefrom), the following data sets have been chosen: (a) a high R_λ data set at $Sc = 1$ which deviates substantially from local isotropy, and (b) high Sc data sets for which (Yeung *etal.* 2002, 2004) local isotropy holds substantially better. It is clear that the observed differences among χ , χ_{\parallel} and χ_{\perp} for the high Schmidt number case are smaller. As the sum of three intermittent random variables, scalar dissipation χ is expected to be less intermittent than its individual components. This is reflected in the normalized two-point correlators for χ being at lower values than those of χ_{\parallel} and χ_{\perp} in the limit of small r . For values of r slightly larger in the dissipation range the two-point correlators for both χ_{\parallel} and χ_{\perp} decay more rapidly than χ until they become close at values of r much larger than η_B (or η in the case of $Sc = 1$).

Measurements of intermittency exponents for χ and its three component surrogates were previously reported by Sreenivasan *etal.* (1977) for the case of a heated boundary layer, based on $Var(\ln \chi_r)$ with one-dimensional averaging. Figure 4.8(a,b) show the DNS results for $Var(\ln \chi_r)$ (and similar for χ_{\parallel} and χ_{\perp} , with three-dimensional averaging over a cube). As in Fig. 4.7, two data sets have been chosen, one at high Reynolds number, and one at high Schmidt number, with different degrees of departure from local isotropy. The DNS results are consistent with Sreenivasan *etal.* (1977) in indicating stronger intermittency

for the components of χ as seen via larger values of the logarithmic variance at small r . At intermediate values of r the data suggest that use of one-dimensional surrogates may lead to a slight overestimate of the intermittency exponents in the inertial-convective range (in the case of high R_λ) and more so in the viscous-convective range (in the case of high Sc). Comparisons with other data sets (not shown) suggest that high Reynolds number tends to reduce differences in the inertial-convective range. On the other hand, in Fig. 4.8(b), it can be seen that results for χ_{\parallel} and χ_{\perp} at high Schmidt number become almost equivalent, but both possess larger intermittency exponents than the results of χ .

In viewing Fig. 4.7 and 4.8 together it seems that the effects of component surrogacy are manifested in the two-point correlators and logarithmic variances in different ways. This is not fully understood, but may be the result of the same physical processes that contribute to contrasts between results obtained by these two methods as noted elsewhere (Wang, Brasseur & Chen 1999). Also less understood is the effect of the orientation of the spatial separation vector (relative to the mean scalar gradient) on the two-point correlator, which can be generalized as $\langle \chi_\alpha(\mathbf{x})\chi_\alpha(\mathbf{x} + r\mathbf{e}_\beta) \rangle$. In the configuration of the simulations four distinct combinations of the set $\{\alpha, \beta\}$ are possible, with the situation becoming more complex yet in anisotropic turbulence where preferred orientations in the mean velocity field will also have an effect.

B. Reynolds number effects in inertial-convective range

The primary requirement for an inertial-convective range is sufficiently high Reynolds number. Fig. 4.9(a,b,c) show the functions $\sigma_{\ln \chi_r}^2$, $\langle \chi_r^2 \rangle$ and $\langle \chi(x)\chi(x+r) \rangle$ at $Sc = 1$ for the three highest Reynolds numbers ($R_\lambda \approx 140, 240$ and 390) in the simulations. Compared to results for energy dissipation in Fig. 4.1, stronger intermittency in the scalar field compared to the velocity is indicated by larger values of these normalized functions at the small scales, and by steeper negative slopes at intermediate scales. However, since the slopes of these curves are more sensitive to the choice of scaling range, great care is needed in order to obtain reliable values of the intermittency exponents. A range of r is chosen such that it best approximates the so-called Yaglom relation for the mixed velocity-scalar

third-order structure function, i.e. $\langle \Delta_r u (\Delta_r \phi)^2 \rangle = -(2/3) \langle \chi \rangle r$ for $\{\eta, \eta_{OC}\} \ll r \ll L$. The scaling range available in the simulations is limited by the Reynolds number, and inherently narrower for scalars with $Sc < 1$ for which $\eta_{OC} > \eta$. Additional ambiguities may also arise due to deviations from local isotropy, although this is in part alleviated by averaging results for r in three coordinate directions.

With the caveats noted above, the best estimates for the scalar dissipation intermittency exponents are given in Table 4.3, for scalars with $Sc = 1/8$ and $Sc = 1$. As expected from standard arguments, an increase in Reynolds number gives a wider scaling range which is also shifted towards scales increasingly large compared to η . Because the scalar statistics scale with η_{OC} for $Sc \leq 1$ an increase in Sc from $1/8$ to 1 produces the opposite trend (towards smaller r/η) as η_{OC} becomes smaller. The results agree with Wang *etal.* (1999) that the variance of the logarithm gives systematically larger values of the intermittency exponent. Larger intermittency exponents reflecting stronger intermittency are also expected at higher Reynolds and Schmidt numbers (at least when $Sc = O(1)$). However, the data in Table 4.3 do not reveal a systematic trend, presumably because the effect is weak and easily masked by uncertainties inherent in the tasks of choosing a precise scaling range and measuring the slopes of curves. Nevertheless, exponents obtained for both $\langle \chi_r^2 \rangle$ and $\langle \chi(x)\chi(x+r) \rangle$ are within the range 0.3-0.4, which is in reasonable agreement with both 0.38-0.46 in Sreenivasan *etal.* (1977) and 0.2-0.3 by Mydlarski & Warhaft (1998) in grid turbulence experiments.

Although the Reynolds number is the main parameter of concern in studies of the inertial-convective range, understanding of Schmidt number effects is also important. Figure 4.10 compares normalized two-point correlators of the scalar dissipation at $Sc = 1/8$ and $Sc = 1$ obtained from the $R_\lambda \approx 390$ simulation. In parts (a) and (b) of this figure, the distance r has been expressed in Kolmogorov and Obukhov-Corrsin scaling, respectively. In the limit $r \rightarrow 0$ the function shown should approach the ratio $\langle \chi^2 \rangle / \langle \chi \rangle^2$, which is (see Table 4.3) larger for $Sc = 1$ than for $Sc = 1/8$. This is not obvious from (a), where the normalized two-point correlator appears to be larger for $Sc = 1/8$ at fixed r , and results for $Sc = 1$ do not show a clear trend towards the small r asymptote. These features arise

because the Kolmogorov scale does not (except for $Sc = 1$) represent the size of the small scales in the scalar field, and because the grid spacing is not sufficiently fine to fully resolve the small-scale content of the scalar dissipation fluctuations. (A critical discussion of local resolution requirements is given recently by Sreenivasan 2004.) The Schmidt number scaling is much clearer in (b) where η_{OC} is used as the normalizing scale instead. In this modified scaling the normalized two-point correlators at $Sc = 1/8$ and $Sc = 1$ are seen to be very similar in shape. However a comparison of the respective intermittency exponents is still very sensitive to the chosen scaling range.

C. Schmidt number effects in viscous-convective range

Recent studies of high-Schmidt-number mixing using DNS have provided direct evidence that although both increasing R_λ and Sc produce a wider range of scales in the scalar field, their effects are very different in nature. In particular, Yeung *et al.* (2002, 2004) showed that high Schmidt number causes a return towards local isotropy and a saturation of intermittency while the value of Sc needed for the asymptotic behavior to emerge appears to decrease with Reynolds number. Schmidt number effects are discussed in the context of dissipation statistics in the viscous-convective range: i.e., for length scales r such that $\eta_B < r < \eta$.

Fig. 4.11(a,b,c) shows the functions $\text{Var}(\ln \chi_r)$, $\langle \chi_r^2 \rangle$ and $\langle \chi(x)\chi(x+r) \rangle$ for a range of Schmidt numbers (1 to 64) at fixed R_λ (38), with scale size r normalized by η_B . At the smaller scales (say $r < 10\eta_B$) data trends are not very well defined in $\text{Var}(\ln \chi_r)$. However, for the other two quantities it is apparent that except for $Sc = 1$ the differences between curves for different Schmidt numbers are small at small r . In other words, the Schmidt number dependence becomes diminished at high Sc , which is consistent with a trend towards saturation of intermittency in single-point statistics in the high Schmidt number limit. It is found that most curves display a scaling range roughly between $2\eta_B$ and 2η , with a steeper slope than in the intermediate scales (say beyond $10\eta_B$) where all curves fall more slowly at increasing Schmidt numbers.

Intermittency exponents for the viscous-convective range obtained from the data in

Fig. 4.11 are shown in Table 4.4. In order to illustrate possible effects of inadequate resolution at the small scales, data have been included for $Sc = 16$ from two simulations at 256^3 and 512^3 resolution, respectively. (Only the latter, which is believed to be more accurate, is actually shown in Fig. 4.11.) The comparison suggests that a degree of resolution of $k_{max}\eta_B = 1.5$ (at 256^3) may not be sufficient and can lead to underestimation of intermittency. (This effect is similar to that for the flatness factor of intermittent signals in space, where insufficient resolution can be considered as a local smoothing which causes some extreme fluctuations not fully captured.) With this limitation considered (and presumably applicable also to the $Sc = 64$ case at the bottom of the Table), it can be said that there are systematic trends in Schmidt number overall. The exponent obtained from the two-point correlator decreases with Sc , which is qualitatively consistent with experimental data by Sreenivasan & Prasad (1989). At higher Schmidt numbers it seems that these two exponents agree more closely with each other, which may be an indication of the attainment of a better-defined scaling range. Differences in the behavior of this scaling exponent from the others remain to be understood although they have been reported before (e.g. Wang, Brasseur & Chen 1999, figures 11 and 12 therein).

An inherent limitation in the results of Fig. 4.11 and Table 4.4 for Sc up to 64 is that the viscous-convective range is not well-defined because of relatively small η/η_B . This consideration provided the motivation for simulations of even higher Sc of up to 1024 (Yeung *et al.* 2004) albeit at even lower Reynolds number, namely $R_\lambda \approx 8$. Fig. 4.12 shows the results, scaled in the same manner as in Fig. 4.11, with corresponding scaling exponents shown in Table 4.5. For reasons similar to those noted in the discussion of Table 4.3, data at $Sc = 64$ and 256 on 128^3 and 256^3 grids respectively are regarded as less accurate and hence omitted from Fig. 4.12. Figure 4.13 shows the intermittency exponents for high Schmidt numbers at $R_\lambda \approx 38$ and $R_\lambda \approx 8$. The data are based on Table 4.4 and 4.5 and average value is taken whenever applicable. The intermittency exponent μ_3 obtained from the two-point correlator decreases with Sc and it is almost independent of R_λ at small Sc . Exponent μ_1 for $\langle \chi_r^2 \rangle$ slightly decreases with Sc for $Sc \geq 32$. The data show that μ_1 is generally smaller than μ_3 , but μ_1 and μ_3 become closer at high Sc . It is noted that the calculated μ_1 at

small Sc is subject to uncertainty arising from the low resolution and fewer data points in viscous-convective range available for the purpose of exponent calculation. The inset of Fig. 4.13 shows μ_2 for $Var(\ln \chi_r)$. The results suggest that μ_2 is normally larger than μ_1 and μ_3 but also tends to be independent of Sc at high Sc . These various intermittency exponents suggest that intermittency shows no increasing trend in viscous-convective range at high Sc .

In this chapter, scalings of energy dissipation, enstrophy and scalar dissipation have been studied based on the DNS data sets for Reynolds number up to $R_\lambda \approx 390$ and Sc up to 1024. Various intermittency exponents have been calculated, including those indicated by $\langle Y(x)Y(x+r) \rangle$, $\langle Y_r^2 \rangle$ and $Var(\ln Y_r)$, where Y represents particularly energy dissipation, scalar dissipation and enstrophy. It is found that the velocity intermittency exponents in inertial range increase with Reynolds number, and has the value of about 0.2 in the highest Reynolds number case of $R_\lambda \approx 390$. This value is reasonably close to 0.25 cited in Sreenivasan *et al.* (1993). It is possible that the intermittency exponent becomes closer to 0.25 for even high Reynolds number. The velocity intermittency exponents μ_1 , μ_2 and μ_3 become closer at high Reynolds number. In calculation of $\langle Y_r^2 \rangle$, averaging over three dimensions gives slightly larger value of intermittency exponent than averaging in one dimension. Scalar intermittency exponents in the inertial-convective range are larger than those of velocity field, suggesting that the scalar field is more intermittent than the velocity field. In the viscous-convective range, scalar intermittency exponents tend to have a weak dependence on Sc in the limit of high Schmidt number. The intermittency exponents μ_1 and μ_3 become closer at high Sc , however, μ_2 is significantly larger than μ_1 and μ_3 .

Table 4.1: Intermittency exponents for energy dissipation and enstrophy

Statistics	$R_\lambda 140$	$R_\lambda 240$	$R_\lambda 390$
Grid	256^3	512^3	1024^3
$\langle \epsilon \rangle$	1.2	1.25	1.3
$\langle \epsilon^2 \rangle / \langle \epsilon \rangle^2$	1.8	2.8	3.7
L/η	98	195	442
measure range	$(31-65)\eta$	$(47-100)\eta$	$(45-125)\eta$
$\langle \epsilon_r^2 \rangle$	0.17	0.16-0.21	0.2-0.23
$\sigma_{\ln \epsilon_r}^2$	0.17	0.17-0.22	0.2-0.24
$\langle \epsilon(x)\epsilon(x+r) \rangle$	0.09-0.17	0.12-0.18	0.17-0.21
$\langle \Omega_r^2 \rangle$	0.21	0.17-0.22	0.22-0.29
$\sigma_{\ln \Omega_r}^2$	0.23	0.18-0.29	0.22-0.32
$\langle \Omega(x)\Omega(x+r) \rangle$	0.09-0.18	0.12-0.19	0.17-0.23
$\langle (\Delta u)^6 \rangle / r^2$	0.2-0.3	0.2-0.28	0.21-0.28
	$(60-71)\eta$	$(92-122)\eta$	$(80-170)\eta$

Table 4.2: Intermittency exponents for scalar dissipation at higher Reynolds numbers

R_λ	Grid	Sc	Range	$\langle \chi(x)\chi(x+r) \rangle$	$\langle \chi_r^2 \rangle$	$\sigma_{\ln \chi_r}^2$
140	256^3	1/8	$(29-57)\eta$	0.31-0.45	0.45-0.51	0.65-0.70
140	256^3	1	$(17-31)\eta$	0.29-0.41	0.42	0.63
240	512^3	1/8	$(45-85)\eta$	0.41-0.47	0.45-0.51	0.7-0.82
240	512^3	1	$(19-51)\eta$	0.31-0.47	0.40-0.50	0.57-0.7
390	1024^3	1/8	$(76-128)\eta$	0.42-0.48	0.48	0.78
390	1024^3	1	$(41-93)\eta$	0.33-0.36	0.34-0.39	0.52-0.61

Table 4.3: Intermittency exponents for scalar dissipation at $R_\lambda \approx 38$

R_λ	Grid	Sc	Range	$\langle \chi(x)\chi(x+r) \rangle$	$\langle \chi_r^2 \rangle$	$\sigma_{\ln \chi_r}^2$
38	256^3	4	$2\eta_B - 2\eta$	0.56-0.6	0.4	0.59
38	256^3	8	$2.8\eta_B - 2\eta$	0.52-0.56	0.37	0.69
38	256^3	16	$4\eta_B - 2\eta$	0.47-0.52	0.38	0.64
38	512^3	16	$2\eta_B - 2\eta$	0.51-0.57	0.37-0.45	0.61-0.82
38	512^3	32	$2.8\eta_B - 2\eta$	0.47-0.51	0.35-0.43	0.68-0.85
38	512^3	64	$4\eta_B - 2\eta$	0.43-0.46	0.35-0.39	0.61-0.72

Table 4.4: Intermittency exponents for scalar dissipation at $R_\lambda \approx 8$

R_λ	Grid	Sc	Range	$\langle \chi(x)\chi(x+r) \rangle$	$\langle \chi_r^2 \rangle$	$\sigma_{\ln \chi_r}^2$
8	128^3	4	$\eta_B - \eta$	0.58	0.2	0.37
8	128^3	8	$1.4\eta_B - \eta$	0.57	0.28	0.47
8	128^3	16	$2\eta_B - \eta$	0.47-0.52	0.35	0.59
8	128^3	32	$2.8\eta_B - \eta$	0.46-0.49	0.37	0.66
8	128^3	64	$4\eta_B - \eta$	0.43	0.35	0.62
8	256^3	64	$2\eta_B - 2\eta$	0.44-0.55	0.34-0.42	0.61-0.76
8	256^3	128	$2.8\eta_B - 2\eta$	0.41-0.50	0.34-0.38	0.68-0.77
8	256^3	256	$4\eta_B - 2\eta$	0.37-0.40	0.33-0.35	0.57-0.66
8	512^3	256	$2.4\eta_B - \eta$	0.39-0.48	0.33-0.38	0.65-0.79
8	512^3	512	$3.4\eta_B - \eta$	0.35-0.45	0.32-0.35	0.71-0.79
8	512^3	1024	$4.8\eta_B - \eta$	0.30-0.40	0.31-0.32	0.60-0.67

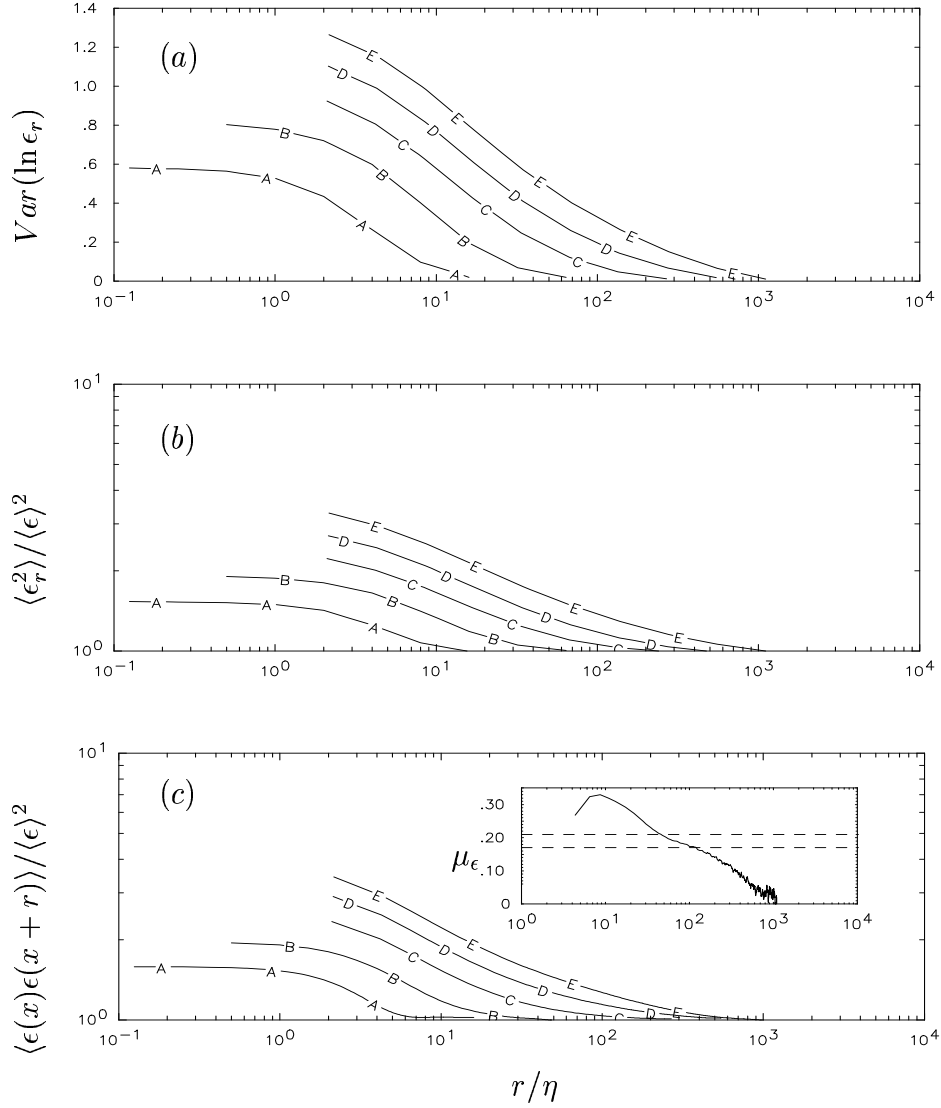


FIG. 4.1 The functions (a) $Var(\ln \epsilon_r)$, (b) $\langle \epsilon_r^2 \rangle / \langle \epsilon \rangle^2$, and (c) $\langle \epsilon(x)\epsilon(x+r) \rangle / \langle \epsilon \rangle^2$ used to infer intermittency exponents for the energy dissipation. Lines A-E represent results at Taylor-scale Reynolds numbers $R_\lambda \approx 8$ (on 256^3 grid), 38 (256^3), 140 (256^3), 240 (512^3), and 390 (1024^3), respectively. Inset in (c) shows use of slope of line E to evaluate the exponent μ_3 at $R_\lambda \approx 390$. Dashed lines are at 0.17 and 0.21, respectively.

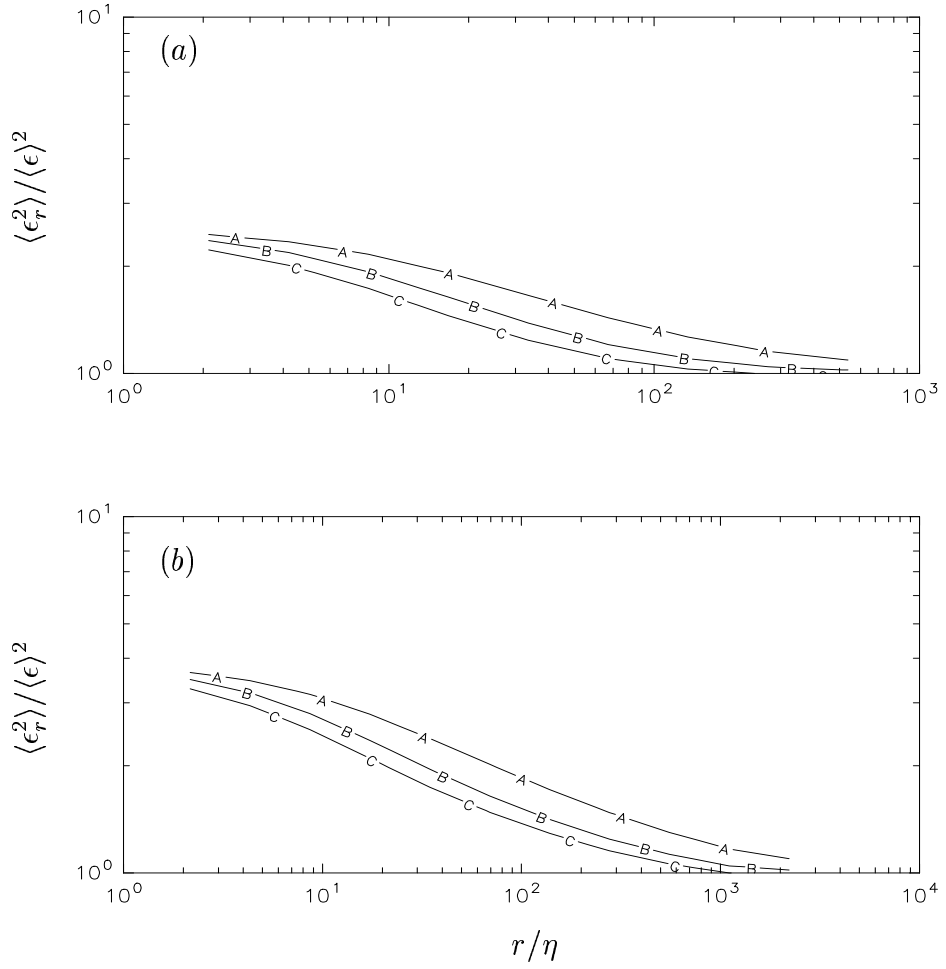


FIG. 4.2. Comparison of the mean-squared local energy dissipation $\langle \epsilon_r^2 \rangle / \langle \epsilon \rangle^2$, at (a) R_λ 140, (b) R_λ 390, for averages taken in one, two- and three-dimensions respectively (lines A-C).

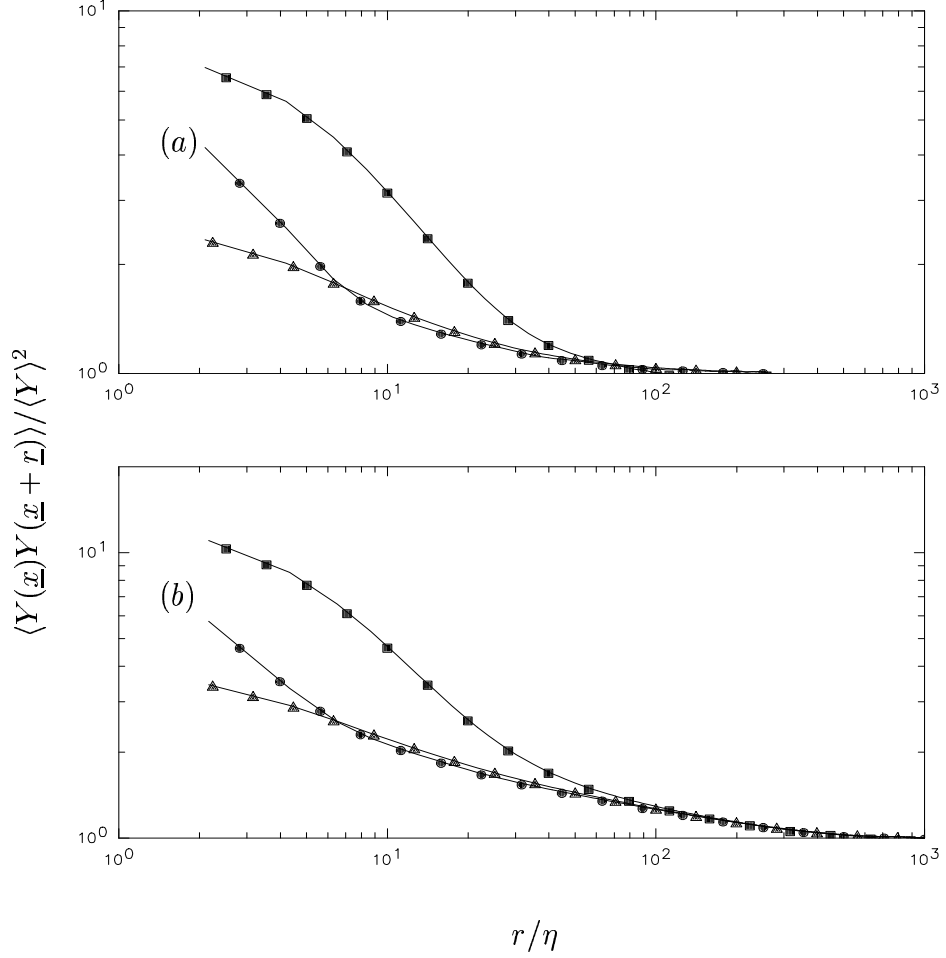


FIG. 4.3. Comparisons of two-point correlators of energy dissipation and its one-dimensional surrogates at (a) R_λ 140, (b) R_λ 390. Triangles for full 3-D dissipation ($Y = \epsilon$) averaged over distance r in three directions; circles for longitudinal velocity with longitudinal separation distance (e.g. $Y = (\partial u_1/\partial x_1)^2$ with $\underline{r} = r\mathbf{e}_1$), squares for transverse velocity with transverse separation distance (e.g. $Y = (\partial u_1/\partial x_2)^2$ with $\underline{r} = r\mathbf{e}_3$).

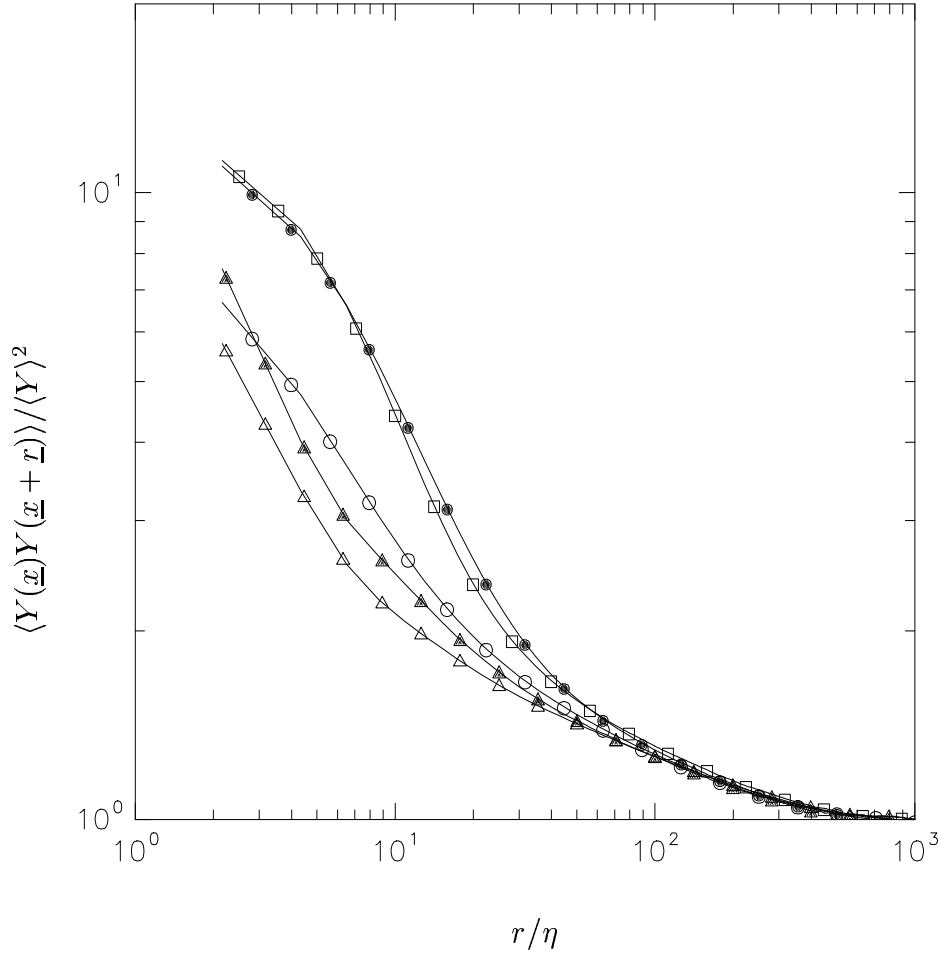


FIG. 4.4. Comparisons of two-point correlators of different velocity gradients squared $(\partial u_\alpha / \partial x_\beta)^2$, with distance r taken along the axis x_γ . Open triangle: $\alpha = \beta = \gamma$, open circle: $\alpha = \beta \neq \gamma$, open square: $\alpha = \gamma \neq \beta$, close triangle: $\alpha \neq \beta = \gamma$, close circle: $\alpha \neq \beta \neq \gamma$.

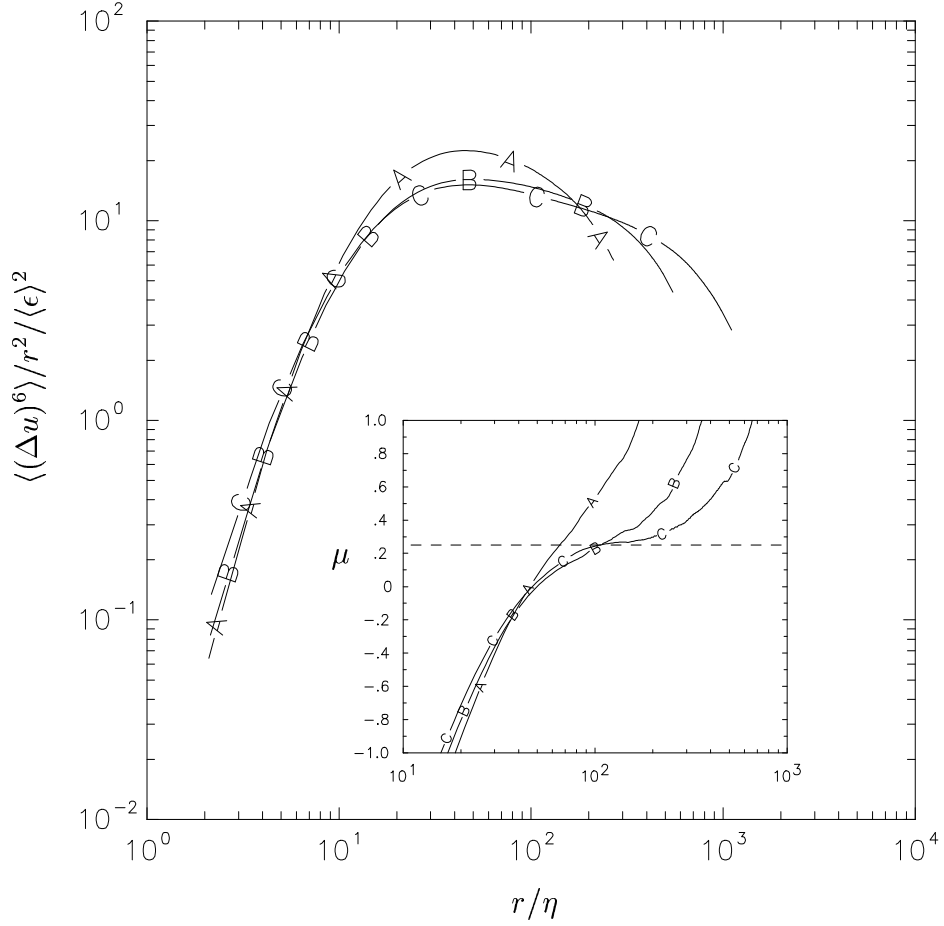


FIG. 4.5. Normalized sixth-order longitudinal velocity structure function. $R_\lambda \approx 140, 240$ and 390 (lines A-C respectively). The inset shows the slopes of the curves, with a dashed line corresponding to an intermittency exponent 0.25 for reference.

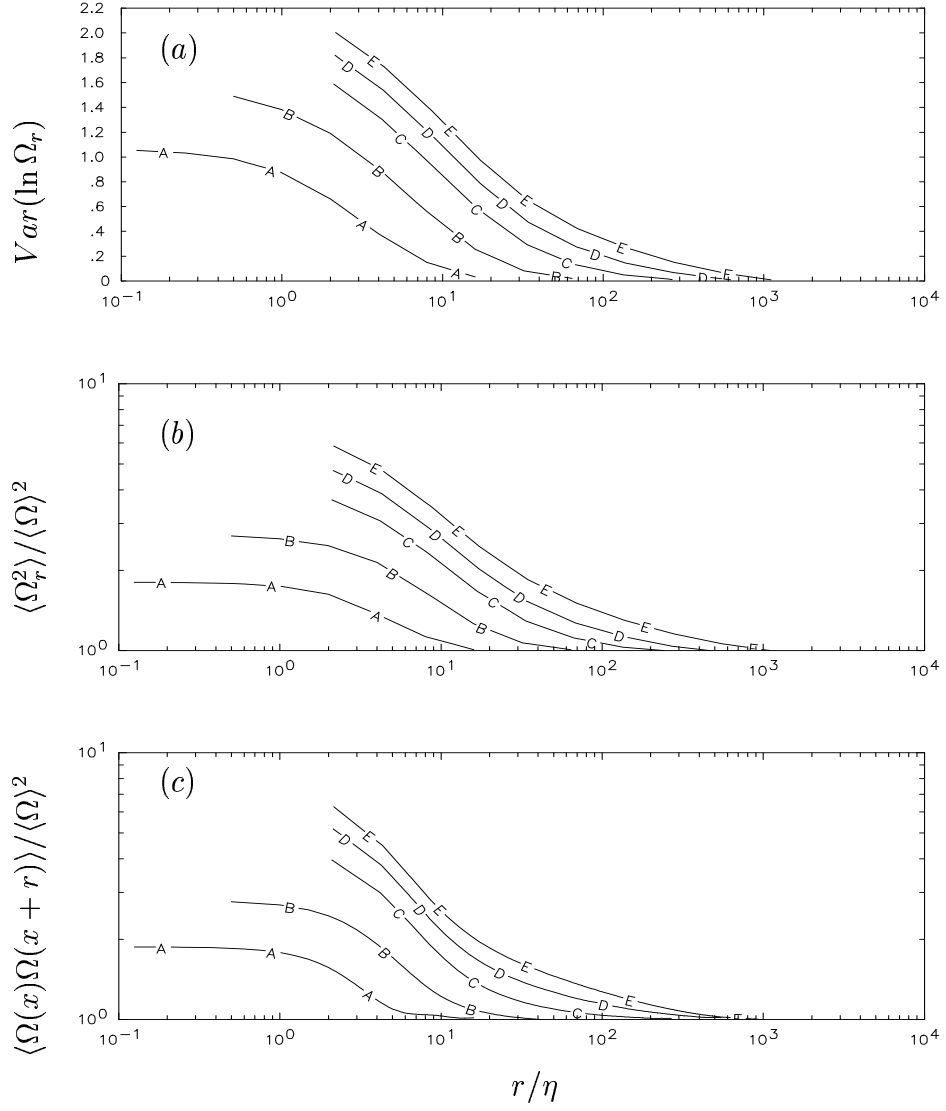


FIG. 4.6(a,b,c). Same as Fig. 4.1(a,b,c), but for the enstrophy ($\Omega = \omega_i \omega_i$).

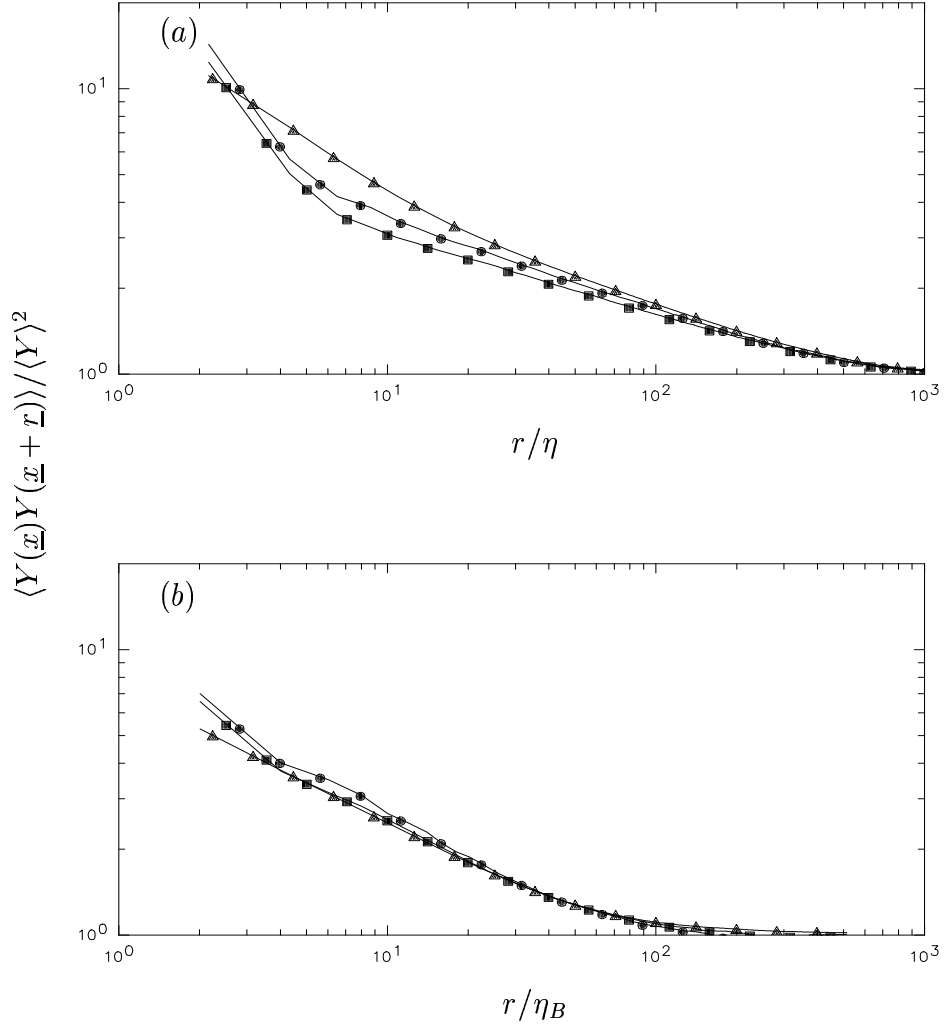


FIG. 4.7 Comparisons of two-point correlators of scalar dissipation and its scalar gradient surrogates for (a) $R_{\lambda} \approx 390$, $Sc = 1$ and (b) $R_{\lambda} \approx 38$, $Sc = 64$. Triangles for full scalar dissipation (χ) averaged over distance r in three directions; circles and squares for components parallel (χ_{\parallel}) and perpendicular (χ_{\perp}) to direction of mean gradient respectively.

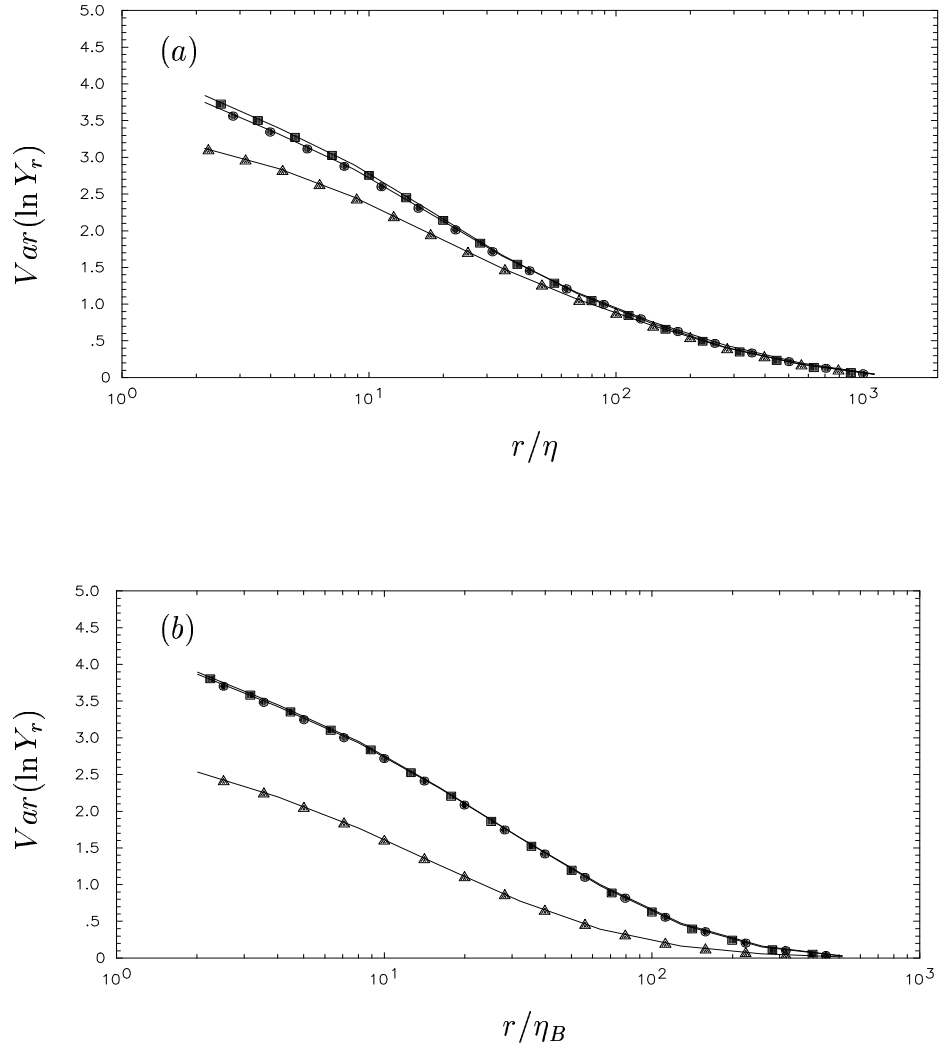


FIG. 4.8. Same as Fig. 4.7, but for local averages taken over three-dimensional boxes of length r on each side.

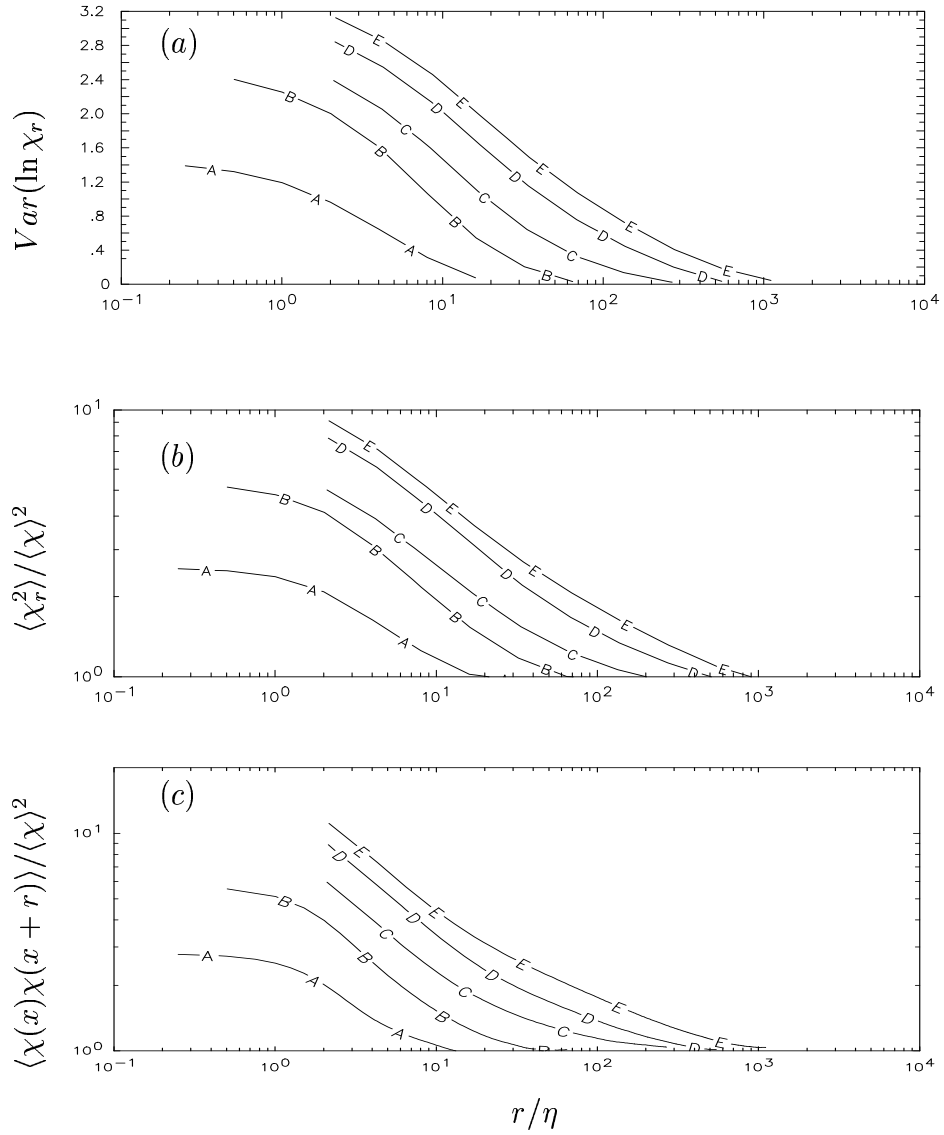


FIG. 4.9(a,b,c). Same as Fig. 4.1(a,b,c), but for scalar dissipation at $Sc = 1$ for the same Reynolds numbers.

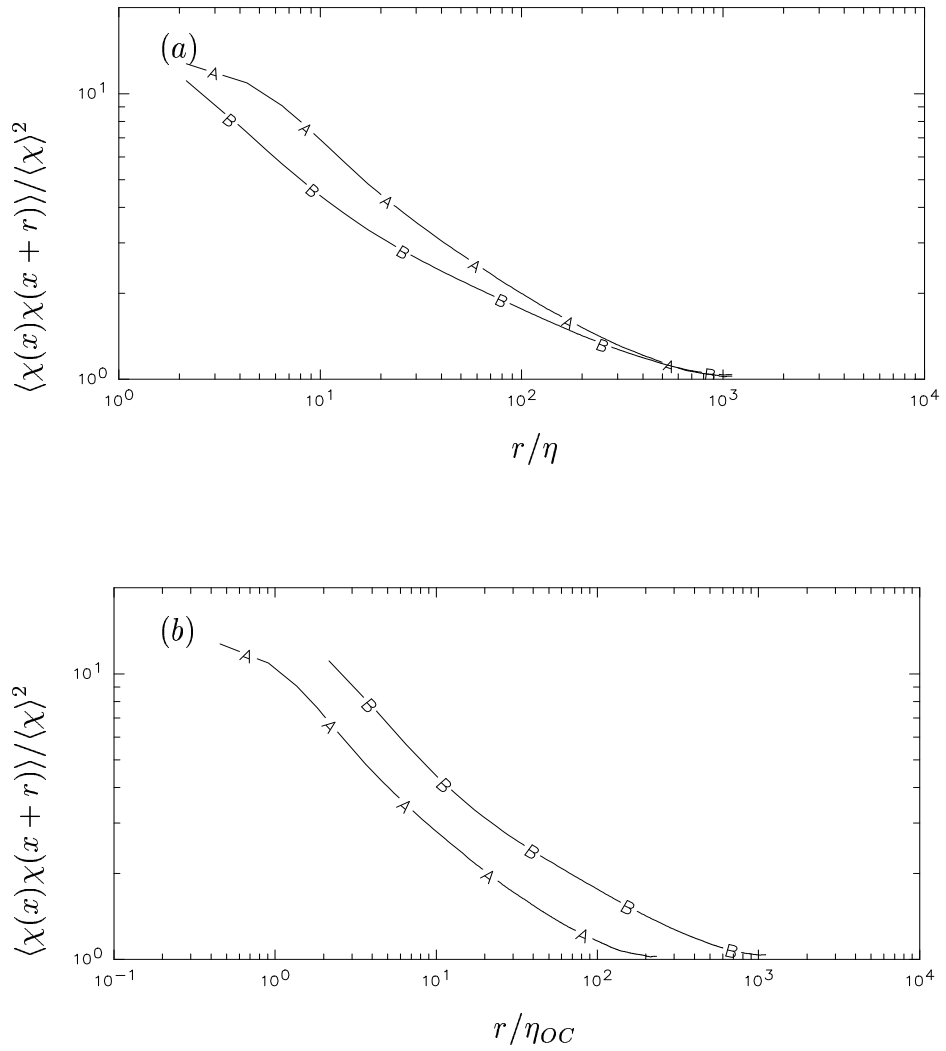


FIG. 4.10. Comparison of two-point correlators for scalar dissipation at $Sc = 1/8$ and 1 (lines A and B) $R_\lambda = 390$, with distance r normalized by (a) Kolmogorov scale and (b) Obukhov-Corrsin scale.

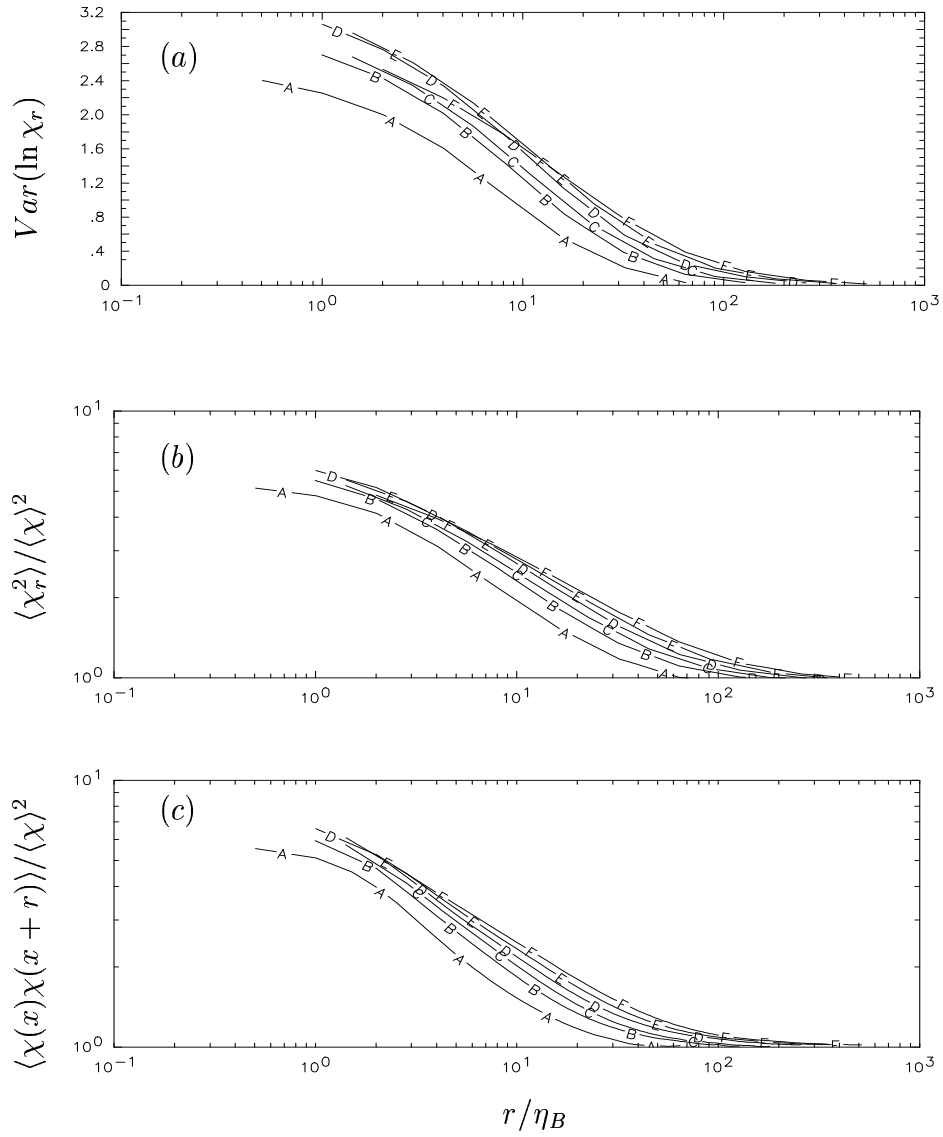


FIG. 4.11(a,b,c). Same as Fig. 4.1(a,b,c), but for scalar dissipation at R_λ 38, for Schmidt numbers $Sc = 1, 4, 8$ (lines A-C, 256^3) and $16, 32, 64$ (lines D-F, 512^3).

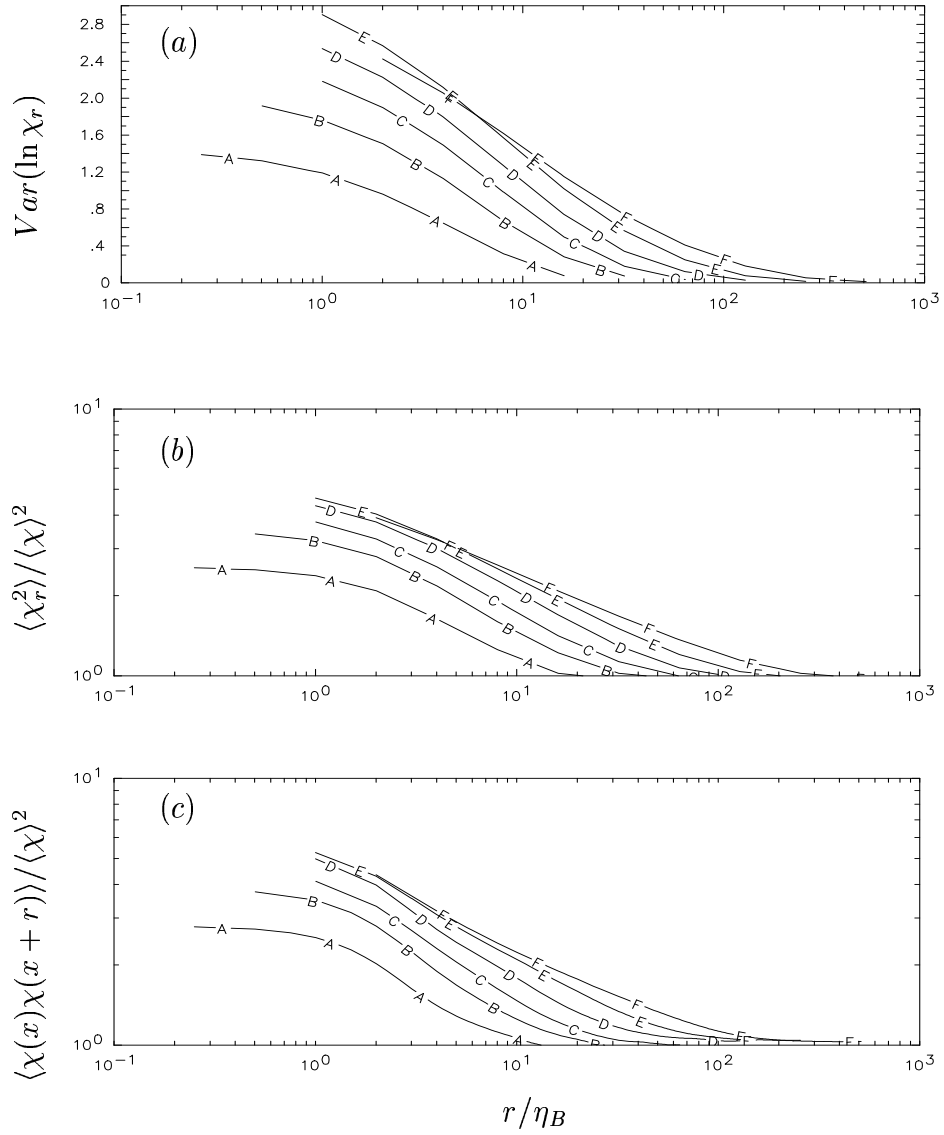


FIG. 4.12(a,b,c). Same as Fig. 4.11(a,b,c), but at $R_\lambda 8$, for $Sc = 1, 4, 16$ (lines A-C, 128^3), 64 (line D, 256^3), and 256,1024 (lines E-F, 512^3).

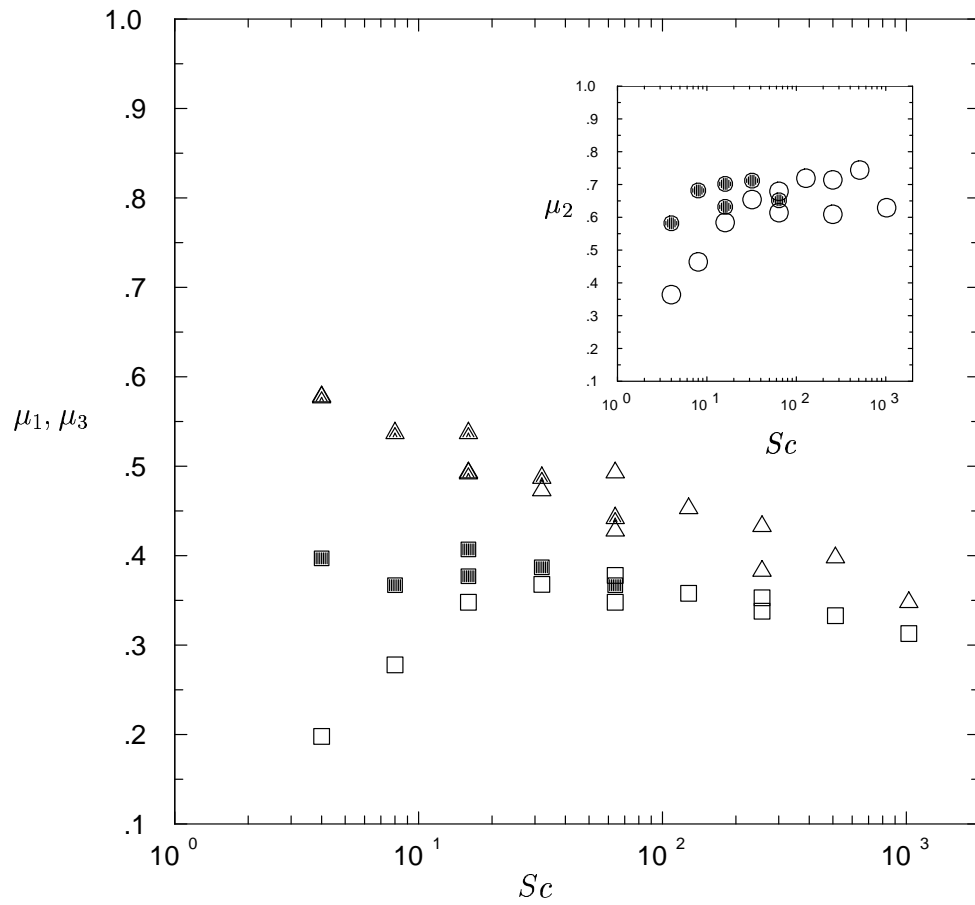


FIG. 4.13 Intermittency exponents as a function of Sc : closed symbols at $R_\lambda \approx 38$, open symbols at $R_\lambda \approx 8$; squares (μ_1), circles (μ_2), triangles (μ_3).

CHAPTER V

DIFFERENTIAL DIFFUSION AND SCALAR SPECTRAL TRANSFER

In this chapter of the thesis, basic properties of differential diffusion between weakly diffusive scalars are discussed. The later part of the chapter describes single scalar spectral transfer and subgrid transfer for a given cut-off wavenumber k_c . The work in this chapter may be considered as an extension of previous work at $Sc = 1$ or less (Yeung, 1996, 1998, Yeung and Zhou 1996) to the high Sc regime.

5.1 *Differential diffusion*

In this section, high- Sc DNS data are examined on basic statistical quantities involving two scalars ϕ_α and ϕ_β with different molecular diffusivity D_α and D_β advected by the same turbulent flows. The two scalars have zero fluctuations at time $t = 0$ and they evolve according to the scalar transport equation Eq. 2.3. A fundamental statistic that characterizes differential diffusion between ϕ_α and ϕ_β is the correlation coefficient $\rho_{\alpha\beta}$ defined as

$$\rho_{\alpha\beta} = \frac{\langle \phi_\alpha \phi_\beta \rangle}{\langle \phi_\alpha^2 \rangle^{1/2} \langle \phi_\beta^2 \rangle^{1/2}}. \quad (5.1)$$

Figure 5.1 shows the evolution of the correlation coefficient $\rho_{\alpha\beta}$ at $R_\lambda \approx 38$ and $R_\lambda \approx 8$ for scalar pairs with different Schmidt numbers. The coefficient $\rho_{\alpha\beta}$ starts from 1 at time $t = 0$ when the two scalars both have zero fluctuations. Subsequently, the two scalars begin to evolve differently as a result of difference in their respective molecular diffusivities and therefore, they become less perfectly correlated. Ultimately, $\rho_{\alpha\beta}$ tends to a stationary level as the turbulent fluctuations become stationary. Fig. 5.1(a) and (b) show correlation coefficients for scalar pairs with Sc ratio 2 and 4 at $R_\lambda \approx 38$ and $R_\lambda \approx 8$, respectively. Scalar pairs in Fig. 5.1(a) are combinations of scalars with $Sc = \{16, 32, 64\}$ and those in Fig. 5.1(b) are from $Sc = \{256, 512, 1024\}$. It can be seen that the level of $\rho_{\alpha\beta}$ in stationary

state for both (a) and (b) is very close to each other for scalar pair with the same Sc ratio. This suggests that at high Schmidt numbers, the scalar correlation coefficient mainly depends on the Sc ratio between the two scalars and its dependence on Reynolds number is rather weak, whereas in Yeung (1998), it is found that for low Sc ($= 1/8, 1$), scalars tend to be more correlated at higher Reynolds number. Fig. 5.1(c) shows $\rho_{\alpha\beta}$ for scalars with larger Sc ratios of 8 and 64 from combinations of $Sc = \{1, 8, 64\}$. It can be seen that larger Sc ratio tends to de-correlate scalar fluctuations further because scalars with large Sc ratio have more disparate scales. It is also noticed in Fig. 5.1(b) that scalar pairs with the same Sc ratio but have different magnitude of Sc 's (line A for $Sc = \{1, 8\}$ and B for $Sc = \{8, 64\}$) have considerable difference compared with Sc ratio of 2 in (a) and (c). Overall, Fig. 5.1 suggests that the asymptotic value of the correlation coefficient between two scalars at high Sc 's mainly depends on the Sc ratio and large Sc ratios tend to de-correlate scalar pair. For large Sc ratio, $\rho_{\alpha\beta}$ tends to be more correlated for scalar pairs with Sc 's of larger magnitude, but for smaller Sc ratio, the magnitude of the Sc 's of the scalar pair has little effect on the correlation coefficient.

Also of interest here is the correlation of scalars at smaller scales, which can be quantified by the correlation coefficient of scalar gradient between two scalars, i.e.,

$$g_{\alpha\beta} = \frac{\langle \frac{\partial\phi_\alpha}{\partial x_i} \frac{\partial\phi_\beta}{\partial x_i} \rangle}{((\langle \frac{\partial\phi_\alpha}{\partial x_i} \rangle^2) \langle \frac{\partial\phi_\beta}{\partial x_i} \rangle^2)^{1/2}}, \quad (5.2)$$

where x_i can be any of the three Cartesian coordinates. Yeung (1998), Fox (1999) and Chakravarthy & Menon (2001) derived a model estimate for $g_{\alpha\beta}$ based on a local isotropy assumption for the ‘‘joint dissipation’’ $\chi_{\alpha\beta} \equiv (D_\alpha + D_\beta) \langle (\partial\phi_\alpha/\partial x_i)(\partial\phi_\beta/\partial x_i) \rangle$, where the large time limit is

$$g_{\alpha\beta} \approx 2 \left(\frac{D_\alpha}{D_\beta} + \frac{D_\beta}{D_\alpha} + 2 \right)^{-1/2}. \quad (5.3)$$

Equation 5.3 indicates that the large time limit of $g_{\alpha\beta}$ is only a function of the ratio of molecular diffusivities and is independent of the large scale parameter of Reynolds number. Figure 5.2 show correlation coefficient of scalar gradients in the direction of mean scalar gradient for various Sc -ratio and Reynolds number combinations. Dotted line represents the large time limit given by Eq. 5.3. Indeed, the stationary state $g_{\alpha\beta}$ agrees with the

estimate of Eq. 5.3 for Sc ratio (hence the ratio of molecular diffusivities) from 2 to 64 in Fig. 5.2. In contrast with scalar correlation coefficient $\rho_{\alpha\beta}$ in Fig. 5.1(b), $g_{\alpha\beta}$ for $Sc = \{1, 8\}$ and $\{8, 64\}$ does not show systematic difference. For $Sc = \{1, 64\}$, $g_{\alpha\beta}$ reaches 0.25 at large times. It is expected for $D_\alpha/D_\beta \rightarrow \infty$, $g_{\alpha\beta}$ will tend to zero. Figure 5.2(c) shows for $g_{\alpha\beta}$ at $R_\lambda \approx 140, 240$ and 390 for $Sc = \{1/8, 1\}$, and the result suggests that large time limit of $g_{\alpha\beta}$ does not depend on Reynolds number, which is consistent with the small scale universality of K41 theory. In contrast, the larger scale correlation coefficient $\rho_{\alpha\beta}$ increases with Reynolds number (Yeung 1998). The results suggest that high Reynolds number tends to reduce differential diffusion at relatively large scales, but differential diffusion remains important at the small scales. It is also worth noting that differences among $g_{\alpha\beta}$ in the three coordinate directions are negligible suggesting that local isotropy is a good approximation for Eq. 5.3. Figure 5.2 at high Schmidt numbers and various Reynolds number agrees very well with the model prediction of Eq.5.3.

The scale dependency of the correlation between two scalars can be represented by the coherency spectrum, defined as

$$\rho_{\alpha\beta}(k) \equiv \frac{E_{\alpha\beta}(k)}{[E_{\alpha\alpha}(k)E_{\beta\beta}(k)]^{1/2}}, \quad (5.4)$$

where $E_{\alpha\beta}(k) \equiv 1/2(\hat{\phi}_\alpha \hat{\phi}_\beta^* + \hat{\phi}_\alpha^* \hat{\phi}_\beta)$ is the co-spectrum between ϕ_α and ϕ_β , where “hat” denotes the corresponding Fourier transform and “asterisk” the complex conjugate. $E_{\alpha\alpha}$ and $E_{\beta\beta}$ are scalar spectrum ($\equiv \langle \hat{\phi} \hat{\phi}^* \rangle$). Equation 5.4 suggests that the coherency is essentially a correlation coefficient in Fourier space, which conveys the information of scalar correlation at different scales. Figure 5.3 shows the coherency spectrum as a function of wavenumber normalized by the Batchelor scale η_B of the less diffusive scalar based on the data sets for high Sc 's at $R_\lambda \approx 38$ and $R_\lambda \approx 8$. In Fig. 5.3, $\rho_{\alpha\beta}$ shows a rough “collapse” among data from intermediate to small scales according to Sc ratios ($D_\alpha/D_\beta = 2, 4, 8, 64$) and there is little differential diffusion at large scales. It can be seen that stronger differential diffusion occurs for larger Sc ratio, which is the major factor affecting differential diffusion at high Sc 's. The magnitude of Schmidt numbers and Reynolds number plays minor role in coherency spectrum at high Sc 's.

The correlation between two scalars as a function of scale size can also be characterized in wavenumber space, where at each fixed wavenumber vector \mathbf{k} , the following can be computed

$$r_{\alpha\beta}(\mathbf{k}) \equiv \frac{\frac{1}{2}(\hat{\phi}_\alpha \hat{\phi}_\beta^* + \hat{\phi}_\alpha^* \hat{\phi}_\beta)}{|\hat{\phi}_\alpha| |\hat{\phi}_\beta|} = \cos[\theta_\alpha(\mathbf{k}) - \theta_\beta(\mathbf{k})], \quad (5.5)$$

with θ_α and θ_β being the phase angles of $\hat{\phi}_\alpha(\mathbf{k})$ and $\hat{\phi}_\beta(\mathbf{k})$ in the complex plane. Hence, the spectral coherency between two scalars can be interpreted as their phase alignment in Fourier space. Fig. 5.4 shows the probability density function (PDF) of the phase angle difference between two scalars for Schmidt number ratio 2, 4, 8 and 64. It can be seen that the PDFs tend to be flatter at high wave numbers and for high Sc ratio scalar pair, which suggests that scalars are more uncorrelated at small scales and for high Sc ratios. This is consistent with the trend for coherency spectrum in Fig. 5.3.

A direct measure of differential diffusion at different scales is the spectrum of the difference between two scalars, defined as

$$F_{\alpha\beta}(k) \equiv E_{\alpha\alpha}(k) - 2E_{\alpha\beta}(k) + E_{\beta\beta}(k), \quad (5.6)$$

where we have $\int_k F_{\alpha\beta}(k) dk = \langle (\phi_\alpha - \phi_\beta)^2 \rangle$. Figure 5.5 shows the difference spectrum normalized by Batchelor variables with η_B chosen to be the Batchelor scale of the less diffusive scalar at $R_\lambda \approx 8$ with Sc up to 1024 and Sc ratio up to 64. At high wavenumbers, the dominating term in Eq. 5.6 is the scalar spectrum of the less diffusive scalar $E_{\beta\beta}(k)$, because the co-spectrum $E_{\alpha\beta}$ is negligible at small scales according to Fig. 5.3 where $\rho_{\alpha\beta}$ drops fast at high wavenumbers and $E_{\alpha\beta}$ drops faster than $E_{\beta\beta}$. The less diffusive scalar ϕ_β has more small-scale content than the more diffusive scalar ϕ_α . Therefore, it is likely that the difference spectrum at small scales can be described by Batchelor scaling based on parameters of the less diffusive scalar. Indeed, the difference spectrum $F_{\alpha\beta}$ in Fig. 5.5 “collapse” at high wavenumbers for all scalar pairs with different Sc ratio. At intermediate to large scales, the co-spectrum becomes more important and $F_{\alpha\beta}$ “collapse” according to Sc ratios with larger Sc scalar pair having a higher difference spectrum at large scales. It is interesting to note that for the scalar pair $Sc = \{1, 64\}$ with the highest Sc ratio 64 (curve B), there is an emerging flat region suggesting the difference spectrum for high Sc -ratio

scalar pair may also exhibiting a k^{-1} scaling range. Results at even higher Sc ratio will provide more evidence.

5.2 Scalar spectral transfer

Scalar transfer spectrum $T_\phi(\mathbf{k})$ serves as a redistributive ($\int_{\mathbf{k}} T_\phi(\mathbf{k}) d\mathbf{k} = 0$) term in the evolution equation of scalar spectrum

$$\frac{\partial E_\phi(\mathbf{k})}{\partial t} = T_\phi(\mathbf{k}) + G_\phi(\mathbf{k}) - 2Dk^2 E_\phi(\mathbf{k}), \quad (5.7)$$

where D is the molecular diffusivity and $G_\phi(\mathbf{k})$ accounts for the mean scalar gradient contribution. The scalar transfer spectrum $T_\phi(\mathbf{k})$ is defined as a non-linear triadic interaction between two scalar modes with scale size of $1/k$ and $1/q$ and one velocity mode of scale size $1/p$ in Fourier space. Here, the wavenumber vectors \mathbf{k} , \mathbf{p} and \mathbf{q} form a triangle, i.e., $\mathbf{p} + \mathbf{q} = \mathbf{k}$. In particular, $T_\phi(\mathbf{k})$ is given by

$$T_\phi(\mathbf{k}) = 2k_j Im \left[\langle \hat{\phi}^*(\mathbf{k}) \int_{\mathbf{k}=\mathbf{p}+\mathbf{q}} \hat{u}_j(\mathbf{p}) \hat{\phi}(\mathbf{q}) d\mathbf{p} \rangle \right], \quad (5.8)$$

where Im denotes the imaginary part and the asterisk denotes a complex conjugate. In order to understand the details of spectral transfer process, the transfer spectrum can be decomposed into contributions from different velocity modes \mathbf{p} and scalar modes \mathbf{q}

$$T_\phi(k) = \sum_p V_\phi(k|p) = \sum_q S_\phi(k|q), \quad (5.9)$$

and $V_\phi(k|p)$ and $S_\phi(k|q)$ can be further decomposed as

$$V_\phi(k|p) = \sum_q T_\phi(k|p, q), \quad (5.10)$$

and

$$S_\phi(k|q) = \sum_p T_\phi(k|q, p). \quad (5.11)$$

Qualitatively, many features of scalar spectral transfer at high Schmidt numbers are similar to those seen in previous work (Yeung 1996). The classical forward cascade behavior is observed: $T_\phi(k)$ and $V_\phi(k|p)$ are negative at low wavenumbers and positive at high wavenumbers; $S_\phi(k|q)$ is negative below the midpoint of each q range and positive above it

with maximum values occurring at the two ends of the q range. At high wavenumbers, the dominant contributions to velocity-scalar interactions (see Fig. 5.7) are nonlocal involving a lower wavenumber velocity mode, suggesting that the large-scale motion affects the small-scale scalar field. However, results for $S_\phi(k|q)$ and $T_\phi(k|p, q)$ show that scalar transfer at high wavenumbers are local, which means that scalar fluctuations at large scales do not affect the small scales. On the other hand, at low wavenumbers, velocity-scalar interactions are more local in nature and scalar transfer is moderately non-local.

In order to compare the rate of scalar spectral transfer at different Reynolds and Schmidt numbers, the scalar variance is normalized to unity in all cases such that the magnitude reflects the relative rate of spectral transfer. Fig. 5.6 and 5.7 show the scalar spectral transfer $T_\phi(k)$ (dashed line) and its decomposition into contribution from different velocity modes $V_\phi(k|p)$, where each solid curve corresponds to the logarithmically spaced wavenumber ranges separated by vertical dashed lines. Fig. 5.6 shows $V_\phi(k|p)$ at $R_\lambda \approx 8$ for $Sc = 1, 8, 64$ and 1024 . Spectral transfer mainly comes from the two lowest velocity modes ($1 \leq p \leq 4$). The forward cascading process is observed, indicated by $T_\phi(k)$ and $V_\phi(k|p)$ that they are negative at low wavenumbers and become positive at high wavenumbers. The transition wavenumber where spectral transfer becomes positive increases with Sc , which suggests that some spectral content is taken out from smaller scales to the high wavenumbers at high Sc .

In general, spectral transfer rate at low to moderate wavenumbers decreases with Schmidt number. As Sc increases, the transfer spectrum curve tends to spread out towards the high wavenumbers. It is seen from Fig. 5.7 that strong non-local velocity-scalar interactions occur at high wavenumbers where velocity mode $2 \leq p \leq 4$ contributes the most. The transfer rate at high wavenumbers increases with Sc up to $Sc = 64$, and $V_\phi(k|p)$ at $Sc = 1024$ is smaller than $Sc = 64$. However, the DNS results for $Sc = 256, 512, 1024$ (not shown) indicate that $T_\phi(k)$ at high wavenumbers increases with Sc . The reason why this trend is not monotonic from $Sc = 64$ (128^3) to 1024 (512^3) might be due to the resolution difference. It can be inferred that the transfer rate at high wavenumbers increases with Sc , which is opposite to the trend at low wavenumbers. This is consistent with the findings

in scalar spectrum where scalars at high Sc has more high wavenumber content. By comparison with results for $V_\phi(k|p)$ at high Reynolds number $R_\lambda \approx 38$ and $R_\lambda \approx 90$ in Yeung (1996), it is found that turbulent motions of intermediate scales tend to be significant for scalar spectral transfer at high Reynolds numbers, which is consistent with previous finding that velocity modes near the peak of the energy dissipation spectrum contribute the most to the transfer.

Fig. 5.8(a) and (b) show the decompositions of $V_\phi(k|p)$ for the most significant modes $1 \leq p \leq 4$ into $T_\phi(k|p, q)$ where different curves represent different scalar modes q . Strong mutual cancellation between adjacent scalar modes at moderate to high wavenumbers can be observed. At high wavenumbers, scalar transfer is local, i.e., the dominant contributions are from scalar mode q very close to k . Scalar transfer becomes weaker for high Sc at intermediate scales and scalar transfer from high wavenumber modes becomes more significant, because scalars of high Sc have more high wavenumber content. The peaks of the transfer occur at the boundaries between adjacent wavenumber ranges and the “spikes” become narrower at high wavenumbers, which means that scalar transfer becomes more local as it cascades to the small scales. Fig. 5.8(c) and (d) show $S_\phi(k|q)$, the contributions to the spectral transfer from different scalar modes q . Qualitatively, $S_\phi(k|q)$ is very similar to $T_\phi(k|p, q)$. As Sc increases, the scalar mode with the highest peak increases.

Furthermore, $S_\phi(k|q)$ can be decomposed into $T_\phi(k|q, p)$ as shown in Fig. 5.9 for q at low to moderate wavenumbers. The largest contributions from velocity modes are the lowest couple of wavenumber ranges, the same as results for $V_\phi(k|p)$ in Fig. 5.6 and 5.7. The shape of $T_\phi(k|q, p)$ is very similar to $S_\phi(k|q)$ and they peak at the same wavenumber k . Unlike the mutual cancellation of $T_\phi(k|p, q)$, contributions from different velocity modes $T_\phi(k|q, p)$ are in phase and add up to $S_\phi(k|q)$.

5.3 *Scalar subgrid transfer*

In Large Eddy Simulation (LES), only large scales of turbulent motions are simulated whereas the dynamics of the small scales are modeled by the subgrid-scale (SGS) models.

Similarly, in the LES approach to studying scalars, corresponding scalar SGS models have to be used. One means of incorporating passive scalar transport into LES is to introduce turbulent Schmidt number Sc_t and closure is obtained when either Sc_t is specified as a model parameter or is estimated using a dynamic procedure (Pullin 2000). This turbulent Schmidt number can be obtained using DNS. Based on the methodology of studying SGS energy (Domaradzki *et al.* 1987, 1990) and scalar transfer (Yeung and Zhou 1996) by DNS, data are obtained for SGS scalar transfer and related SGS parameters at high Schmidt numbers in an effort to have more complete understanding of the physical process of scalar SGS transfer for a wider range of Schmidt numbers.

In the DNS approach to studying SGS transfer, a fictitious cutoff wavenumber k_c is introduced, which separates the scales into resolvable ($k \leq k_c$) and subgrid ($k > k_c$) ranges. The scalar transfer spectrum for the resolvable scales can be written as

$$T_\phi(k) = T_\phi^{<<}(k|k_c) + T_\phi^{><}(k|k_c) + T_\phi^{>>}(k|k_c), \quad (5.12)$$

where $T_\phi^{<<}(k|k_c)$ is the fully resolvable scale transfer for triadic interaction with $k, p, q \leq k_c$, (k, p, q are defined in Eq. 5.8), $T_\phi^{><}(k|k_c)$ is the resolvable-subgrid transfer with one of p and q in the resolvable range and the other in the subgrid range, $T_\phi^{>>}(k|k_c)$ is the fully subgrid transfer with both $p, q > k_c$. The total subgrid transfer $T_\phi^s(k|k_c)$ is written as

$$T_\phi^s(k|k_c) = T_\phi^{><}(k|k_c) + T_\phi^{>>}(k|k_c). \quad (5.13)$$

Subgrid transfer $T_\phi^s(k|k_c)$ is the rate at which scalar is transferred into and out of the resolvable range due to interactions with subgrid scales. In SGS models, the SGS transfer is modeled by the subgrid diffusivity, defined as

$$D_e(k|k_c) = -\frac{T_\phi^s(k|k_c)}{2k^2 E_\phi(k)}. \quad (5.14)$$

Similarly, some SGS models use turbulent Schmidt number (or Prandtl number) as the input parameter, which is defined as

$$Sc_t(k|k_c) = \frac{\nu + \nu_e(k|k_c)}{D + D_e(k|k_c)}, \quad (5.15)$$

where ν and D are viscosity and molecular diffusivity, respectively, and $\nu_e(k|k_c)$ is the turbulent eddy viscosity similarly defined as the ratio of energy transfer and energy spectrum

$$\nu_e(k|k_c) = -\frac{T(k|k_c)}{2k^2 E(k)}. \quad (5.16)$$

In a forward cascade process, the net effect of the subgrid scales on the resolvable scales is to transfer the scalar fluctuations towards smaller scales and the eddy diffusivity is positive. When inverse transfer occurs, i.e., the net scalar fluctuations are transferred towards larger scales, the eddy diffusivity becomes negative. Usually, both forward and inverse transfer occur among different wavenumber modes.

To give an idea how different types of triadic interactions as shown in Eq. 5.12 contribute to the total spectral transfer, Figure 5.10 shows the decomposition of scalar spectral transfer for $Sc = 1$ and $Sc = 64$ at $R_\lambda \approx 38$. At low wavenumbers, subgrid transfer is almost zero because local triadic interactions dominate. Negative resolved-subgrid scale transfer emerges at wavenumbers close to the cutoff wavenumber k_c . This negative subgrid transfer suggests a net effect of forward cascade process that transfers scalar fluctuations to the smaller scales with $k > k_c$. It also implies a moderately non-local transfer. The fully subgrid transfer with $p, q > k_c$ are negligible compared to other contributions which means few non-local triadic interactions. The spectral transfer in the resolved range also shows a forward cascade with the resolved and the total transfer being negative at low wavenumbers and positive at high wavenumbers. It can be seen that subgrid transfer is important only in the resolved range that are close to the cutoff wavenumber. For the high Sc case in Fig. 5.10(b), the magnitude of spectral transfer is less than the low Sc case in (a) and there is strong mutual cancellation of the resolved transfer and the resolved-subgrid transfer at close to k_c .

The cutoff wavenumber k_c is an important parameter in LES and SGS transfer. Intuitively, higher k_c in LES gives more accurate results and requires higher resolution and the SGS transfer will be restricted to a narrower region close to k_c . Lower k_c in LES corresponds to a coarser grid simulation. Fig. 5.11 shows the resolved transfer, the subgrid transfer and the corresponding sub-grid diffusivity for scalar $Sc = 64$ at $R_\lambda \approx 38$ for different k_c . As k_c

increases, the ranges of scales in the resolvable region increases as shown in (a). For high k_c , subgrid transfer and subgrid diffusivity become less and appear confined in a narrower region.

As Sc increases, the scalar spectrum at high wavenumbers will increase and the subgrid transfer will subsequently increase. But the subgrid diffusivity depends on the ratio of subgrid transfer and the scalar spectrum (as in Eq. 5.14) and will be determined by the relative strength of these two factors. Fig. 5.12 shows the subgrid transfer and subgrid diffusivity for $Sc = 1, 8$ and 64 at $R_\lambda \approx 8$ and $k_c = 8$ and 16 . In Fig. 5.12(a) and (b), the subgrid transfer at close to k_c indeed increases with Sc . The subgrid diffusivity in Fig. 5.12(c) and (d), however, shows much less dependence on Sc , especially at higher k_c . At $k_c = 8$, subgrid diffusivity at close to k_c shows slightly decreasing trend with Sc , indicating that the increase of scalar spectrum with Sc at high wavenumbers dominates that of the transfer spectrum.

It is expected the turbulent Schmidt number will be very sensitive to the cutoff wavenumber k_c , because in the definition in Eq. 5.15, $Sc_t(k|k_c)$ has non-linear relation with the subgrid eddy viscosity and subgrid diffusivity, which depend on both the spectrum and the transfer spectrum. Fig. 5.13 shows the turbulent Schmidt number for $Sc = 16, 32$ and 64 at $k_c = 4, 16, 32$ and 64 . It is seen that as k_c increases from Fig. 5.13(a) to (d), $Sc_t(k|k_c)$ becomes closer to the actual Schmidt number at low wavenumber numbers. This is because both subgrid viscosity and diffusivity approaches zero at low wavenumbers as k_c increases. At wavenumber close to k_c for relatively high $k_c = 16, 32, 64$, the subgrid viscosity and diffusivity dominate the viscosity and molecular diffusivity, respectively. Furthermore, subgrid diffusivity increases with wavenumber faster than subgrid viscosity because the scalar has more high wavenumber contents than the velocity field. This will make the turbulent Schmidt number decreases at k close to k_c . This trend is reversed for $Sc < 1$ as in Yeung and Zhou (1996) where subgrid viscosity increases faster than subgrid diffusivity. Fig. 5.13 may provide some criteria as to how high the cutoff number should be in a LES in order to obtain reasonably accurate results.

Subgrid transfer can also be decomposed into contributions from modes of forward and inverse transfer, i.e., the modes with negative and positive transfers, respectively. The spectral transfers and subgrid diffusivities shown in the previous figures are the net results from contributions from both forward and inverse transfer. Figure 5.14 shows the forward, the inverse and the net transfer and the corresponding subgrid diffusivity to see their relative strength. This figure suggests that although the net subgrid transfer is a forward cascading process, there are significant inverse transfer contributions, i.e., transfer from subgrid scales to the resolved scales. Similarly, the decomposition of the fully subgrid transfer shown in Fig. 5.15 suggests that at higher k_c , the forward and inverse transfer for non-local triadic interactions are almost equally likely.

In this chapter, several aspects of the DNS results have been examined, including differential diffusion, between two scalars with different molecular diffusivity advected by the same turbulent flow, the scalar spectral transfer and the subgrid scalar transfer. It is found that Schmidt number ratio (also the ratio of molecular diffusivity) between the two scalars at high Sc is an important parameter in differential diffusion and the higher this ratio is, the two scalars tend to be more uncorrelated. The magnitude of the Sc 's of the two scalars and Reynolds numbers are less important. Scalar spectral transfer at high Schmidt numbers undergoes the forward transfer process and it becomes weaker at moderate to large scales as Sc increases, but the transfer increases with Sc at small scales. Subgrid scale scalar transfer is dominated by forward transfer process although there are also significant transfer contributions. Subgrid transfer weakens with increasing cutoff wavenumber and becomes stronger with increasing Sc .

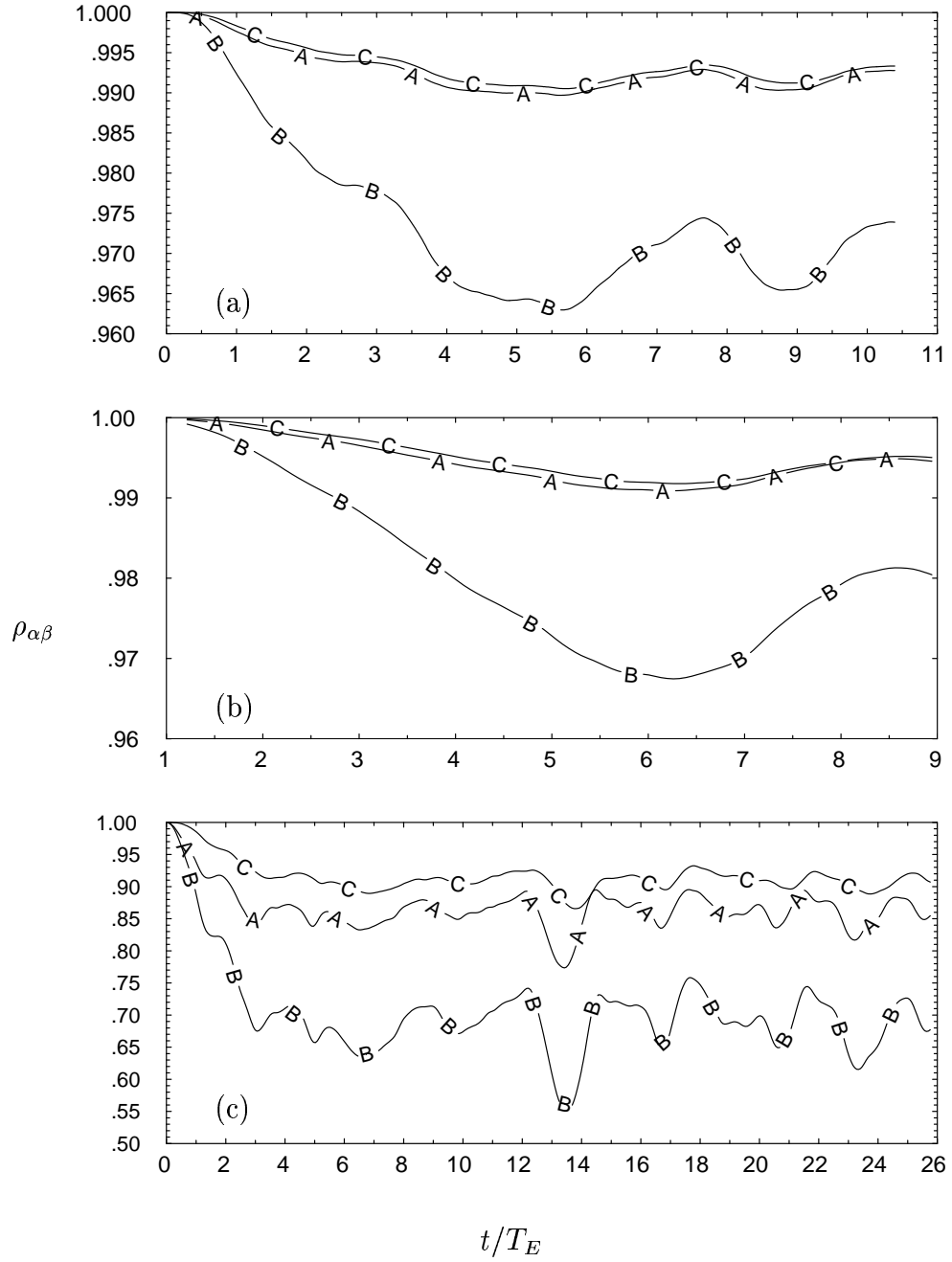


FIG. 5.1(a) Evolution of the scalar correlation coefficient $\rho_{\alpha\beta}$. Line A, B, and C represent scalar pairs with (a). $Sc = \{16, 32\}$, $Sc = \{16, 64\}$ and $Sc = \{32, 64\}$ at $R_\lambda \approx 38$. (b). $Sc = \{256, 512\}$, $Sc = \{256, 1024\}$ and $Sc = \{512, 1024\}$ at $R_\lambda \approx 8$. (c). $Sc = \{1, 8\}$, $Sc = \{1, 64\}$ and $Sc = \{8, 64\}$ at $R_\lambda \approx 8$.

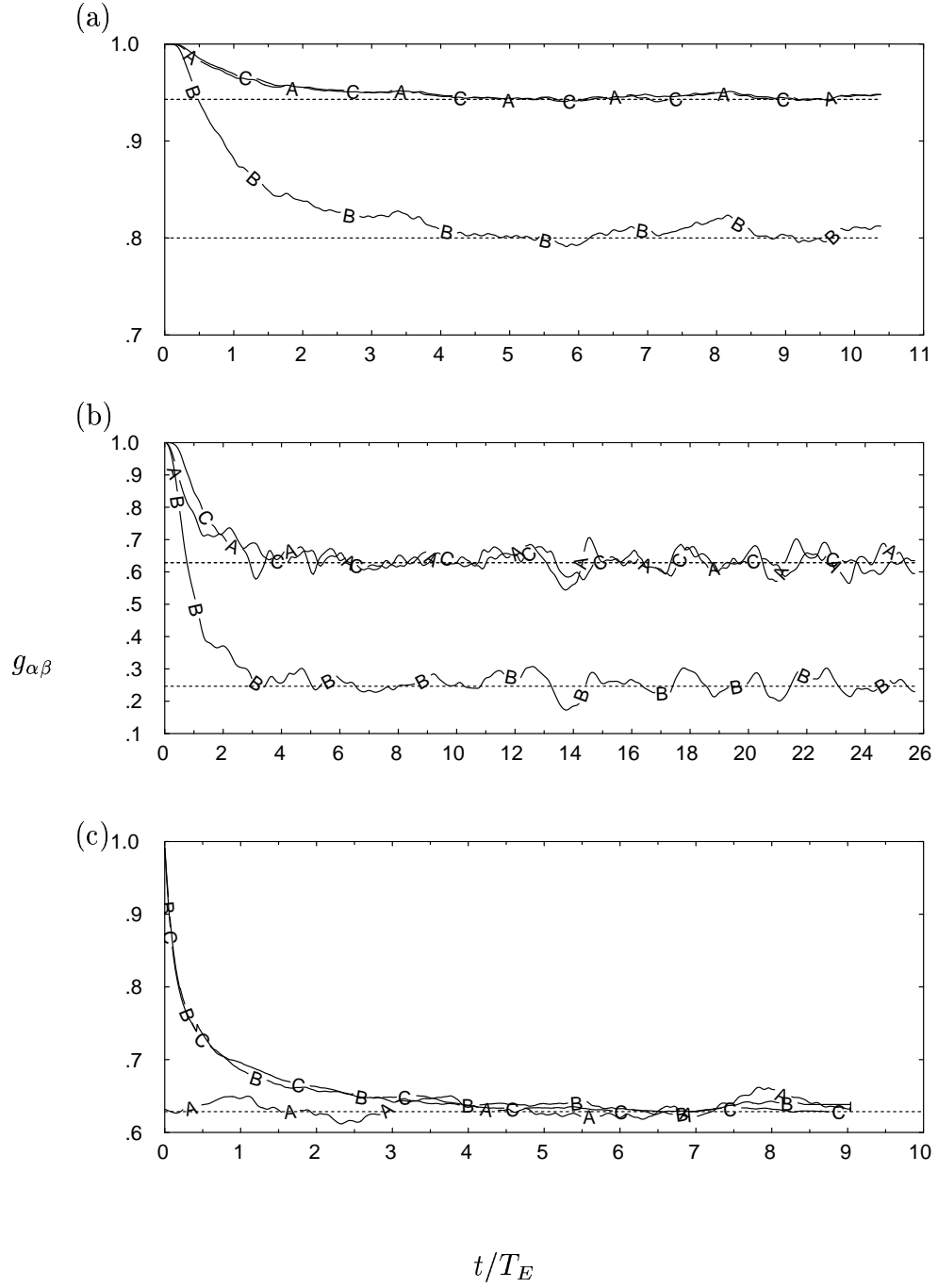


FIG. 5.2 Evolution of the scalar gradient ($\nabla_{\parallel}\phi$) correlation coefficient $g_{\alpha\beta}$. Line A, B, and C represent scalar pairs with (a) $Sc = \{16, 32\}$, $Sc = \{16, 64\}$ and $Sc = \{32, 64\}$ at $R_{\lambda} \approx 38$. (b) $Sc = \{1, 8\}$, $Sc = \{1, 64\}$ and $Sc = \{8, 64\}$ at $R_{\lambda} \approx 8$. (c) $Sc = \{1/8, 1\}$ at $R_{\lambda} \approx 140, 240$ and 390 . Dashed line represents the large time limit in Eq. 5.3.

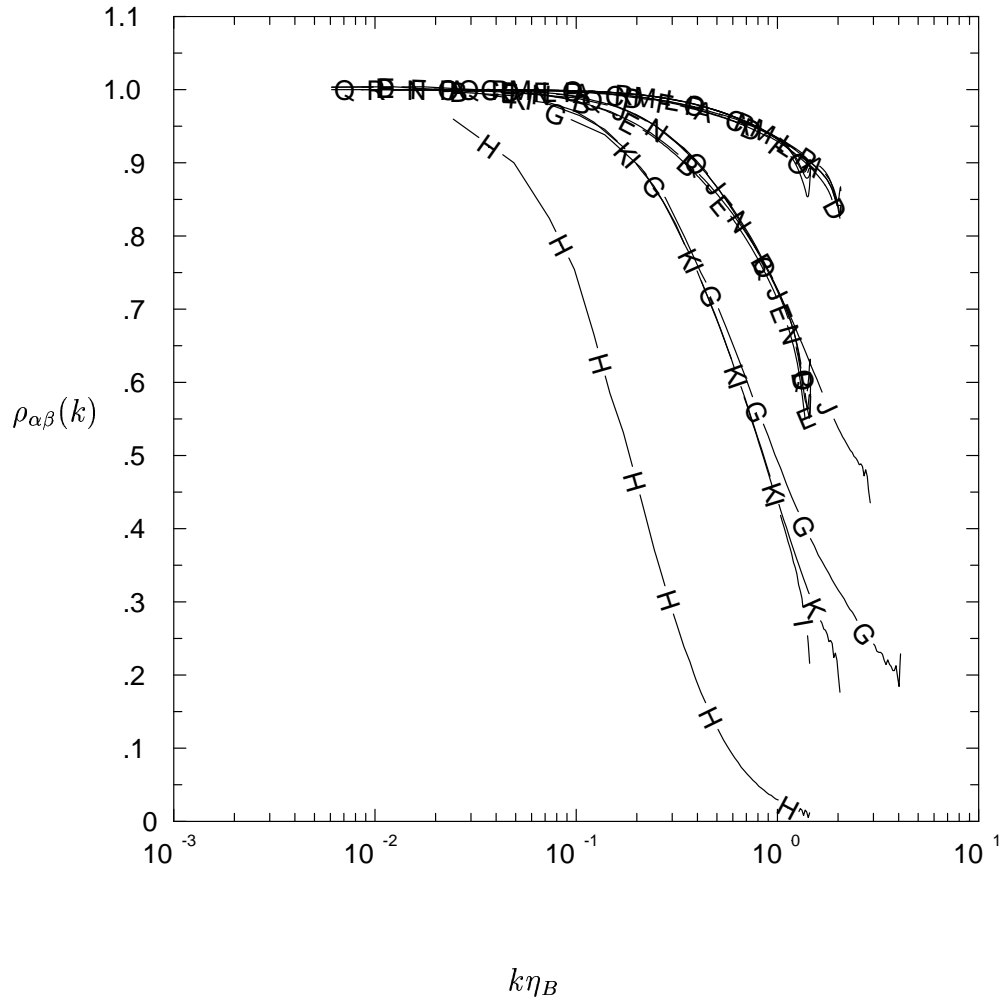


FIG. 5.3 Coherency spectrum as defined in Eq. 5.4, where we normalized wavenumber by η_B of the less diffusive scalar. Lines A-F represent scalar pairs with $Sc = \{4, 8\}, \{4, 16\}, \{8, 16\}, \{16, 32\}, \{16, 64\},$ and $\{32, 64\}$ at $R_\lambda \approx 38$. Lines G-R represent scalar pairs with $Sc = \{1, 8\}, \{1, 64\}, \{8, 64\}, \{4, 16\}, \{4, 32\}, \{16, 32\}, \{64, 128\}, \{64, 256\}, \{128, 256\}, \{256, 512\}, \{256, 1024\}$ and $\{512, 1024\}$, respectively, at $R_\lambda \approx 8$. The curves “collapse” according to Sc ratio of the scalar pair.

$\text{Log}_{10}\text{PDF}$ of phase angle

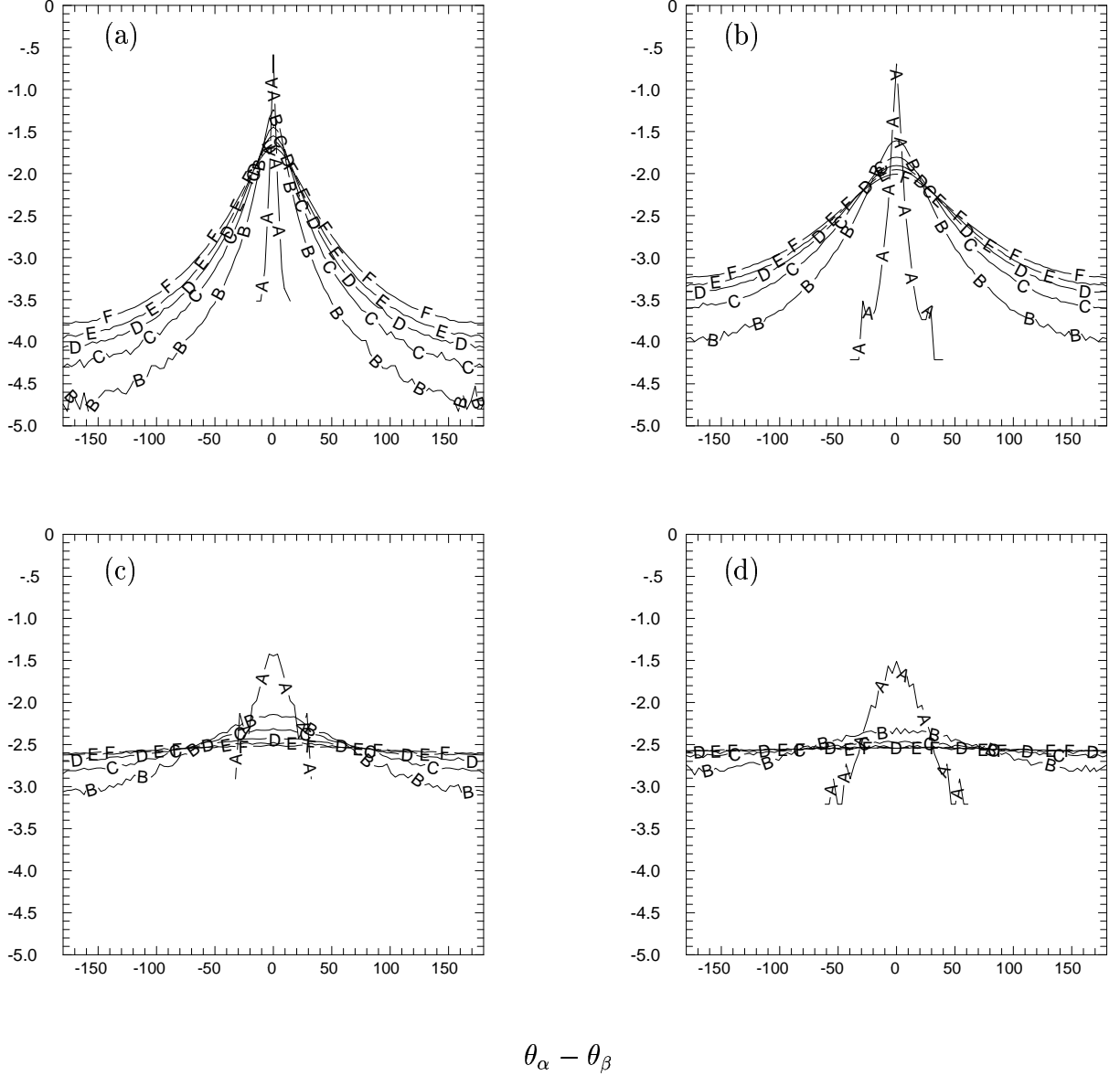


FIG. 5.4 PDFs of the difference in phase angle at $R_\lambda \approx 8$ between scalars: (a) $Sc = \{512, 1024\}$, (b) $Sc = \{256, 1024\}$, (c) $Sc = \{1, 8\}$, (d) $Sc = \{1, 64\}$. (a), (b) lines A-F represent $k = 6, 46, 86, 126, 166, 206$, respectively. (c), (d) lines A-F represent $k = 2, 12, 22, 32, 42, 52$, respectively.

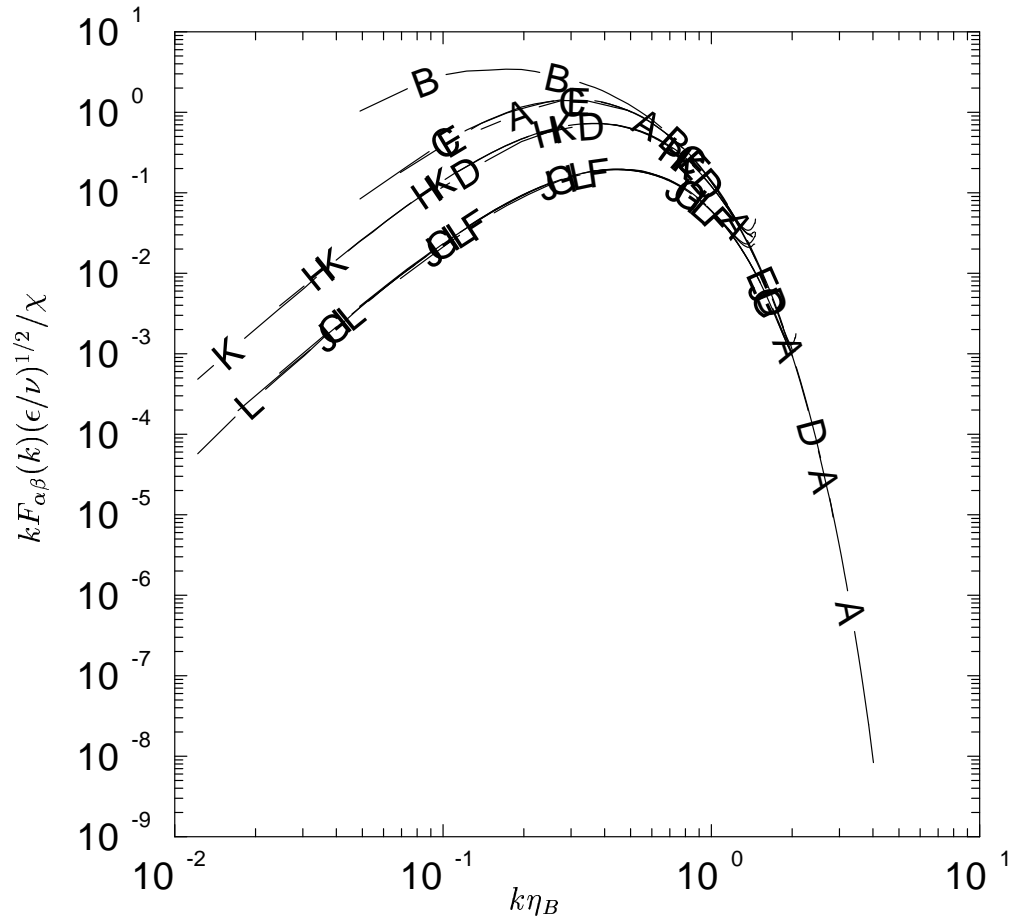


FIG. 5.5 Difference spectrum as defined in Eq. 5.6, where we normalized wavenumber by η_B of the less diffusive scalar. Lines A-L represent scalar pairs with $Sc = \{1, 8\}$, $\{1, 64\}$, $\{8, 64\}$, $\{4, 16\}$, $\{4, 32\}$, $\{16, 32\}$, $\{64, 128\}$, $\{64, 256\}$, $\{128, 256\}$, $\{256, 512\}$, $\{256, 1024\}$ and $\{512, 1024\}$, respectively, at $R_\lambda \approx 8$.

$$T_\phi(k|p)$$

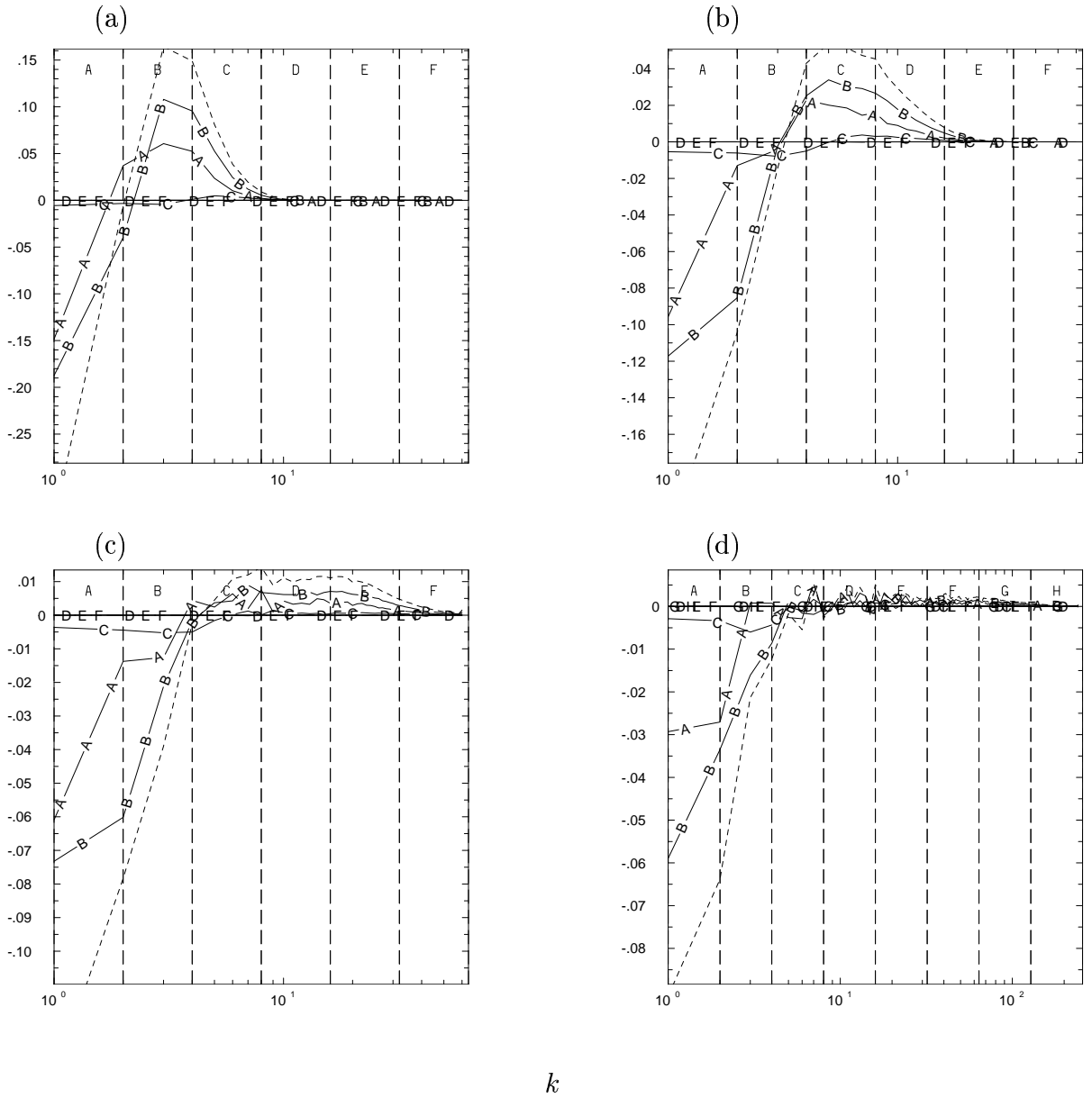


FIG. 5.6 Decomposition of the scalar transfer spectrum into contributions $T_\phi(k|p)$ from velocity modes p in the logarithmic spaced ranges A-F in (a), (b), (c) and A-H in (d), where dashed lines are the overall scalar transfer $T_\phi(k)$. All from DNS data sets at $R_\lambda \approx 8$. (a) $Sc = 1, 128^3$. (b) $Sc = 8, 128^3$. (c) $Sc = 64, 128^3$. (d) $Sc = 1024, 512^3$.

$$T_\phi(k|p)$$

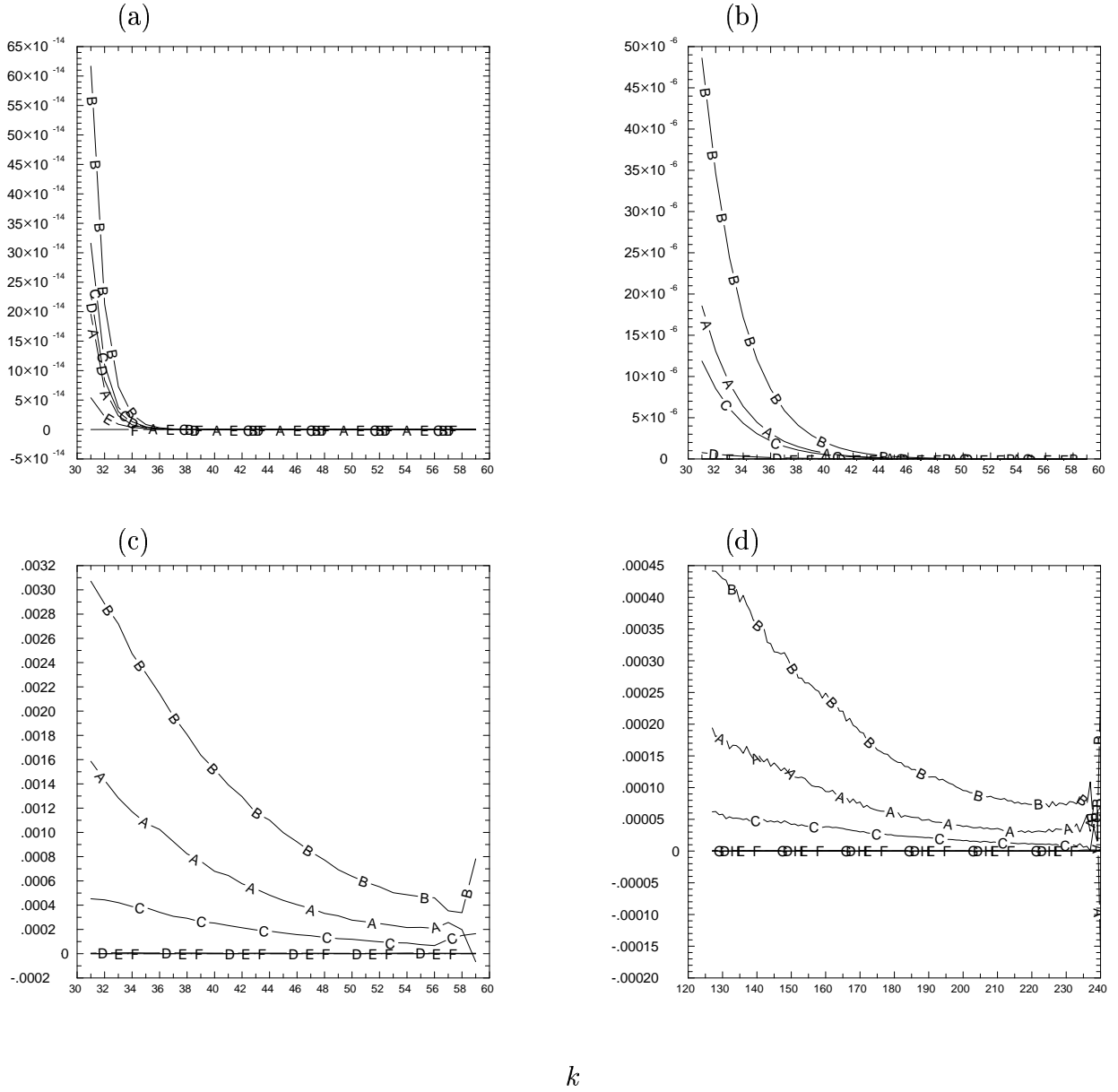


FIG. 5.7 The same as FIG. 5.6, shown only for high wavenumbers.

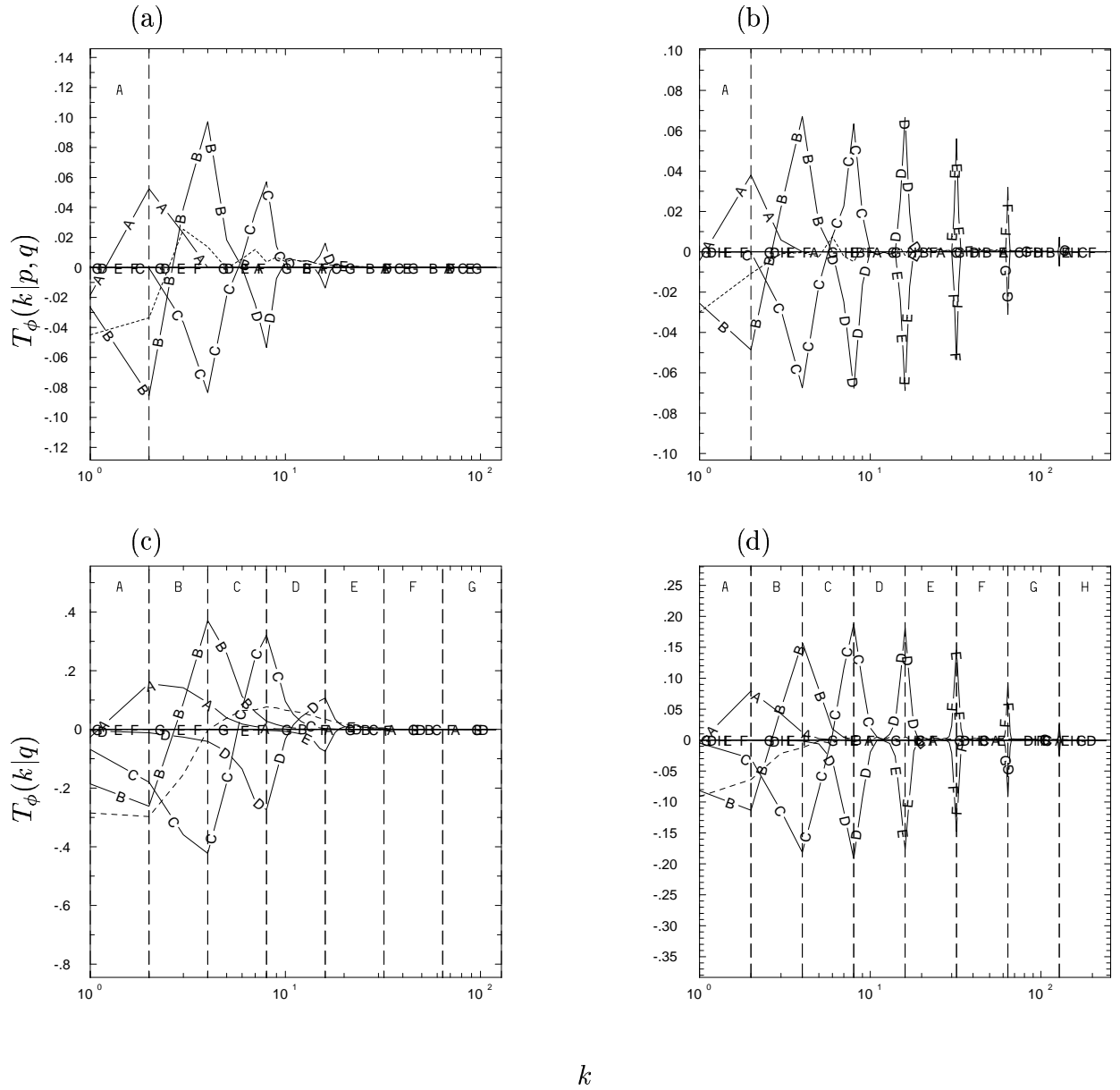


FIG. 5.8 Decomposition of scalar spectral transfer at $R_\lambda \approx 38$. (a) $T_\phi(k|p, q)$, $Sc = 1$, dashed line for $T_\phi(k|p)$, $1 \leq p \leq 2$, solid curves correspond to q at different ranges, (b) same as (a) for $Sc = 64$, (c) $T_\phi(k|q)$, $Sc = 1$, dashed line for $T_\phi(k)$, (d) same as (c) for $Sc = 64$.

Transfer spectrum

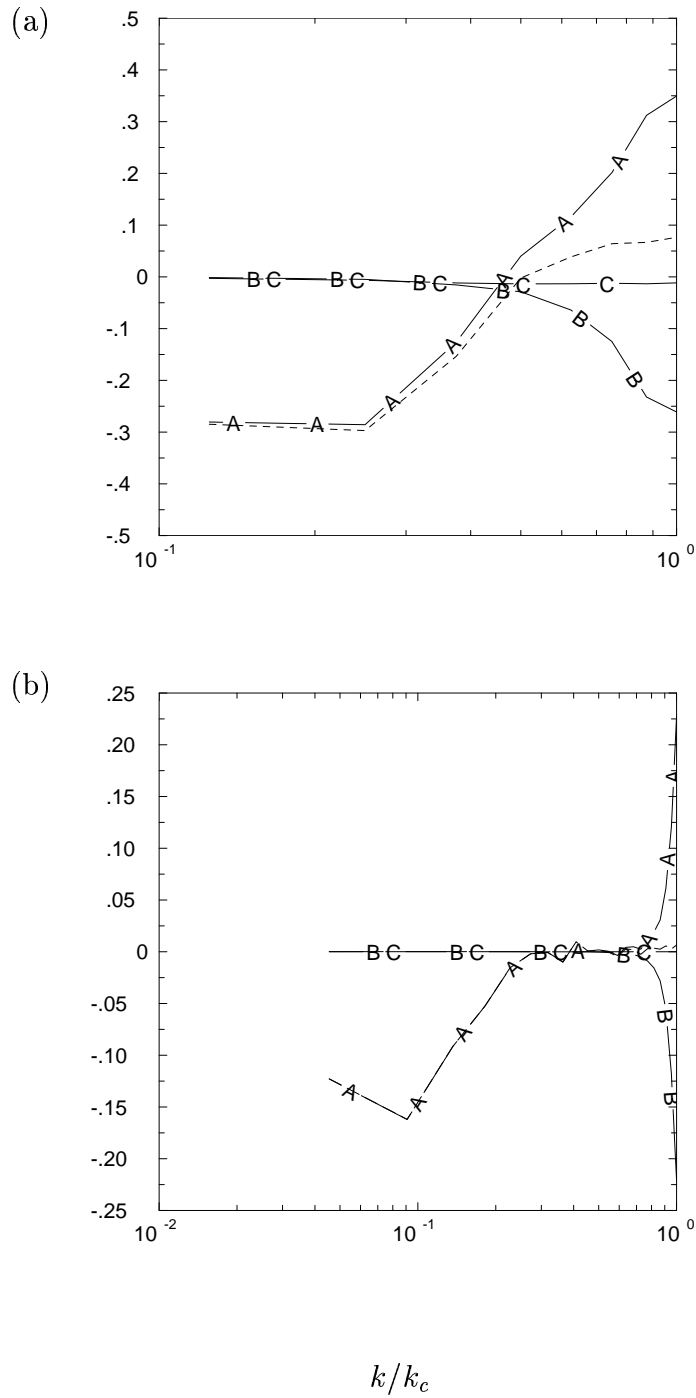


FIG. 5.10 Decomposition of scalar transfer spectrum $T_\phi(k)$ (dashed line) into fully resolvable transfer $T_\phi^{<<}(k|k_c)$ (line A), resolvable-subgrid transfer $T_\phi^{><}(k|k_c)$ (line B) and fully subgrid transfer $T_\phi^{>>}(k|k_c)$ (line C). (a) $Sc = 1$ at $R_\lambda \approx 38$ (256^3), $k_c = 8$, (b) $Sc = 64$ at $R_\lambda \approx 38$ (512^3), $k_c = 22$.

$$T_{\phi}^{<<}(k|k_c), T_{\phi}^s(k|k_c), D_e(k|k_c)$$

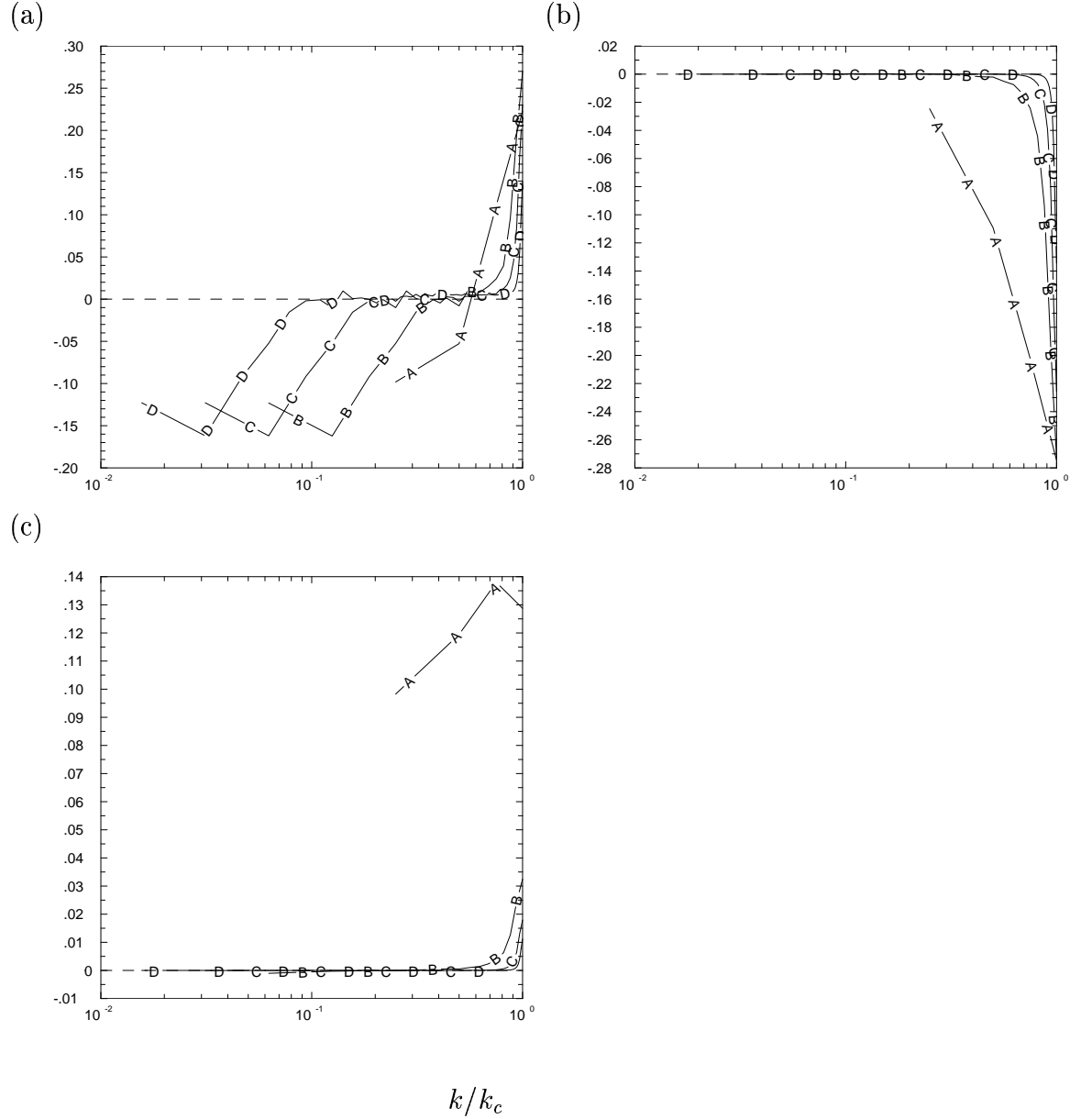


FIG. 5.11 (a) Fully resolvable transfer $T_{\phi}^{<<}(k|k_c)$ for $Sc = 64$ at $R_{\lambda} \approx 38$ at $k_c = 4, 16, 32, 64$ (lines A-D, respectively). (b) Same as (a) for subgrid transfer $T_{\phi}^s(k|k_c)$. (c) Same as (a) for subgrid eddy diffusivity $D_e(k|k_c)$.

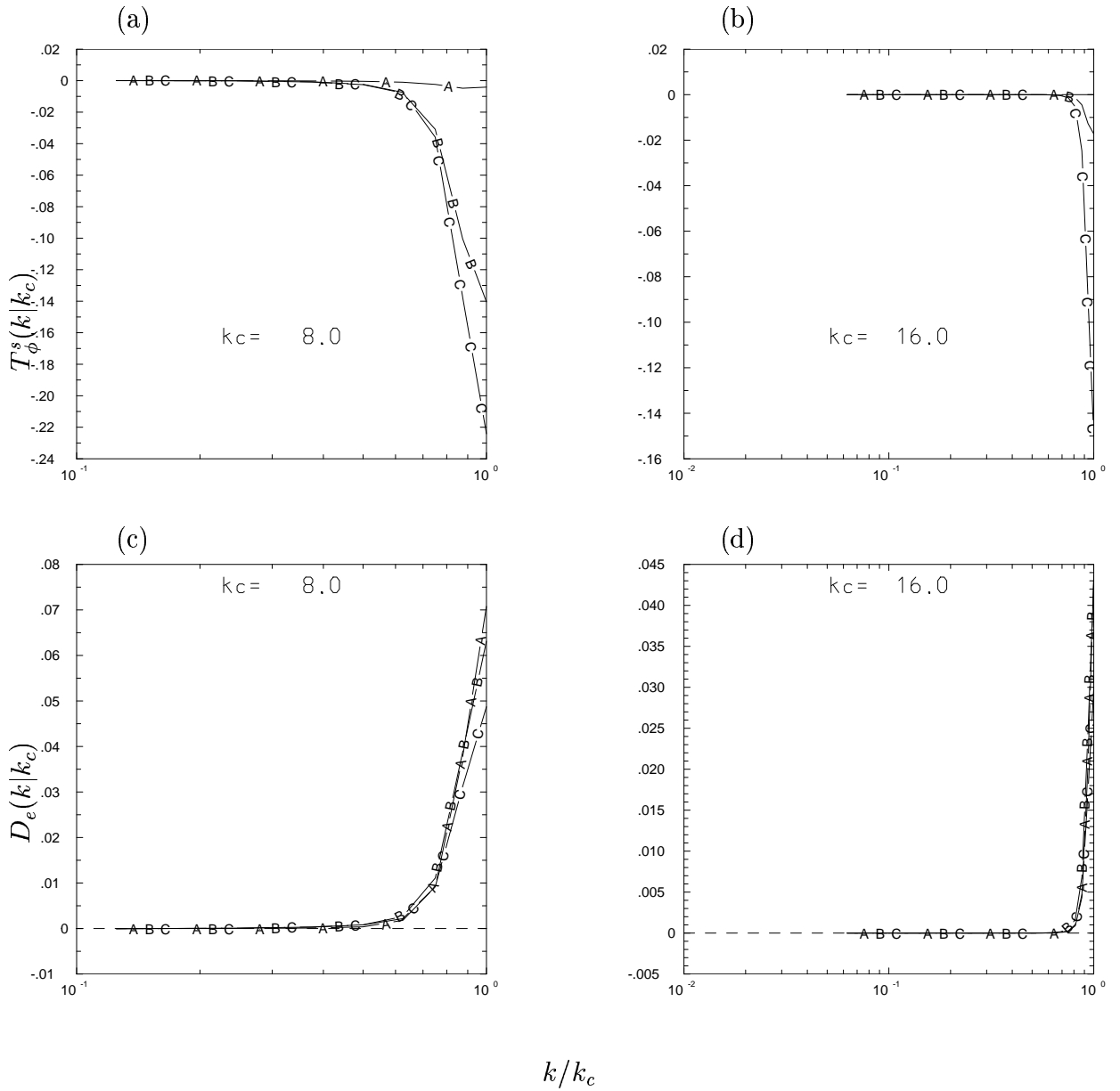


FIG. 5.12 (a) Subgrid transfer $T_\phi^s(k|k_c)$ for $Sc = 1, 8, 64$ (lines A-C) at $R_\lambda \approx 8$, $k_c = 8$. (b) Same as (a) at $k_c = 16$. (c) Subgrid diffusivity $D_e(k|k_c)$ with the same parameters as (a). (d) Same as (c) at $k_c = 16$.

$$S_{c_t}(k|k_c)$$

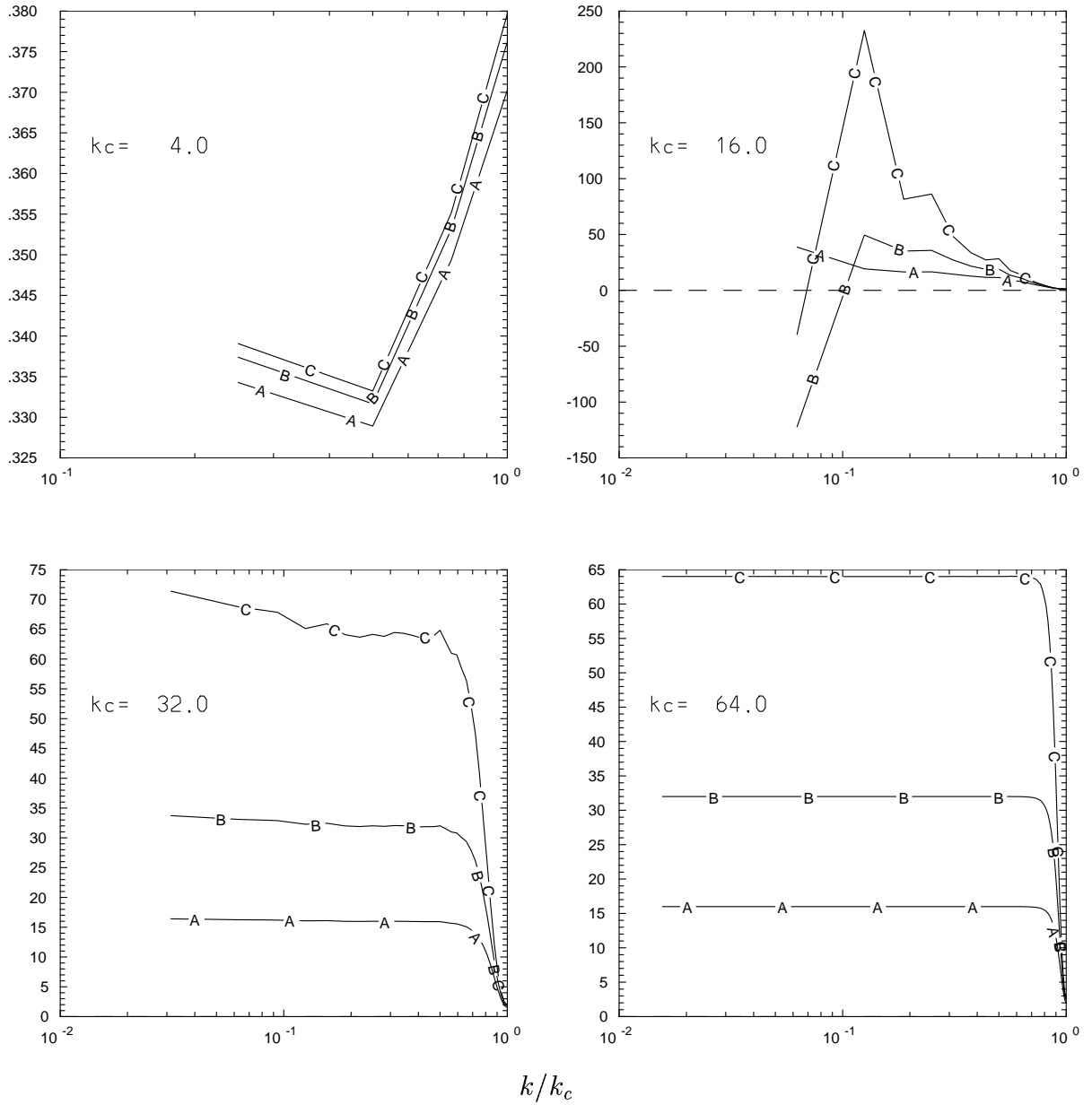


FIG. 5.13 Subgrid turbulent Schmidt number $S_{c_t}(k|k_c)$ for $Sc = 16, 32, 64$ (lines A-C) at $R_\lambda \approx 38$.

Decomposition of $T_\phi^s(k|k_c)$ and $D_e(k|k_c)$

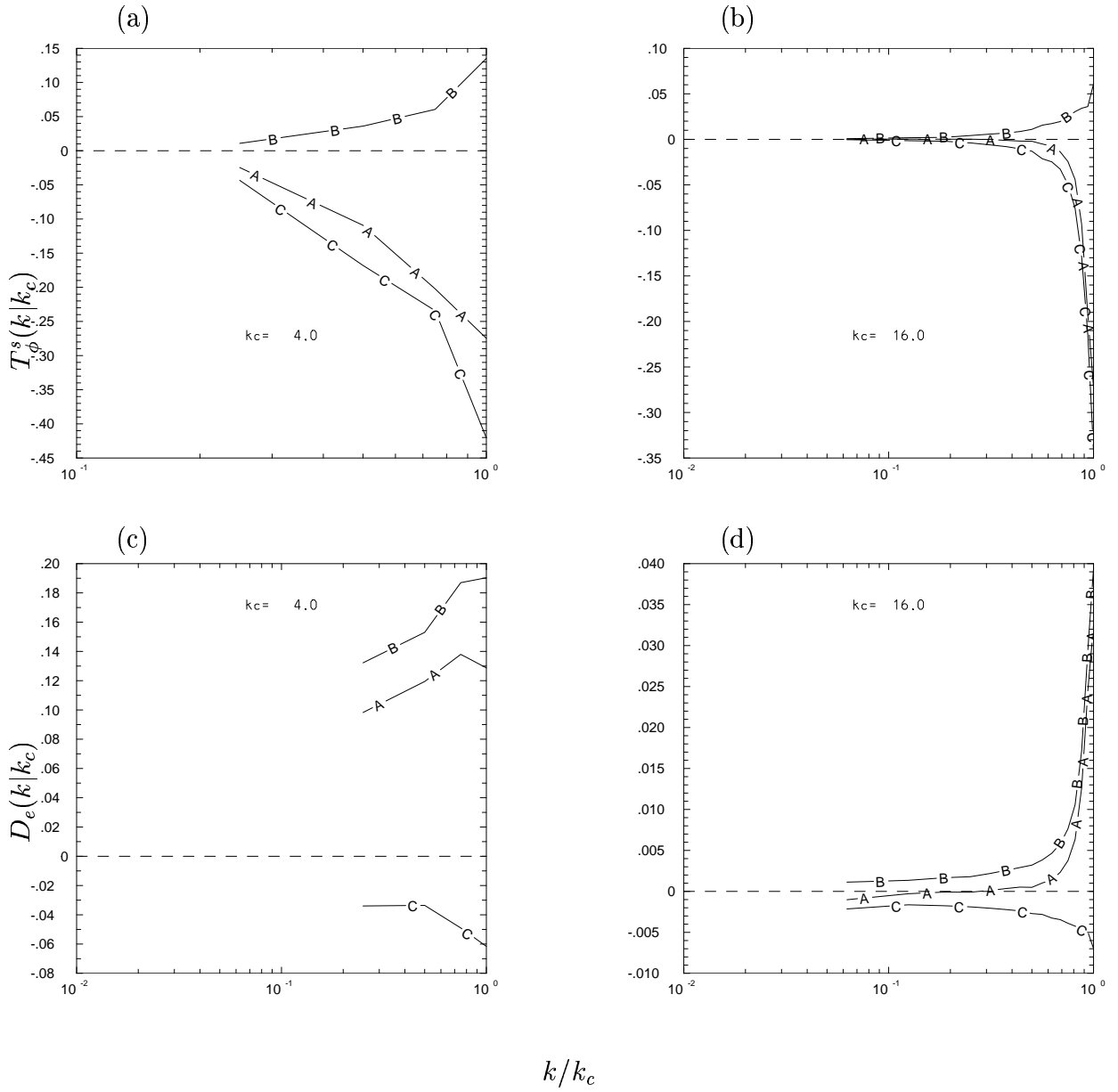


FIG. 5.14 (a) Subgrid transfer $T_\phi^s(k|k_c)$ (line A), its positive (line B) and negative contribution (line B and C) for $Sc = 64$ at $R_\lambda \approx 38$, $k_c = 4$. (b) Same as (a) at $k_c = 16$. (c) Corresponding decomposition of subgrid diffusivity $D_e(k|k_c)$ with the same parameters as (a) (d) Same as (c) at $k_c = 16$.

Decomposition of $T_\phi^{>>}(k|k_c)$

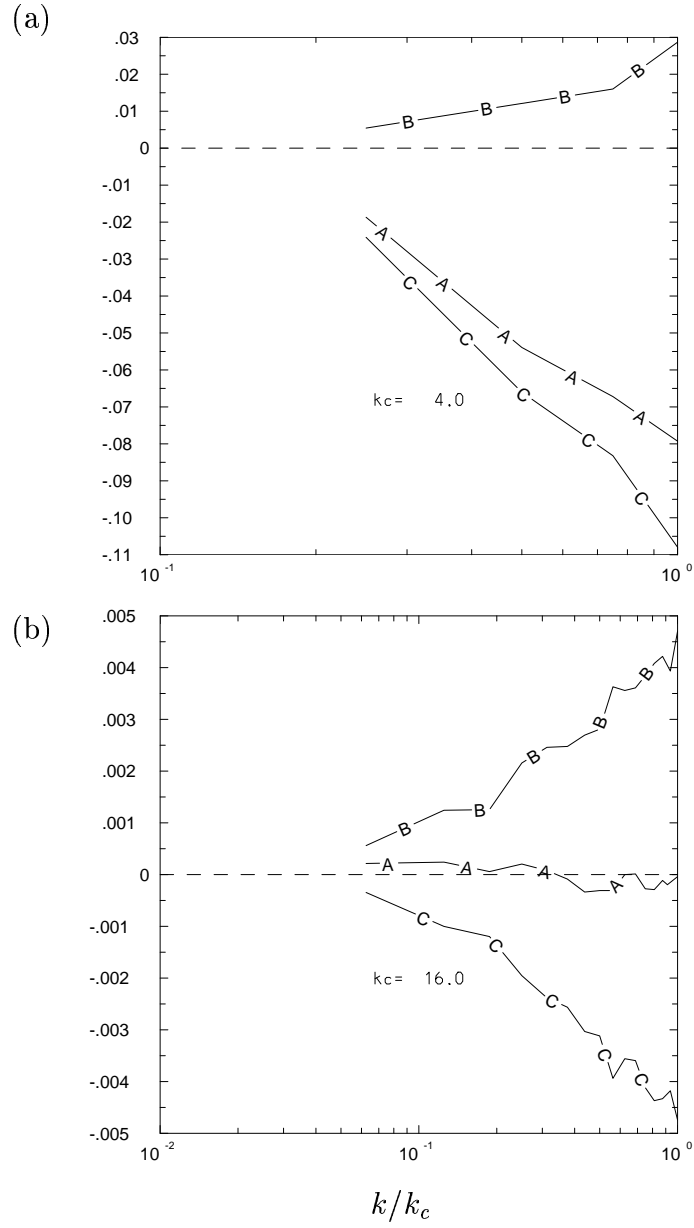


FIG. 5.15 Same as FIG. 5.14 (a) and (b), respectively, for decomposition of fully subgrid transfer.

CHAPTER VI

CONCLUSION

In this work, properties of passive scalars at high Schmidt numbers in stationary isotropic turbulence are studied by Direct Numerical Simulation (DNS). Schmidt numbers (Sc) as high as 1024 were achieved at Taylor-scaled Reynolds number $R_\lambda \approx 8$, in addition to $Sc = 64$ at $R_\lambda \approx 38$. The main objective is to contribute to the physical understanding of the scalar behavior in the limit of high Schmidt number.

Direct numerical simulation of stationary isotropic turbulence is performed on a cubic domain using a parallel code based on Rogallo's (1981) pseudo-spectral algorithm. Turbulent velocity field is made statistically stationary by a stochastic forcing scheme (Eswaran and Pope 1988) acting at large scales. The scalar field is also maintained stationary by a uniform mean scalar gradient. The instantaneous velocity and scalar field saved at different times are analyzed and ensemble averages at different times are taken as different realizations. The results for high Sc come from simulations using up to 512^3 grid points at $R_\lambda \approx 38$ and $R_\lambda \approx 8$ for Sc up to 64 and 1024, respectively. Results at $R_\lambda \approx 90, 140, 240, 390$ are also obtained for $Sc = 1/8$ and 1 using up to 1024^3 grid points.

In addition to the insights gained from the limited analyses of the DNS data, the DNS database also provided detailed information for further use as new theories and models come up. In the following section, summary of the results from Chap.III-V is given and possible future work that can provide additional understanding of scalar mixing at high Schmidt numbers is given.

6.1 *Principal results*

Chapter III presents results on the properties of moderately and weakly diffusive scalars through the scalar spectrum, structure functions and statistics of scalar gradient and scalar

dissipation. Moderately diffusive scalars with $Sc = 1/8$ and 1 appear to have inertial-convective ranges with Obukhov-Corrsin's $k^{-5/3}$ scaling from $R_\lambda \approx 140$ to 390 and the inertial-convective range widens with increasing Reynolds number. The Obukhov-Corrsin constant supported by the results is about 0.4 for $1 - D$ scalar spectrum, which is in agreement with experimental value from Sreenivasan (1996). Comparisons of scalar structure functions of up to order 8 with those of velocity structure function show that the scaling exponents of scalar structure functions in inertial range deviate more from the classical scaling than the corresponding velocity structure functions. This suggests that scalar field is more intermittent than velocity field in inertial range and agrees with similar finding by other researchers. The velocity-scalar mixed third-order structure function shows sustaining trend of approaching Yaglom's exact relation (1949) as Reynolds number increases. The mixed structure function at low Reynolds numbers ($R_\lambda \approx 38$ and 8) also approaches Yaglom's relation as Sc increases even though there is no inertial range at such low Reynolds numbers. The DNS results on scalar spectral at high Sc agree with Batchelor (1959) and Kraichnan (1968)'s models, both of which give a k^{-1} scaling range. Kraichnan's model works better in capturing the spectrum in the diffusive range. Unlike the moderately diffusive scalars at higher Reynolds number, the second-order scalar structure function for $Sc > 1$ at $R_\lambda \approx 38$ and 8 does not show a classical $2/3$ scaling range. The results for small-scale scalar statistics, such as odd-order moments and probability density function of scalar gradients do not support Kolmogorov's hypothesis of local isotropy. However, the normalized odd-order moments decreases with Sc suggesting that local isotropy is a better approximation at high Sc . Kurtosis (flatness) of scalar gradients and scalar dissipation shows that small-scale intermittency tends to an asymptotic level at high Sc .

In Chapter IV, intermittency exponents manifested by the two-point statistics of scalar dissipation are studied, including the two-point correlator $\langle \chi(x)\chi(x+r) \rangle$, the second-order moment of local dissipation $\langle \chi_r^2 \rangle$ and the variance of the logarithmic local dissipation $Var(\ln \chi_r)$. Comparisons are made for scalar dissipation with those of energy dissipation and enstrophy. A major challenge is to compute $\langle \chi(x)\chi(x+r) \rangle$ with local average taken over a three-dimensional cube of size r . It is found that the intermittency exponents obtained by

3-D averaging is larger than those obtained by 1-D averaging. The intermittency exponent for energy dissipation in inertial range increases with Reynolds number and reaches about 0.2 at $R_\lambda \approx 390$, which is close to the commonly cited value of 0.25. The three types of intermittency exponents for energy dissipation from the three two-point statistics mentioned above become closer to each other as Reynolds number increases. However, for scalar dissipation, the intermittency exponent of the variance of the logarithmic local dissipation is significantly larger than the other two types at high Sc . Intermittency exponents for scalar dissipation in inertial range are larger than those of the energy dissipation, indicating that scalar field is more intermittent in inertial range. The intermittency exponents of scalar dissipation in viscous-convective range has weak dependence on Sc at high Sc .

Results have been obtained for differential diffusion between two scalars transported by the same turbulent flow, scalar spectral transfer and subgrid transfer in Chapter V. The ratio of Schmidt number (also molecular diffusivity) between two scalars is an important parameter in differential diffusion and the two scalars tend to be more uncorrelated with increasing Sc ratio. The magnitude of Sc s of the two scalars is less important than the Sc ratio. Scalar coherency spectrum and scalar difference spectrum “collapse” according to Sc ratios. Scalar spectral transfer at high Schmidt numbers has the same forward transfer process as that at low Schmidt numbers. The transfer becomes weaker at low to moderate wavenumbers as Sc increases, while the trend is reversed at high wavenumbers, suggesting that scalar spectral transfer at small scales is more important for scalars with high Sc . Subgrid-scale scalar transfer is dominated by forward transfer process and there are also significant portion of inverse transfer. Subgrid transfer becomes weaker with increasing cutoff wavenumber and stronger with increasing Sc .

6.2 Future research

In this concluding section, possible extensions of the current work and further investigations of scalars at high Schmidt numbers in other types of turbulent flows are discussed. These possibilities can be summarized as follows: (a) Schmidt number effects in turbulent shear flow, (b) scalar mixing in rotating turbulence, (c) scalar conditional statistics related to

mixing models, (d) Lagrangian statistics of passive scalars.

Discussions have been given on issues of local isotropy and intermittency in isotropic turbulence in Chap.III and IV. Compared to isotropic turbulence, shear flow adds a source of anisotropy to turbulence velocity field. Whether this velocity anisotropy affects the local isotropy of scalar field and to what extent can be of interests. Whether Schmidt number plays a significant role in local isotropy compared to turbulent shears will also assist in a better understanding.

An important application of scalar mixing in rotating turbulence is in jet engines, where the velocity field is subjected to a uniform solid-body rotation. Strong local anisotropy has been found (Yeung and J.Xu 2004) due to Coriolis forces, and where the one-dimensional scalar spectrum in the direction of rotation is very different from that in the other two directions. The question remains whether Batchelor's k^{-1} scaling still holds for 1-D scalar spectrum in any direction and whether increasing Schmidt number will promote a return to isotropy of the statistics of scalar gradient fluctuations.

Research on the geometric structure of passive scalars has been conducted by several authors (Schumacher *etal.* 2003, Brethouwer *etal.* 2003). The alignment between the most compressive strain rate and the largest scalar gradient is believed to cause the formation of sheet-like scalar fronts. The effects of velocity field on the passive scalars can be partly quantified via scalar statistics conditional on the energy dissipation (Vedula *etal.* 2001). Scalar conditional statistics are essential in scalar mixing models. DNS has been proved to be an effective way to study such detailed statistics. Study of the scalar conditional statistics and the alignment between strain rate and scalar gradient will provide additional understanding on the scalar mixing at high Schmidt numbers.

Finally, a Lagrangian approach to study scalar mixing at high Schmidt numbers will provide a different perspective. Lagrangian statistics of the trajectories of fluid and scalar particles are essential in stochastic modeling of turbulent dispersion problems and DNS is a very useful and convenient tool in studying Lagrangian statistics. Our DNS data for the trajectories of scalar particles at high Schmidt numbers can be analyzed to obtain

various one-scalar statistics and two-scalar dispersion statistics that are needed in stochastic modeling.

Appendix A

Schmidt number effects on turbulent transport with uniform mean scalar gradient (P.K. Yeung, Shuyi Xu and K.R. Sreenivasan. *Phys. Fluids* **14** (2002), (4178-4191).

Abstract

We study by DNS the effects of Schmidt number (Sc) on passive scalars mixed by forced isotropic turbulence. The scalar field is maintained statistically stationary by a uniform mean gradient. We consider the scaling of spectra, structure functions, local isotropy and intermittency. For moderately diffusive scalars with $Sc = 1/8$ and 1, the Taylor-scale Reynolds number analyzed is either 140 or 240. A modest inertial-convective range is obtained in the spectrum, with a one-dimensional Obukhov-Corrsin constant of about 0.4, consistent with experimental data. However, the presence of a spectral bump makes a firm assessment somewhat difficult. The viscous-diffusive range is universal when scaled by Obukhov-Corrsin variables. In a second set of simulations we keep the Taylor-scale Reynolds number fixed at 38 but vary Sc from 1 to 64, roughly by factors of 2. We observe a gradual evolution of a -1 roll-off in the viscous-convective region as Sc increases, consistent with Batchelor's predictions. In the viscous-diffusive range the spectra follow Kraichnan's form well, with a coefficient that depends weakly on Sc . The breakdown of local isotropy manifests itself through differences between structure functions with separation distances in directions parallel and perpendicular to the mean scalar gradient, as well as through finite values of odd-order moments of scalar gradient fluctuations and of mixed velocity-scalar gradient fluctuations. However, all these indicators show, to varying degrees, an increasing tendency to isotropy with increasing Sc . The moments of scalar gradients and the scalar dissipation rate peak at $Sc \approx 4$. The intermittency exponent for the scale-range between the Kolmogorov and Batchelor scales is found to decrease with Sc , suggesting qualitative consistency with previous dye experiments in water ($Sc = O(1000)$).

Appendix B

Simulations of three-dimensional turbulent mixing for Schmidt numbers of the order 1000 (P.K. Yeung, S. Xu, D.A. Donzis and K.R. Sreenivasan. *Flow, Turbulence and Combustion* **72** (2004), (333-347).

Abstract

We report basic results from new numerical simulations of passive scalar mixing at Schmidt numbers (Sc) of the order of 1000 in isotropic turbulence. The required high grid-resolution is made possible by simulating turbulence at very low Reynolds numbers, which nevertheless possesses universality in dissipative scales of motion. The results obtained are qualitatively consistent with those based on another study (Yeung et al. 2002) with a less extended Schmidt number range and a higher Reynolds number. In the stationary state maintained by a uniform mean scalar gradient, the scalar variance increases slightly with Sc but scalar dissipation is nearly constant. As the Schmidt number increases, there is an increasing trend towards k^{-1} scaling predicted by Batchelor (1959) for the viscous-convective range of the scalar spectrum; the scalar gradient skewness approaches zero; and the intermittency measured by the scalar gradient flatness approaches its asymptotic state. However, the value of Sc needed for the asymptotic behavior to emerge appears to increase with decreasing Reynolds number of turbulence. In the viscous-diffusive range, the scalar spectrum is in better agreement with Kraichnan's (1968) result than with Batchelor's.

Appendix C

Scaling of multi-particle Lagrangian statistics in direct numerical simulations. (Yeung, P.K., Xu, S., Borgas, M.S. and Sawford, B.L. (2004), proceedings in *IUTAM Symposium on Reynolds Number Scaling in Turbulent Flow*, edited by A.J. Smits, Kluwer Academic Publishers, Dordrecht; 163-168. (Proceedings of the IUTAM Symposium Princeton, NJ, September 2002).

Abstract

Basic results on the evolution of shape and size of three- and four-particle Lagrangian clusters are reported from direct numerical simulations at Taylor-scale Reynolds numbers between 90 and 400 in isotropic turbulence. At early times shape distortion by viscous effects is such that both the area and volume increase less rapidly than the two-particle separation. Later-time behavior is characterized by power-law increases and a self-similar shape distribution. Reynolds number effects are more prominent in measures of size than in shape parameters.

Appendix D

Molecular dispersion in isotropic turbulence (Shuyi Xu, P.K. Yeung and M. Borgas) *APS Fluid Dynamics Division Meeting, Washington D.C., November 19-21 2000.*

Abstract

Effects of molecular diffusion are implicitly neglected when Lagrangian statistical models for fluid particle motion are used to describe contaminant dispersion in turbulence. However, they are important at small times or close to localized contaminant sources. Here we use direct numerical simulations (DNS) to study this process, by tracking the paths of molecules undergoing Brownian motion relative to the fluid, at a rate according to diffusivities giving Schmidt numbers from 0.01 to 1000. The statistics of molecules of a single “species” (at a given Schmidt number) are well described in the framework of Saffman (1960, *J. Fluid Mech.* **8**, 273), with the major modeling parameter being an integral time scale for the fluid velocity autocorrelation sampled along the molecular trajectory. We present two-species statistics measuring how molecules of species with different Schmidt number become dispersed from each other, with the separation distance being more intermittent if the Schmidt numbers involved are high. The two-species substance cross-correlation corresponding to the single-species autocorrelation is found to be very small. The DNS results are compared with a new Lagrangian stochastic model for relative dispersion including molecular Brownian motion. Implications for high Reynolds numbers are discussed.

REFERENCES

- Anselmet, F., Gagne, Y. & Hopfinger, E.J., "High-order velocity structure functions in turbulent shear flows," *J. Fluid Mech.* **140**, 63 (1984).
- Antonia, R.A. & Chambers, A.J., "On the correlation between turbulent velocity and temperature derivatives in the atmospheric surface layer," *Boundary-Layer Meteorol.* **18**, 399 (1980).
- Antonia, R.A. & Orlandi, P., "Effect of Schmidt number on small-scale passive scalar turbulence," *Appl. Mech. Rev.* **56**, 615 (2003).
- Antonia, R.A., Phan-Thien, N. & Satyaprakash, B.R., "Autocorrelation and spectrum of dissipation fluctuations in a turbulent jet," *Phys. Fluids* **24**, 554 (1981).
- Antonia, R.A. & Van Atta, C.W., "Structure functions of temperature fluctuations in turbulent shear flows," *J. Fluid Mech.* **84**, 561 (1978).
- Batchelor, G.K., "Small-scale variation of convected quantities like temperature in turbulent fluid," *J. Fluid Mech.* **5**, 113 (1959).
- Bilger, R.W. & Dibble, R.W., "Differential molecular diffusion effects in turbulent mixing," *Combust. Sci. Tech.* **28**, 161 (1982).
- Bogucki, D., Domaradzki, J.A. & Yeung, P.K., "Direct numerical simulations of passive scalars with $Pr > 1$ advected by turbulent flow," *J. Fluid Mech.* **343**, 111 (1997).
- Borgas, M.S., "A comparison of intermittency models in turbulence," *Phys. Fluids* **4**, 2055 (1992).
- Borgas, M.S., Sawford, B.L., Xu, S., Donzis, D.A. & Yeung, P.K., "High Schmidt number scalars in turbulence: Structure functions and Lagrangian theory," *Phys. Fluids* **16**, 3888 (2004).
- Brethouwer, G., Hunt, J.C.R. & Nieuwstadt, F.T.M., "Micro structure and Lagrangian statistics of the scalar field with a mean gradient in isotropic turbulence," *J. Fluid Mech.* **193**, 474 (2003).
- Chakravarthy, V.K. & Menon, S., "Linear eddy simulations of Reynolds number and Schmidt number effects on turbulent scalar mixing," *Phys. Fluids* **13**, 488 (2001).
- Chen, J.Y., Bilger, R.W. & Dibble, R.W., "PDF modeling of turbulent non-premixed $CO/H_2/N_2$ jet flames with reduced mechanisms," *23rd Symposium (International) on Combustion* (The combustion Institute, Pittsburgh), 775 (1990).
- Chen, S., Doolen, G., Herring, J.R., Kraichnan, R.H., Orszag, S.A. & She, Z.S., "Far-dissipation range of turbulence," *Phys. Rev. Lett.* **70**, 3051 (1993).

- Chen, S., Sreenivasan, K.R. & Nelkin, M., “Inertial range scalings of dissipation and Enstrophy in isotropic turbulence,” *Phys. Rev. Lett.* **79**, 1253 (1997).
- Chertkov, M., Falkovich, G. & Kolokolov, I., “Intermittent dissipation of a passive scalar in turbulence,” *Phys. Rev. Lett.* **80**, 2121 (1998).
- Cleve, J., Greiner, M. & Sreenivasan, K.R., “On the effects of surrogacy of energy dissipation in determining the intermittency exponent in fully developed turbulence,” *Europhys. Lett.* **61**, 756 (2003).
- Corrsin, S., “On the spectrum of isotropic temperature fluctuations in isotropic turbulence,” *J. Appl. Phys.* **22**, 469 (1951).
- Dasi, L.P., “The small-scale structure of passive scalar mixing in turbulent boundary layers,” *Ph.D thesis, School of Civil Engineering, Georgia Institute of Technology*, August (2004).
- Dillon, T.M. & Caldwell, D.R., “The Batchelor spectrum and dissipation in the upper ocean,” *J. Geophys. Res.* **85**, 1910 (1980).
- Domaradzki, J.A., Liu, J.A. & Brachet, M.E., “Analysis of subgrid-scale interactions in numerically simulated isotropic turbulence,” *Phys. Fluids A* **5**, 1747 (1993).
- Domaradzki, J.A., Metcalfe, R.W., Rogallo, R.S. & Riley, J.J., “Analysis of subgrid-scale eddy viscosity with use of results from direct numerical simulations,” *Phys. Rev. Lett.* **58**, 547 (1987).
- Domaradzki, J.A. & Rogallo, R.S., “Local energy transfer and nonlocal interactions in homogeneous, isotropic turbulence,” *Phys. Fluids A* **2**, 413, (1990).
- Drake, M.C., Pitz, R.W. & Lapp, M., “Laser measurements on non-premixed H_2 -air flames for assessments of turbulent combustion models,” *AIAA J.* **24**, 905 (1986).
- Eswaran, V. & Pope, S.B., “Direct numerical simulations of the turbulent mixing of a passive scalar,” *Phys. Fluids* **31**, 506 (1988).
- Falkovich, G., “Bottleneck phenomenon in developed turbulence,” *Phys. Fluids* **6**, 1411 (1994).
- Fox, R.O., “The Lagrangian spectral relaxation model for differential diffusion in homogeneous turbulence,” *Phys. Fluids* **11**, 1150 (1999).
- Frisch, U., Sulem, P.L. & Nelkin, M., “A simple dynamical model of intermittent fully developed turbulence,” *J Fluid Mech.* **87**, 719 (1978).
- Frisch, U., *Turbulence*, Cambridge University Press, Cambridge, U.K. (1995).
- Gibson, C.H. & Schwarz, W.H., “The universal equilibrium spectra of turbulent velocity and scalar fields,” *J. Fluid Mech.* **16**, 365 (1963).
- Gibson, C.H., Friehe, C.A. & McConnell, S.O., “Skewness of temperature derivatives in turbulent shear flows,” *Phys. Fluids Suppl.* **20**, 156 (1977).

- Gotoh, T., Nagaki, J. & Kaneda, Y., “Passive-scalar spectrum in viscous-convective range in two-dimensional turbulence,” *Phys. Fluids* **12**, 155 (2000).
- Holzer, M. & Siggia, E.D., “Turbulent mixing of a passive scalar,” *Phys. Fluids* **6**, 1820 (1994).
- Kármán, T. von & Howarth, L., “On the statistical theory of isotropic turbulence,” *Proc. R. Soc. Lond. A* **164**, 192 (1938).
- Kerr, R.M., “Higher-order derivative correlations and the alignment of small-scale structures in isotropic numerical turbulence,” *J. Fluid Mech.* **153**, 31 (1985).
- Kolmogorov, A.N., “The local structure of turbulence in an incompressible viscous fluid for very large Reynolds numbers,” *Dokl. Akad. Nauk. SSSR* **30**, 301 (1941).
- Kolmogorov, A.N., “A refinement of previous hypotheses concerning the local structure turbulence in a viscous incompressible fluid at high Reynolds number,” *J. Fluid Mech.* **13**, 82 (1962).
- Kraichnan, R.H., “Small-scale structure of a scalar field convected by turbulence,” *The Phys. Fluids* **11**, 945 (1968).
- Kraichnan, R.H., “Intermittency in the very small scales of turbulence,” *Phys. Fluids* **10**, 2081 (1967).
- Kraichnan, R.H., “Eddy viscosity in two and three dimensions,” *J. Atmos. Sci.* **33**, 1521 (1976).
- Kraichnan, R.H., “Anomalous scaling of a randomly advected passive scalar,” *Phys. Rev. Lett.* **72**, 1016 (1994).
- Lesieur, M. & Rogallo, R.S., “Large-eddy simulation of passive scalar diffusion in isotropic turbulence,” *Phys. Fluids A* **1**, 718 (1989).
- Lumley, J.L. & Yaglom, A.M., “A century of turbulence,” *Flow, Turb. and Combust.* **66**, 241 (2001).
- Meneveau, C. & Sreenivasan, K.R., “Simple multifractal cascade model for fully-developed turbulence,” *Phys. Rev. Lett.* **59**, 1424 (1987).
- Meneveau, C. & Sreenivasan, K.R., “The multifractal nature of turbulent energy dissipation,” *J. Fluid Mech.* **224**, 429 (1991).
- Miller, P.L. & Dimotakis, P.E., “Measurements of scalar power spectra in high Schmidt number turbulent jets,” *J. Fluid Mech.* **308**, 129 (1996).
- Monin, A.S. & Yaglom, A.M., *Statistical Fluid Mechanics* Vol. II, MIT Press, Cambridge, MA (1975).
- Moin, P., Squires, K., Cabot, W. & Lee, S., “A dynamic subgrid-scale model for compressible turbulence and scalar transport,” *Phys. Fluids A* **3**, 2746 (1991).
- Mydlarski, L. & Warhaft, Z., “Passive scalar statistics in high-Péclet-number grid turbulence,” *J. Fluid Mech.* **358**, 135 (1998).

- Nelkin, M., "Do the dissipation fluctuations in high Reynolds number turbulence define a universal exponent?" *Phys. Fluids* **24**, 556 (1981).
- Nelkin, M., "Enstrophy and dissipation must have the same scaling exponent in the high Reynolds number limit of fluid turbulence," *Phys. Fluids* **11**, 2202 (1999).
- Nilsen, V. & Kosály, G., "Differentially diffusing scalars in turbulence," *Phys. Fluids* (1998).
- Nye, J.O. & Brodkey, R.S., "The scalar spectrum in the viscous-convective subrange," *J. Fluid Mech.* **29**, 151 (1967).
- Obukhov, A.M., "The structure of the temperature field in a turbulent flow," *Izv. Akad. Nauk. SSSR, Ser. Geophys.* **13**, 58 (1949).
- Obukhov, A.M., "Some specific features of atmospheric turbulence," *J. Fluid Mech.* **13**, 77 (1962).
- Orlandi, P. & Antonia, R.A., "Dependence of the non-stationary form of Yaglom's equation on the Schmidt number," *J. Fluid Mech.* **451**, 99 (2002)
- Overholt, M.R. & Pope, S.B., "Direct numerical simulation of a passive scalar with imposed mean scalar gradient in isotropic turbulence," *Phys. Fluids* **8**, 3128 (1996).
- Overholt, M.R. & Pope, S.B., "A deterministic forcing scheme for direct numerical simulations of turbulence," *Computers & Fluids* **27**, 11 (1998).
- Pope, S.B., "Computations of turbulent combustions: progress and challenges," *Twenty-Third Symposium (International) on Combustion*, The combustion Institute (invited plenary lecture), 591, (1990).
- Pope, S.B., *Turbulent Flows*. Cambridge University Press, Cambridge, U.K. (2000).
- Prasad, R.R. & Sreenivasan, K.R., "Quantitative three-dimensional imaging and the structure of passive scalar fields in fully turbulent flows," *J. Fluid Mech.* **216**, 1 (1990).
- Praskovsky, A. & Oncley, S., "Comprehensive measurements of the intermittency exponent in high Reynolds number turbulent flows," *Fluid Dyn. Res.* **21**, 331 (1997).
- Pullin, D.I., "A vortex-based model for the subgrid flux of a passive scalar," *Phys. Fluids* **12**, 2311 (2000).
- Qian, J., "Viscous range of turbulent scalar of large Prandtl number," *Fluid Dyn. Res.* **15**, 103 (1995).
- Rogallo, R.S., "Numerical experiments in homogeneous turbulence," *NASA Tech. Memo.* 81315 (1981).
- Rothschild, B.J. & Osborn, T.R., "Small-scale turbulence and plankton contact rates," *J. Plankton Res.* **10**(3), 465 (1988).
- Saylor, J.R. & Sreenivasan, K.R., "Differential diffusion in low Reynolds number water jets," *Phys. Fluids* **10**, 1135 (1998).

- Schumacher, J., "Derivative moments in stationary homogeneous shear turbulence," *J. Fluid Mech.* **441**, 109 (2001).
- Schumacher, J., "Schmidt number dependence of derivative moments for quasi-static straining motion," *J. Fluid Mech.* **479**, 221 (2003).
- Schumacher, J., "Geometric features of the mixing of passive scalars at high Schmidt numbers," *Phys. Rev. Lett* **91**, 174501 (2003).
- She, Z.S. & Orszag, S.A., "Physical model of intermittency in turbulence: inertial-range non-Gaussian statistics," *Phys. Rev. Lett* **66**, 1701 (1991),
- Shen, X. & Warhaft, Z., "The anisotropy of the small scale structure in high Reynolds number ($R_\lambda \sim 1000$) turbulent shear flow," *Phys. Fluids* **12**, 2976 (2000).
- Sirivat, A. & Warhaft, Z., "The mixing of passive helium and temperature fluctuations in grid turbulence," *J. Fluid Mech.* **120**, 475 (1982).
- Smith, L.L., Dibble, R.W., Talbot, L., Barlow, R.S. & Carter, C.D., "Laser Raman scattering measurements of differential molecular diffusion in nonreacting turbulent jets of H_2/CO_2 mixing with air," *Phys. Fluids* **7**, 1455 (1995).
- Sreenivasan, K.R. & Antonia, R.A., "Skewness of temperature derivatives in turbulent shear flows," *Phys. Fluids* **20**, 1986 (1977).
- Sreenivasan, K.R. & Antonia, R.A., "The phenomenology of small-scale turbulence," *Annu. Rev. Fluid Mech.* **29**, 435 (1997).
- Sreenivasan, K.R., "On local isotropy of passive scalars in turbulent shear flows," *Proc. Roy. Soc. Lond.* **434**, 165 (1991).
- Sreenivasan, K.R., "The passive scalar spectrum and the Obukhov-Corrsin constant," *Phys. Fluids* **8**, 189 (1996).
- Sreenivasan, K.R., "an update on the energy dissipation rate in isotropic turbulence," *Phys. Fluids* **10**, 528 (1998).
- Sreenivasan, K.R. & Kailasnath, P., "An update on the intermittency exponent in turbulence," *Phys. Fluids A* **5**, 512 (1993).
- Sreenivasan, K.R. & Prasad, R.R., "New results on the fractal and multifractal structure of the large Schmidt number passive scalars in fully developed turbulence," *Physica D* **38**, 322 (1989).
- Sreenivasan, K.R., "Possible effects of small-scale intermittency in turbulent reacting flows," *Flow, Turbulence and Combustion* **72**, 115 (2004).
- Swaminathan, N. & Bilger, R.W., "Direct numerical simulation of turbulent nonpremixed hydrocarbon reaction zones using a two-step reduced mechanism," *Comb. Sci. & Tech.* **127**, 167 (1997).
- Tong, C. & Warhaft, Z., "On passive scalar derivative statistics in grid turbulence," *Phys. Fluids* **6**, 2165 (1994).

- Tong, C. & Warhaft, Z., "Passive scalar dispersion and mixing in a turbulent jet," *J. Fluid Mech.* **292**, 1 (1995).
- Turns, S.R., *An Introduction to Combustion, Concepts and Applications*. McGraw-Hill, Boston, MA (2000).
- Van Atta, C.W. & Chen, W.Y., "Structure functions of turbulence in the atmospheric boundary layer over the ocean," *J. Fluid Mech.* **44**, 145 (1970).
- Van Atta, C.W. & Yeh, T.T., "Evidence for scale similarity of intermittency in turbulent flows at large Reynolds numbers," *J. Fluid Mech.* **71**, 417 (1975).
- Vedula, P., Yeung, P.K. & Fox, R.O., "Dynamics of scalar dissipation in isotropic turbulence: a numerical and modeling study," *J. Fluid Mech.* **433**, 29 (2001).
- Wang, L.P., Chen, S. & Brasseur, J.G., "Examination of hypotheses in the Kolmogorov refined turbulence theory through high-resolution simulations, Part 1. velocity field," *J. Fluid Mech.* **309**, 113 (1996).
- Wang, L.P., Chen, S. & Brasseur, J.G., "Examination of hypotheses in the Kolmogorov refined turbulence theory through high-resolution simulations, Part 2. Passive scalar field," *J. Fluid Mech.* **400**, 163 (1999).
- Warhaft, Z. & Lumley, J.L., "An experimental study of the decay of temperature fluctuations in grid-generated turbulence," *J. Fluid Mech.* **88**, 659 (1978).
- Warhaft, Z., "Passive scalars in turbulent flows," *Annu. Rev. Fluid Mech.* **425**, 161 (2000).
- Williams, B.S., Marteau, D. & Gollub, J.P., "Mixing of a passive scalar in magnetically forced two-dimensional turbulence," *Phys. Fluids* **9**, 2061 (1997).
- Yaglom, A.M., "On the local structure of a temperature field in a turbulent flow," *Dokl. Akad. Nauk. SSSR* **69**, 743 (1949).
- Yeh, T.T. & Van Atta, C.W., "Spectral transfer of scalar and velocity fields in heated-grid turbulence," *J. Fluid Mech.* **58**, 233 (1973).
- Yeung, P.K., "Multi-scalar triadic interactions in differential diffusion with and without mean scalar gradients," *J. Fluid Mech.* **321**, 235 (1996).
- Yeung, P.K., "Correlations and conditional statistics in differential diffusion: scalars with uniform mean gradients," *Phys. Fluids* **10**, 2621 (1998).
- Yeung, P.K. & Moseley, C.A., "A message-passing, distributed memory parallel algorithm for direct numerical simulation of turbulence with particle tracking," *Parallel Computational Fluid Dynamics: Implementations and Results Using Parallel Computers* A. Ecer, J. Periaux, N. Satofuka and S. Taylor (Editors). Elsevier Science Publishers, Amsterdam, 473 (1995).
- Yeung, P.K., Sykes, M.C. & Vedula, P., "Direct numerical simulation of differential diffusion with Schmidt numbers up to 4.0," *Phys. Fluids* **12**, 1601 (2000).

- Yeung, P.K. & Sawford, B.L., "Random sweeping hypothesis for passive scalars in isotropic turbulence," *J. Fluid Mech.* **459**, 129 (2002).
- Yeung, P.K. & Pope, S.B., "Differential diffusion of passive scalars in isotropic turbulence," *Phys. Fluids A* **5**, 2467 (1993).
- Yeung, P.K. & Sawford, B.L., "Random-sweeping hypothesis for passive scalars in isotropic turbulence," *J. Fluid Mech.* **459**, 129 (2002).
- Yeung, P.K., Xu, S. & Sreenivasan, K.R., "Schmidt number effects on turbulent transport with uniform mean scalar gradient," *Phys. Fluids* **14**, 4178 (2002).
- Yeung, P.K., Xu, S., Donzis, D.A. & Sreenivasan, K.R., "Simulations of three-dimensional turbulent mixing for Schmidt numbers of the order 1000," *Flow, Turbulence and Combustion* **72**, 333 (2004).
- Yeung, P.K. & Xu, J., "Effects of rotation on turbulent mixing: nonpremixed passive scalars," *Phys. Fluids* **16**, 93 (2004).
- Yeung, P.K. & Zhou, Y., "Analysis of subgrid eddy diffusivity in turbulence using direct numerical simulation databases," *AIAA*, 96-3074 (1996).
- Yeung, P.K. & Zhou, Y., "Universality of the Kolmogorov constant in numerical simulations of turbulence," *Phys. Rev. E* **56**, 1746 (1997).
- Zhou, Y. & Vahala, G., "Reformulation of recursive renormalization group based subgrid modeling of turbulence," *Phys. Rev. E* **47**, 2503 (1993).

VITA

Shuyi Xu was born in a small town in the Northeast of China where her father, who was originally from southern China, settled down in his late twenties. Shuyi Xu was admitted to Beijing University of Aeronautics and Astronautics in 1992 and obtained her Bachelor of Engineering degree in Aerospace Engineering of Jet Propulsion in 1996. Since 1998, she has been pursuing graduate studies in School of Aerospace Engineering at the Georgia Institute of Technology.

Shuyi Xu has broad interests in mathematics, sciences, humanities, music and arts. Through years of study and research, she came to realize that she has a better intuition and “feel” in mathematical approach to things than physical one. She is still trying to find the “perfect” niche for a career where her strength, passion and sense of self-accomplishment meet.